# HARNESSING ELASTIC INSTABILITIES FOR ENERGY TRANSDUCTION

By

Suihan Liu

A DISSERTATION

Submitted to
Michigan State University
in partial fulfillment of the requirements
for the degree of

Engineering Mechanics - Doctor of Philosophy

2019

# ABSTRACT

HARNESSING ELASTIC INSTABILITIES FOR ENERGY TRANSDUCTION

By

Suihan Liu

The recent reconsideration of structural instabilities as a favorable mechanism instead of a route leading to failure, has brought increased attention across disciplines to extend their understanding of structural instabilities in both form and function. In biological systems energy transduction is a concept that describes the conveyance of energy – the process to collect and store energy and then release it to perform work. Given the ingenious examples from nature, developing "smart" structures that can emulate biological ones has long been an engineering goal. Realizing energy transduction in mechanical systems offers many opportunities in the design of smart structural systems that can respond and react to their environment. Due to the ability of internal energy exchange within a structure or solid, the presence of elastic instabilities allows to drive dynamic reactions by releasing the system energy in a designed manner. Therefore, elastic instabilities can be harnessed to achieve energy transduction in a mechanical system. The research reported in this dissertation was aimed to address two challenges in mechanical energy transduction: (1) harvest electric energy from low frequency quasi-static mechanical deformations, and (2) dissipate energy in materials subject to cyclic shear deformations in a recoverable and rate-independent manner.

Novel structural concepts are proposed to address the noted challenges. Physical prototypes of both concepts were built through 3D multi-material polymer printing and tested experimentally to verify the expected behavior. For each structural system, a theoretical model was developed based on energy methods, and numerical simulations were carried out by finite element analyses (FEA)

using the commercial program ABAQUS. The experimentally validated analytical and numerical models were used to predict system response and explore the design space for each concept.

In the energy harvesting concept, the strain energy accumulated in axially compressed bilaterally constrained columns under quasi-static deformations is released through multiple buckling instabilities in their elastic postbuckling response. The released strain energy is transformed into usable electric energy by coupling the dynamic response with the piezoelectric effect of mounted transducers. This proposed concept overcomes the poor performance of piezoelectric materials under low frequency excitations and it was shown to be effective in harvesting energy directly from quasi-static deformation sources. This work focused on enhancing this concept by maximizing the output through non-prismatic column designs for piezoelectric oscillators and integrated piezoelectric patches for geometric efficiency in energy harvesting devices. It was demonstrated that the resulting energy generation can adequately provide power supply for low-power budget devices with enhanced performance, which can be potentially used to power structural health monitoring systems and human wearable/implantable bio-sensors.

The energy-dissipative material concept, which proposes the use of elastic inclined beams in the microstructure of the material architecture, was shown to manage the strain energy generated due to cyclic shear deformations and dissipate it through sequential snapping instabilities. The periodic arrangement of the elastic inclined beams permits the generation of a ‘twinkling’ phenomenon under repeated in-plane deformations, which results in rate-independent energy dissipations and a fully recoverable response. This concept overcomes the disadvantages of permanent deformations and rate dependency in traditional energy dissipating mechanisms and materials. The developed material design concept can be deployed in diverse applications such as personal protection, packaging, and civil structures.

*致我的妈妈。*

# ACKNOWLEDGMENTS

I would like to dedicate my first and sincerest gratitude to my advisor Professor Rigoberto Burgueño for everything he did for me, even though it is not possible to express all my appreciation to him in a few lines here. In the confusion of nearing the conclusion of my undergraduate studies, I found myself drawn to Prof. Burgueño's strong character and love for structures. I could not make a better decision than choosing to work with him and pursuing a Ph.D. degree when he introduced me the fascinating field of nonlinear structural mechanics. Prof. Burgueño is always the first one comes to work, his office door is always open, he is always patient and caring, and I know he is always there to support me. The inspiring guidance and the faith that he constantly placed in me made this dissertation possible. His influence on me is fundamental and beyond academics. His devotion to work, curiosity to learn, earnestness towards people, idealism of mind, and perfectionism in life will continuously influence my attitude towards work and life. Prof. Burgueño is an excellent teacher and the best advisor that any student could ever ask for. But more than an advisor, Rigo is my best friend. I was very fortunate to be able to know him professionally and personally. I will never forget those days that we laughed together. As I complete my doctoral studies I hope that our friendship will continue.

I am also indebted to my dissertation committee members, Professor Alejandro Díaz, Professor Sara Roccabianca, and Professor Xiaobo Tan. I greatly appreciate Prof. Díaz's attitude toward science. He raised key questions and gave valuable input that forced me to think about my work in a variety of ways, and for that I am grateful. He also has a great sense of humor in his smart and unpredictable way, which was fun and made me a bit nervous at the same time when talking to him. I am very happy that Prof. Roccabianca joined MSU and that I was able to get to know her. I remember the chat we had in a snowy morning before her linear elasticity class, during which she shared with me her experience and gave me valuable advice on pursuing a career in academia. She is always very supportive and approachable, with a genial smile on her face. And her Italian fashion taste also brightens up the Engineering building. I am really thankful for Prof. Tan's presence in my committee. I admire the excellence in his academic career, which motivates me to pursue higher goals and do better on my own work. I truly appreciate all their time, advice, insight, and guidance, which contributed greatly to my personal and professional development.

I also want to acknowledge the great faculty and staff members in the College of Engineering who generously helped me during my undergraduate and graduate studies at MSU. My appreciation goes to Prof. Ronald Averill for his help and guidance on numerical modeling and optimization; Prof. M. Emin Kutay and Prof. Patrick Kwon for their excellent lectures and support when I was applying for graduate schools; Dr. Katy Colbry for her time and advice in helping me apply for the NSF graduate fellowship; and Mr. Brian Wright for his help in the preparations of 3D printed prototypes.

My sincere gratitude also goes to all the colleagues with whom I worked the closest. Specifically, I want to thank Mingzhe Li for helping me many times on setting up experiments in the lab; and Ali Imani Azad for the collaboration and discussions, and his help with the numerical simulations and material testing presented in Section 3.6. I also had a great time sharing an office with Nan Hu, Pegah Rajaei, Shabnam Rajaei, Ali Imani Azad, and Charifa Hejase, who helped make every working day entertaining.

I am very grateful of all the good friends I made at MSU who helped me through these past four years. Xinyi Wang, Zhao Li, Pengfei Yuan, and Ruiqiong Guo, for the weekends, holidays, trips, laughs, good wine and food that we shared together. My appreciation also goes to Ruike

Zhao, for her friendship and encouragement. A special thanks to Nan Hu who is like a big brother to me, and his loving family who brought me warmth and joy. I also want to acknowledge the East Lansing Hot Yoga Studio, its lovely instructors, staff, and relaxing environment helped me to keep physical health and mental peacefulness during graduate school.

In addition, my doctoral study could not have been completed without the primary funding support from the U.S. National Science Foundation, and the recruitment fellowship from the College of Engineering at MSU. I also appreciate the travel funding opportunities provided by the Graduate School, the College of Engineering, the Department of Civil and Environmental Engineering, and the Department of Mechanical Engineering to allow me to attend multiple conferences during my graduate studies.

I also want to express my affection to my dog Saki, who always keeps me company and for showing me a worriless attitude towards life.

Lastly and most importantly, there is nothing that I have ever accomplished without the endless love and unconditional support from my mom, Donghong Sun, who is my role model and also my biggest fan. She always owns my deepest gratitude.

# TABLE OF CONTENTS

# LIST OF TABLES

# LIST OF FIGURES

# Chapter 1

# INTRODUCTION

## 1.1 Motivation

Recently, the reconsideration of structural instabilities as a favorable mechanism to provide functionality instead of representing a failure limit state, have brought together the disciplines of physics, mechanics, mathematics, biology, and materials science to extend their understanding of elastic instabilities for both form and function. Ingenious examples on the use of structural instabilities can be found in nature, as shown in Figure 1-1. One of the fastest motions in the plant kingdom, the rapid closure of the Venus flytrap lobes to capture insects, results from a snap-through instability [1]; buckling instabilities in flagella allows bacteria to change swimming direction within a faction of a second [2], and is also the smallest example of using the mechanism of instabilities. In addition, buckling instabilities also explain the wave-like shape of a snake crawling between walls [3], and the cause behind the helical shape of plant roots as they penetrate into soils [4, 5].

Developing “smart” structures that can emulate biological systems in their integrated ability to sense and adapt has long been an engineering goal. In biological systems, energy transduction is a concept that describes the conveyance of energy, such as the processes of photosynthesis and respiration, which collect photonic energy and convert into chemical energy that is released by plants to grow. Realizing was for energy transduction in mechanical systems offers ample opportunities in the design of smart structural systems that can respond and react to the environment. Due to the ability of internal exchange of energy within a structure or solid, the presence of elastic instabilities allows to drive dynamic reactions by releasing the system energy in a designed manner. Therefore, structural instabilities can be harnessed to achieve energy transduction in mechanical system.

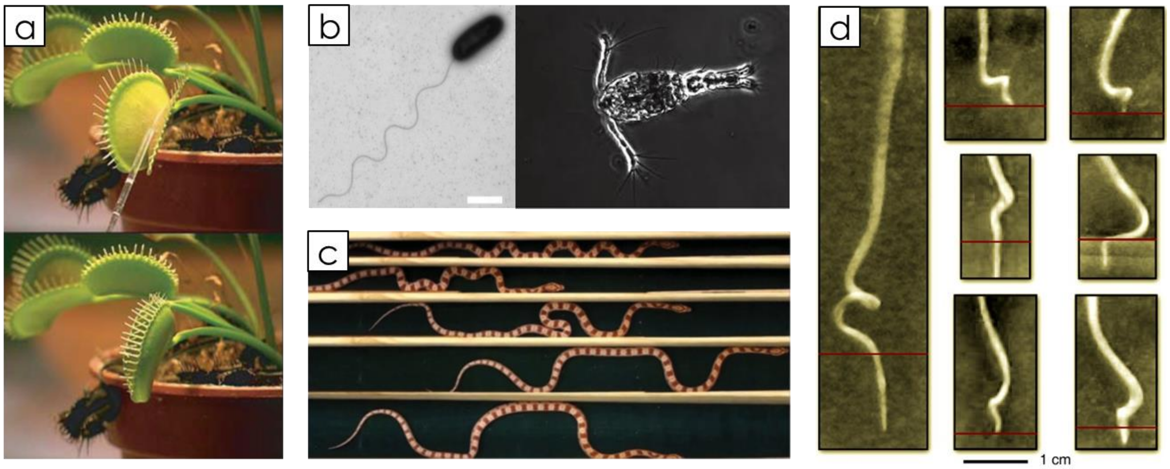

Figure 1-1: Examples of structural instabilities in nature for both form and function: (a) the snap closure of the Venus flytrap lobes [1], (b) the flagellar buckling of swimming bacteria [2], (c) the wave-like shape of a crawling snake [3], and (d) the helical buckling shape of plant roots [5].

Before turning deeply into a presentation of the controls and uses of structural instability, it is necessary to briefly introduce structural instability in terms of its historical development, definitions, relevant phenomena and structural forms, and current developments and applications.

## 1.2 History and relevance of structural instability

The study of structural instability cannot be separated from stability theory in mechanics, which has a long history that can be traced back to the seventeenth century. A brief timeline of the historical developments of structural (in)stability is shown in Figure 1-2. The first idea of stability was brought by Torricelli in 1644, in which he considered a system of two interconnected weights that would not be moving if they take the lowest possible position under gravity [6]. Without specifically using the term ‘*stability*,’ Torricelli’s axiom undeniably paved the foundation of defining stability based on the potential energy concept. The theory of elastic stability began with the work of Euler on the buckling of compressed columns in 1744, which is also the first time the term '*stability'* was introduced [7]. Based on a formulation of the differential equation of the elastica, he concluded that a slender column would bend (i.e., buckle) instead of shortened under compression. In 1788, Lagrange formalized the Torricelli's axiom and posed that the system is stable if its potential energy has a strict minimum (i.e., if it is positive definite), assuming the total energy is continuous and the system contains only conservative and dissipative forces [8]. Lagrange's theorem was later on rigorously proven by Dirichlet, showing that a minimum of the potential energy is sufficient to prove stability [9]. Thus, the energy criterion of stability, known as the Lagrange-Dirichlet theorem, gives the definition of stability for conservative systems. Even though instability is a dynamic concept, the Lagrange-Dirichlet theorem allows determining the limits of stability statically (i.e., reduces the stability problem to an investigation of the shape of the potential energy surface as a function of the generalized displacements of the structure). In 1885, Poincaré first introduced a general bifurcation theory and classified various types of stationary points [10]. The exact mathematical definition of stability was given by Lyapunov in 1945, which stated that an equilibrium state is stable if, and only if, all motions of the system starting close to the equilibrium state remain close to this state for all time [11]. This definition of stability is general and applies to all systems in mechanics, as well as other scientific fields beyond the context of mechanics. Lyapunov proved his theorem through two distinct methods, the indirect method through linearization and the direct method based on energy, which essentially employed the Lagrange–Dirichlet stability theorem. Comparing these two theorems, the Lagrange–Dirichlet theorem is a special case of the Liapunov theorem, which only permits dissipative forces in conservative systems that do not destroy the existence of the potential energy function (i.e., not applicable for dissipative forces due to material damage). After the definition of stability was rigorously defined, the emergence of the theory of structural stability began; which has resulted in numerous analytical theories and numerical tools to provide safe design guidelines. Most linear elastic problems of structural stability were solved by the end of the 19th century, and nonlinear elasticity problems were extensively explored in the early 20th century. However, the focus of these studies were on the onset of critical limits of stability. The post-critical behavior in elastic structures started attracting more attention only a few decades ago. A fundamental and detailed discussion on elastic stability and instability can be found in the books by Thompson and Hunt [12, 13] and by Bažant and Cedolin [14].

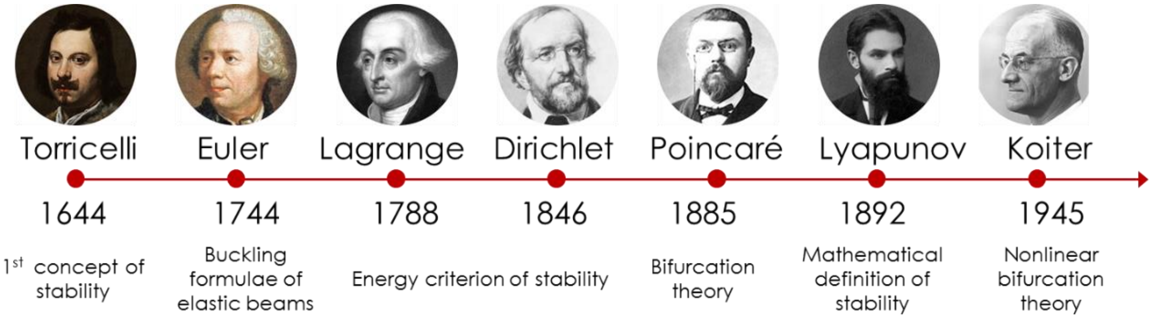

Figure 1-2: Timeline of the historical developments of structural (in)stability.

## 1.3 Energy criterion of stability

The structural systems that are considered in this dissertation are conservative; thus, the stability definition by the Lagrange-Dirichlet theorem applies. The potential energy of a system consists the (elastic) strain energy due to stretching and bending, and the external work; which can be written as:

$$U = U_s + U_b - W. \qquad \text{Equation 1-1}$$

The energy concept of stability is often illustrated by considering a simple "ball on the hill" analogy, as shown in Figure 1-3. The potential energy of the ball with mass *m* due to gravity depends on its position on a smooth hill with height $h$, which can be written as:

$$U(x) = mgh(x). \qquad \text{Equation 1-2}$$

Since the force of a system is the first variation of the potential energy with respect to displacement, and recalling Newton's second law that equilibrium it yields:

$$\frac{\partial U}{\partial x} = F = mg\frac{\partial h}{\partial x} = 0. \qquad \text{Equation 1-3}$$

The equilibrium states can be either stable or unstable. According to the Lagrange-Dirichlet theorem, the system is at a stable equilibrium state when the second variation of the potential energy is greater than zero, as

$$\frac{\partial^2 U}{\partial x^2} = \frac{\partial F}{\partial x} = mg\frac{\partial^2 h}{\partial x^2} > 0, \qquad \text{Equation 1-4}$$

where the ball is resting at the local energy minimum. This indicates that any small perturbation $\delta x$ will return the ball to its original position, increase the potential energy, and increase the reaction force. The system is at an unstable equilibrium state when the second variation of energy is less than zero, as

$$\frac{\partial^2 U}{\partial x^2} = \frac{\partial F}{\partial x} = mg\frac{\partial^2 h}{\partial x^2} \leq 0, \qquad \text{Equation 1-5}$$

where the ball is resting at the local energy maximum. This indicates that any small perturbation $\delta x$ will roll the ball away from its original position, decrease the potential energy, and decrease the reaction force. The critical limit between the stable and unstable states is at $\frac{\partial F}{\partial x} = 0$.

From the above illustration, we can therefore conclude that instability can be identified in elastic systems by a non-convex potential energy surface and a negative stiffness region (i.e., the right half of Figure 1-3). The non-convex potential energy allows the displacement to increase as energy decreases, which leads an *energy release* from the system. The stiffness of most elastic systems is positive and the reaction force exerted onto the system is in the opposite direction to that of the system's governing deformation, which corresponds to a restoring force. A system with a negative stiffness region exerts a reaction force in the same direction as the deformation, which helps the deformation increase further and indicates a *dynamic motion*. In structures under conservative loads, instability is elicited by either buckling or snapping phenomena, which are discussed in the following sections.

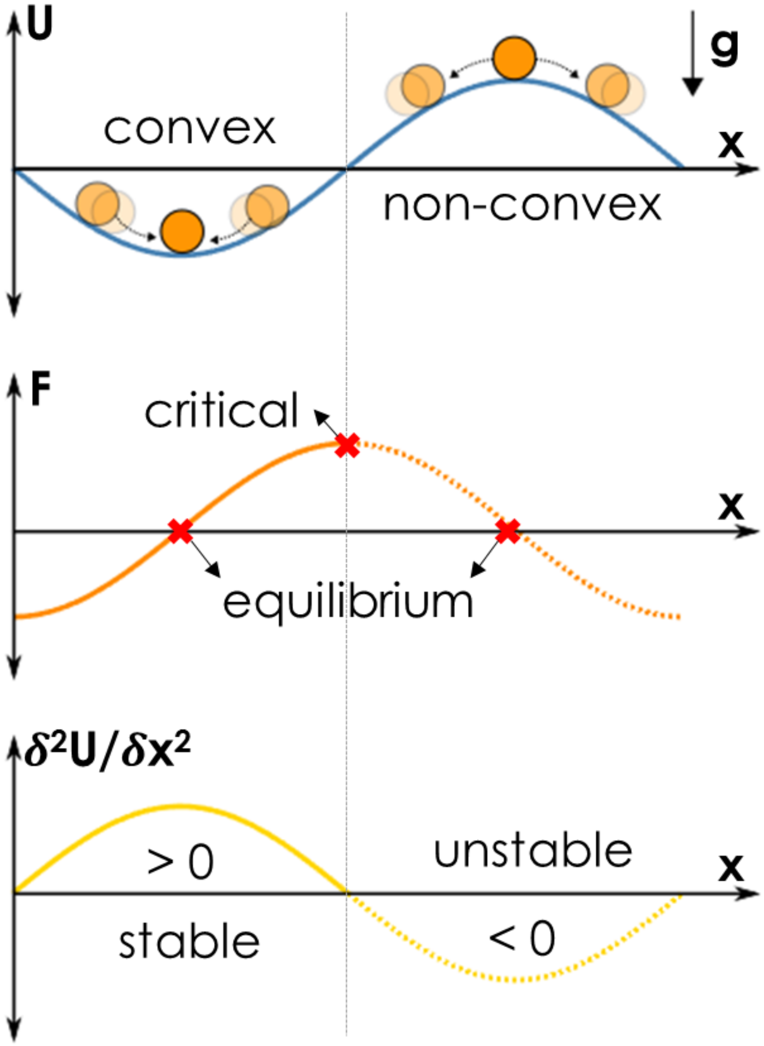

Figure 1-3: Illustration of stability and instability in terms of potential energy of an elastic structural system.

## 1.4 Basic structural instability phenomena

### 1.4.1 Buckling

Buckling occurs in slender structures that fail in carrying compressive load by membrane stresses, shown as the development of out-of-plane deformations due to bending. The simplest example to be considered for buckling is a pin-ended column under compressive load, as shown in Figure 1-4. Slender structures are most efficient at carrying loads under a membrane stress state. Thus, the column will initially try to deform by pure compression before buckling, and the potential energy of the column due to compressive load $P$ can be written as:

$$U = U_s - W = \int_0^l \frac{EA}{2}\varepsilon^2 dx - P\Delta L \qquad \text{Equation 1-6}$$

After buckling, the curvature in the column causes bending energy to develop in the system. The potential energy thus becomes

$$U = U_s + U_b - W = \int_0^l \frac{EI}{2}\kappa^2 dx + \int_0^l \frac{EA}{2}\varepsilon^2 dx - P\Delta L \qquad \text{Equation 1-7}$$

where

$$\Delta L = \int_0^l \left(\sqrt{dx^2 + dy^2} - dx\right) dx = \int_0^l \left(\sqrt{1 + (y')^2} - 1\right) dx \cong \frac{1}{2}\int_0^l (y')^2\, dx \qquad \text{Equation 1-8}$$

$$\kappa = y" \; and \; \varepsilon = \frac{1}{2}(y')^2 \qquad \text{Equation 1-9}$$

It can be seen that the stretching energy appears in the column before and after buckling. Therefore, the incremental compressive load $P$ at the onset of critical buckling only causes an increase of the strain energy due to bending, and the potential energy at the critical buckling can be written as:

$$\frac{\partial U}{\partial x} = U_b - W = \int_0^l \left[\frac{EI}{2}\left(y"\right)^2 - \frac{P}{2}(y')^2\right] dx \qquad \text{Equation 1-10}$$

Equation 1-10 yields the equilibrium state at $\frac{\partial U}{\partial x} = 0$, which gives the critical buckling load as:

$$P_{cr} = EI \frac{\int_0^l y''^2 dx}{\int_0^l y'^2 dx} \qquad \text{Equation 1-11}$$

Assuming the deformed shape of the column after the critical buckling as:

$$y(x) = \sin\left(\frac{\pi x}{l}\right) \qquad \text{Equation 1-12}$$

which satisfies the kinematic boundary conditions. Substituting the deformed shape into Equation 1-11 we can get the critical buckling load as:

$$P_{cr} = EI \frac{\pi^2 \int_0^l \sin^2\left(\frac{\pi x}{l}\right) dx}{l^2 \int_0^l \cos^2\left(\frac{\pi x}{l}\right) dx} = \frac{EI\pi^2}{l^2} \qquad \text{Equation 1-13}$$

which is the same as the Euler's critical buckling load for pin-ended column.

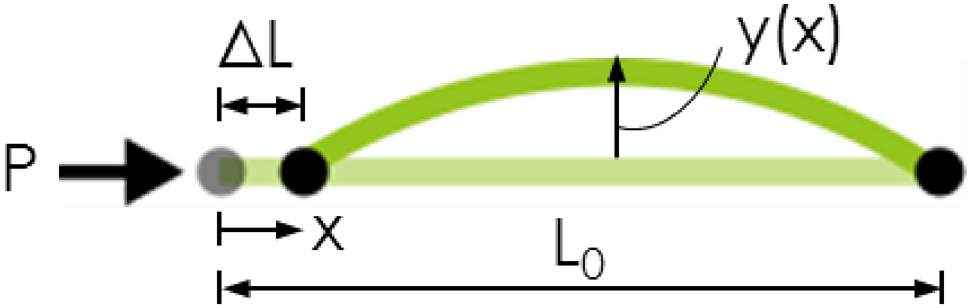

Figure 1-4: Axially compressed pin-ended column.

From the above example one can see that the strain energy developed in slender structures under external loads consists two parts: the stretching energy, which is due to extension or compression of the mid-plane and proportional to the thickness ($t$); and the bending energy, which is due to the curvature change of the structure and proportional to the cube of the thickness ($t^3$). The equilibrium shape of a structure is determined by a competition between the stretching and bending energies. Slender structures are most efficient by carrying load in a membrane stress state;

thus, when compressed they will try to deform by pure compression. However, smaller thickness makes the bending energy decreases ($\propto t^3$) faster than the stretching energy ($\propto t$). Therefore, slender structures are easier to deform by bending after the appearance of curvature, which triggers buckling. Consequently, buckling is a *bifurcation of equilibrium*. At the critical point of buckling a small variation in the control parameter makes the structure switch to another equilibrium path, or, according to Poincaré's discussion about bifurcation, leads to an exchange of stability.

However, buckling does not necessarily lead to instability, since the postbuckling equilibrium path can be either stable (i.e., positive stiffness) or unstable (i.e., negative stiffness). Postbuckling behavior is commonly categorized into: (1) symmetric stable buckling, which is often seen in compressive columns, (2) symmetric unstable buckling, which is exhibited by many thin-walled shells, and (3) asymmetric buckling, which occurs less frequently but can be found in frames. These three types of buckling are schematically shown in Figure 1-5. More examples and discussion can be found in the books by Thompson and Hunt [12, 13] and by Bažant and Cedolin [14].

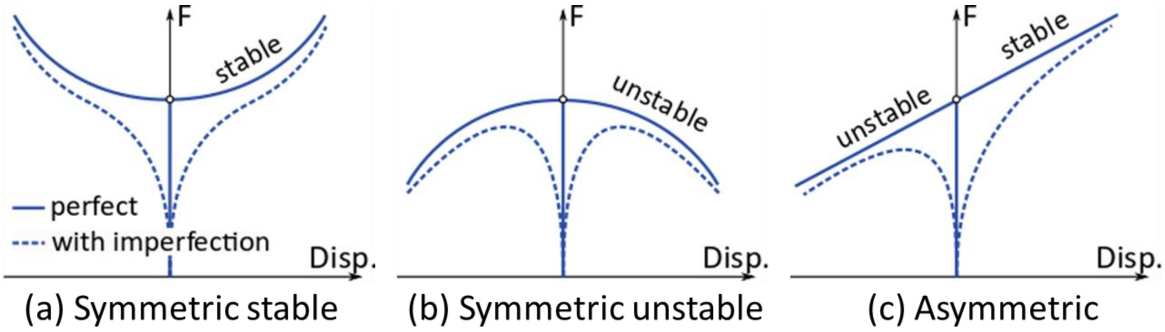

Figure 1-5: Postbuckling responses of elastic structures. (a) Symmetric stable buckling. (b) Symmetric unstable buckling. (c) Asymmetric buckling.

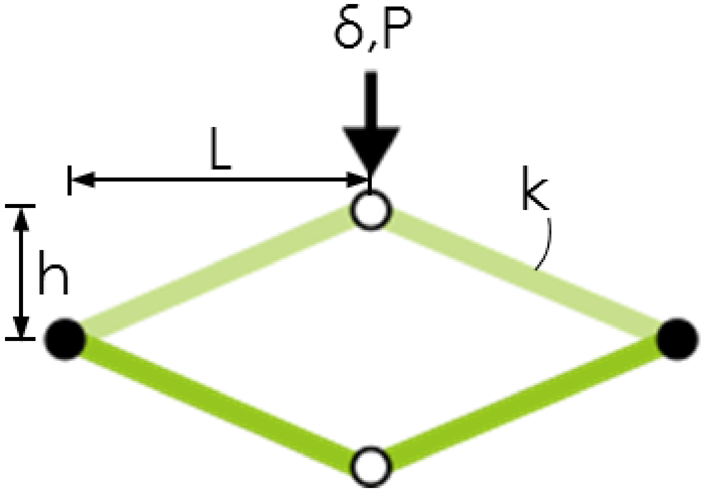

Figure 1-6: Two-bar shallow truss.

### 1.4.2 Snapping

Snapping (also called snap-through) occurs in slender structures that fail when carrying out-of-plane loads primarily by membrane stresses. In this type of instability the structure snaps from its initial equilibrium shape to an inverted equilibrium shape. Let's consider a two-bar hinge-linked rigid truss model (a.k.a. von Mises truss) for snapping, as shown in Figure 1-6, assuming the bar is rigid enough to avoid buckling. The potential energy of the truss due to the transverse load at the apex can be written as

$$U = U_s - W = \frac{1}{2}(2k\Delta L^2) + P\delta \qquad \text{Equation 1-14}$$

where

$$\Delta L = \sqrt{L^2 + (h-\delta)^2} - \sqrt{L^2 + h^2} \qquad \text{Equation 1-15}$$

Thus, the reaction force P at the apex can be solved at the equilibrium state at $\frac{\partial \mathrm{U}}{\partial \delta} = 0$. We can thus plot the force-displacement response and the second variation of the potential energy as shown in Figure 1-7, where the gray dotted lines indicate the unstable region (i.e., negative stiffness at $\frac{\partial^2 \mathrm{U}}{\partial \delta^2} < 0$).

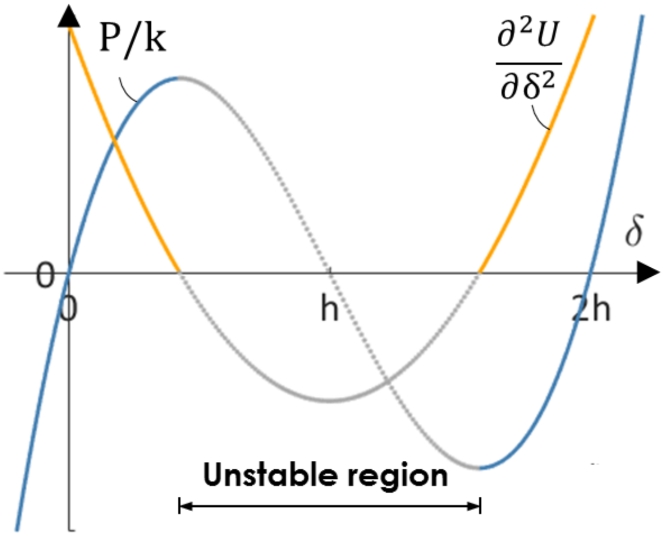

Figure 1-7: Snapping response of the two-bar shallow truss.

Comparing the strain energy formulation of a snapping shallow arch (Equation 1-14) with a buckling column (Equation 1-7), one can see that the strain energy of a shallow truss leading to snapping instability is only due to stretching and without an alternative energy path available, which results in a single continuous force-displacement response curve with no branches. Therefore, snapping is a *limitation of equilibrium*. At the critical point of snapping, a small variation in the control parameter makes the structure lose stability at its equilibrium path. The equilibrium path becomes unstable as the structure snaps, and regains stability as the structure reaches an inverted stable shape. The snapping phenomenon always leads to instability, which is often exhibited by domes and shallow arches.

### 1.4.3 Buckling vs. snapping

A slender structure can exhibit buckling or snapping depending on its geometry or loading condition. The case scenarios in Section 1.4.2 of the two-bar truss is under the assumption that the bar stiffness $k_a$ is large enough to avoid buckling. Now we consider the same truss but assume the bars are slender enough that they may buckle during loading. The response is then governed by a combination of membrane action (i.e., axial shortening of the element's center line) and bending action, where axial shortening leads to a symmetric deformation mode and bending is dominant for an asymmetric mode. The force response of the buckled bars is roughly $2P_{cr}\theta$, where $P_{cr}$ is the critical buckling load of a single bar. For a given axial stiffness of the bars, the initial height *h* of the bars controls the bending and axial interaction of the truss, as shown in Figure 1-8. When *h* is low, the truss will follow the limit point response curve since the maximum load for a snapthrough response is lower than the buckling load. As *h* increases, the slopes for both responses increase, but the limit point response grows at a faster rate. If buckling of the bars occurs at or after the limit point there will be no influence on the snapthrough behavior. As *h* keeps increasing the bifurcation buckling response intersects the limit point response before the maximum point, and the bars will buckle and follow the bifurcation path instead. The effect of the increase in *h* can also be thought as a gradual change of the governing deformation from the transverse direction of the bars to the axial direction of bars; thus changing the structure from being susceptible to snapping to becoming prone to buckling.

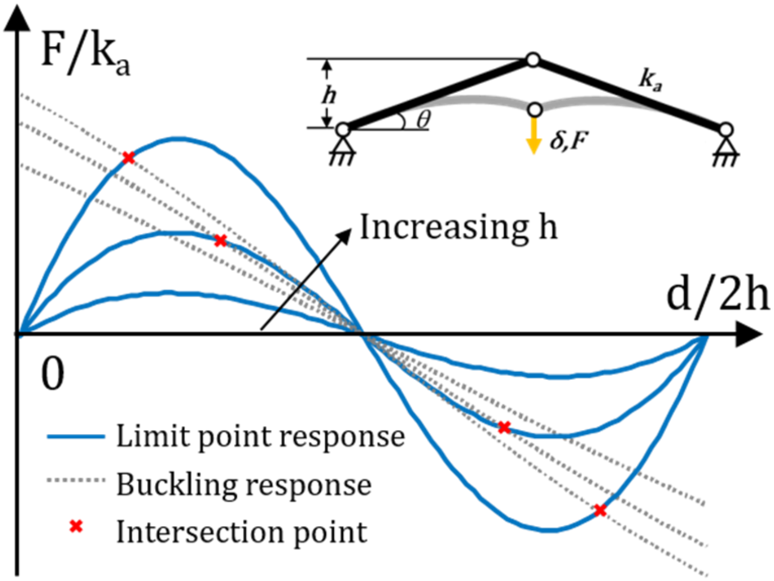

Figure 1-8: Effect of height h of a two-bar truss by considering buckling of the bars.

### 1.4.4 Common structural elements permitting buckling and snapping

Elastic instability is often seen as either buckling or snapping in slender structural members. Classical examples including the buckling of columns, plates, shells, and frames with different boundary conditions [14-24], and the snapping of von Mises trusses [25], inclined beams [26, 27] and shallow arches, for which their initial shape can be generated either by pre-compression (pre-stressing) [28-32] or pre-shaped [33-35]. If the initial shape is pre-compressed to its critical buckling stress level then the second stable shape has the same stress as the initial one, which results in a symmetric energy landscape. If the initial shape of a buckled beam is pre-shaped and stress-free, then bistability depends on its geometry and results in an asymmetric energy landscape. For a pre-shaped geometry, the rise to span ratio must not be too small to exhibit bistability, but it should also not be too large to trigger asymmetric buckling [36]. Buckled beam structures have been studied in many early works to determine their limit point response under distributed and concentrated loads [37-40], and their behavior with different boundary conditions has also been studied for: pinned-pinned [41-44], clamped-clamped [35, 45-47], and torsional spring [48] constrained ends.

Commonly seen planar structures such as curved shells in singly-curved, doubly-curved, or axisymmetric configuration also may exhibit snapthrough instability. A singly-curved shell structure is straight in the longitudinal direction with a curved cross-section, and the second stable configuration flips the original shape such that it results with a curvature in the initially straight longitudinal direction and becomes straight in the transverse direction [49, 50]. The non-monotonic response of single-curved shells is due to induced stresses during manufacturing, which can be obtained with isotropic materials thru pre-stress in the initial configuration [50, 51], or anisotropic materials (such as laminated composites) thru residual stresses [52, 53]. Multistability in thin laminates can be provided by the mismatch of the effective (or global) thermal expansion coefficients between plies, which create residual stresses during curing, either with asymmetric [54-56] or hybrid symmetric layups [57]; or caused by pre-stress induced prior to curing for symmetric layups [58, 59]. A double-curved shell that is curved in two orthogonal directions can be initially stress-free and exhibit multistability purely due to nonlinear geometric effects. The initial shape of a shell determines whether there is a change in the Gaussian curvature that develops from the coupling of bending and stretching deformation modes [60, 61]. The work done by [62] analytically demonstrated that geometry and curvatures control the existence of bistability in general planar structures with linear elastic material properties. In composites, different cured shapes of multistable laminates can be obtained, such as a bistable saddle, a twisted saddle, a tristable doubly-curved shell [63], and twisted cylindrical shapes [59, 64, 65]. Other planar form examples include shallow elliptical shells [66, 67] and circular shells [63, 68, 69]. All these forms are affected by many factors including the materials' elastic properties, degree of anisotropy, and arrangement, which define the coupling deformation characteristics [55, 70]. In nature, bistable mechanisms share the same principle. For example, the carnivorous waterwheel plant [71] and Venus flytrap [1] have doubly-curved leaves, where bending of the leave causes its mid-plane to be stretched and then to rapidly snap from an open to a closed configuration to capture their prey. Helical ribbons, which are typically the result from balancing residual stresses with restoring forces from bending and stretching, can either be in a single-curved form, like cylindrical helical or tubular shapes, or in a double-curved form, such as twisted or straight helicoidal shapes. Helical ribbons also exhibit multistability as a consequence of the mechanical anisotropy pertinent to helical deformation and geometric nonlinearity [72, 73]. Axisymmetrical caps can experience snapthrough in both thin shells [74-76] and thick shells [77] under various boundary and loading conditions. Moreover, spherical rubber balloons or cylindrical tubes also undergo limit point instabilities under inflation [78, 79].

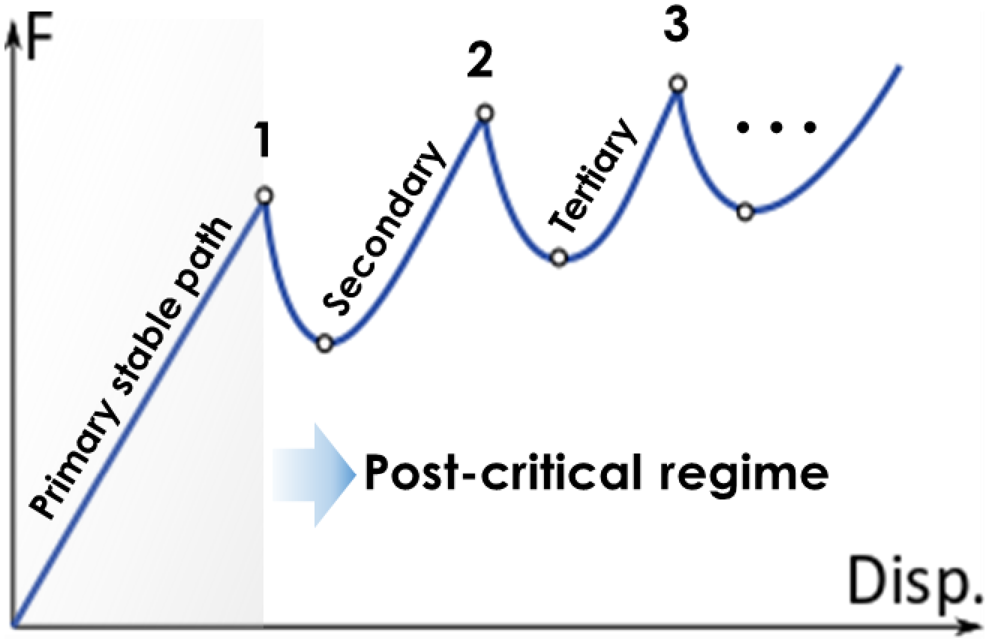

Figure 1-9: Multiple instabilities exhibited in the post-critical regime of an elastic system.

## 1.5 Post-critical response with multiple elastic instabilities

Most slender structures as discussed above exhibit a single instability in the post-critical regime, either due to snapping or buckling. The occurrence of multiple instabilities for structures in their elastic post-critical regime is relatively less common. A force-displacement response of such behavior is schematically shown in Figure 1-9. After the initial critical point the structure loses stability, and it is able to regain stability in the post-critical regime from an alternative stable equilibrium path and keep deforming until reaching the critical point of the current path, upon which it again loses stability. The structure switches to a different shape configuration according to each stable equilibrium, and the same process can keep repeating in an elastic post-critical regime that possesses multiple instabilities. This type of phenomena was first observed by Yamaki in 1984 from a series of experiments on elastic polyester cylindrical shells under axial shortening [80], and later on was also found in structures under buckling or snapping, including axially compressed plates supported by multiple longitudinal fixtures [81], strut supported by a nonlinear elastic foundation [82, 83], and strips or plates with bilateral rigid constraints [84, 85].

This post-critical behavior is fairly less studied, but a couple shared key parameters can still be drawn from structures that exhibit multiple elastic instabilities. The slenderness of a structure and the elasticity of the material are necessary to allow deformations to continue in the far post-critical regime, and the structure needs to have more than one degree-of-freedom (DOF) to provide multiple equilibrium paths that allow some DOFs to lose stability while others remain stable.

To gain further understanding of this phenomenon, let’s consider a structure with multiple DOF where each DOF is the previously discussed two-bar shallow truss which ensures the presence of an unstable response. The instability can be triggered either by buckling or snapping, as illustrated in Figure 1-10. Two condition can then be considered: that the trusses are in parallel connection or in series connection.

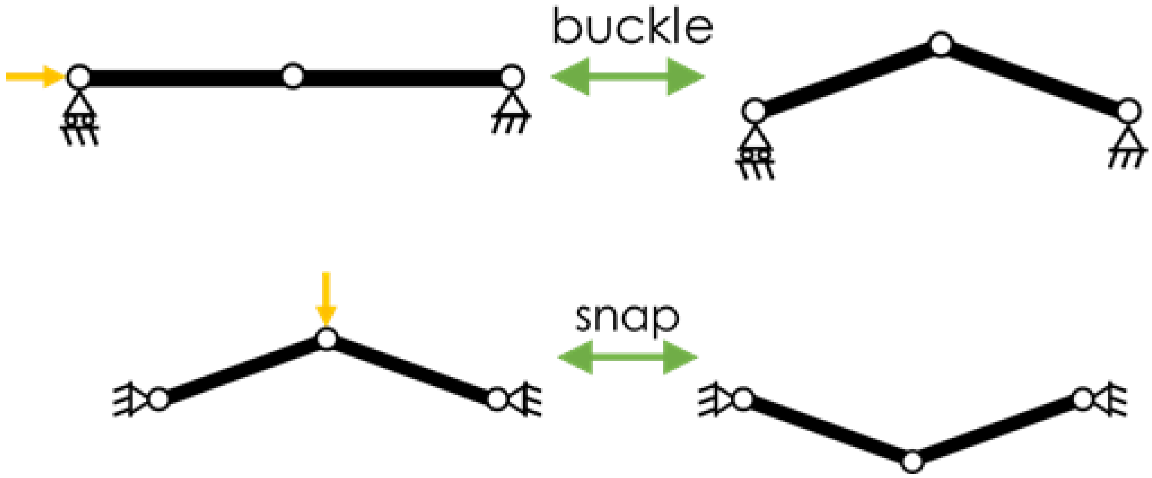

Figure 1-10: A two-bar shallow truss loses stability under buckling and snapping.

### 1.5.1 DOF in parallel connection

Recall that if the trusses are in parallel connection, the displacement is the same everywhere and the system force is a summation of forces at each truss. Let's then consider the simplest case: two identical trusses connected by a rigid bar, and a uniform displacement is applied on the bar such that it deforms the two trusses. This system is illustrated in Figure 1-11. The resistance of each truss to the load varies by the stiffness of the connecting spring $k_1$ and $k_2$, which can be considered as the imperfection in the system, and causes each truss to snap at a different time. Since the total force is a sum of forces at each truss, they system response is simply a superposition of the response from each truss; which results in multiple snap-through events in the force-displacement curve. It follows that the number of snap-through instabilities depends on the number of truss (DOF) in a system.

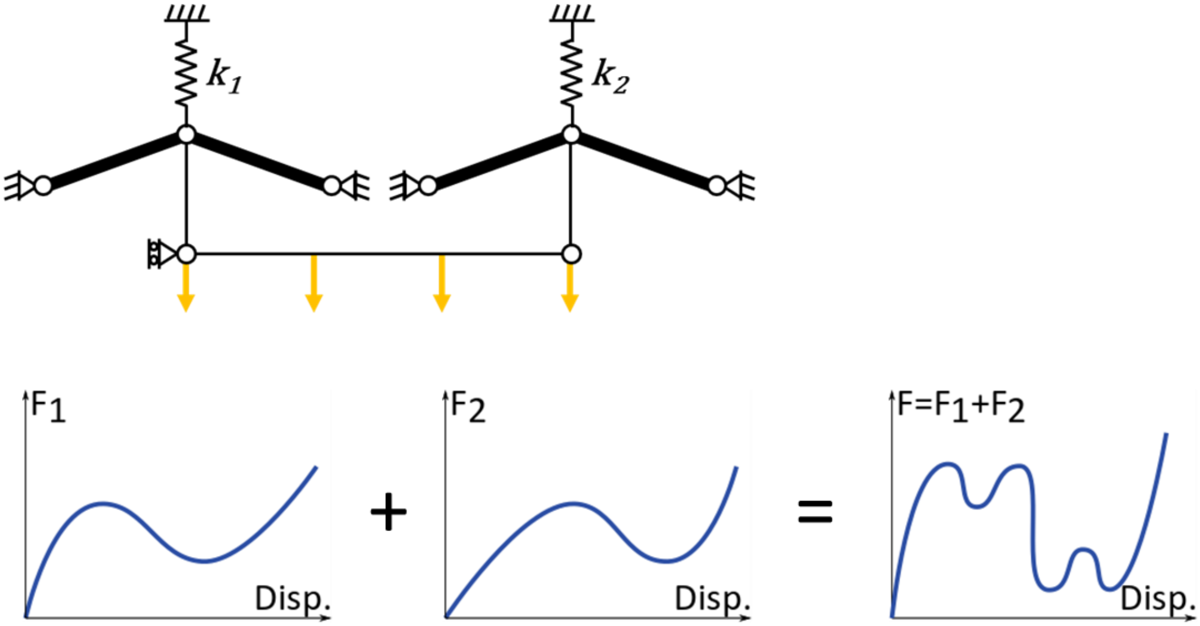

Figure 1-11: Two shallow truss in parallel connection.

### 1.5.2 DOF in series connection

For a system of trusses connected in series the force is same everywhere and the total displacement is a summation of displacements at each truss. Let’s first consider a single shallow truss connected in series with a spring of stiffness $k_b$ at its apex, as shown in Figure 1-12a. Consider that the displacement is applied at the end of the spring instead of instead of directly to the truss’s apex. When the stiffness of the spring is large most of the displacement goes to deform the truss due to the equal forces, and the resulting system behavior is similar to the situation if the displacement had been applied directly on the truss. When the stiffness $k_b$ decreases the applied displacement is shared by deforming the spring and the truss, which delays the response of the truss due to the applied displacement thus reducing the force for each incremental displacement. This has an effect of moving the limit points of the primary and secondary stable equilibrium paths farther from their stable equilibrium points (i.e., zero-force intersections) symmetrically. As a consequence, the positive stiffness decreases but the negative stiffness increases. As the stiffness $k_b$ keeps decreasing, the two stable equilibrium paths overlap. Under a small increase in the displacement beyond the limit point, the truss will snap vertically down to reach the secondary equilibrium path instead of snapping ‘back’, since the structure always wants to follow the lowest energy path. This results in an enclosed hysteresis area between the loading and unloading force-deformation paths – leading to energy dissipation.

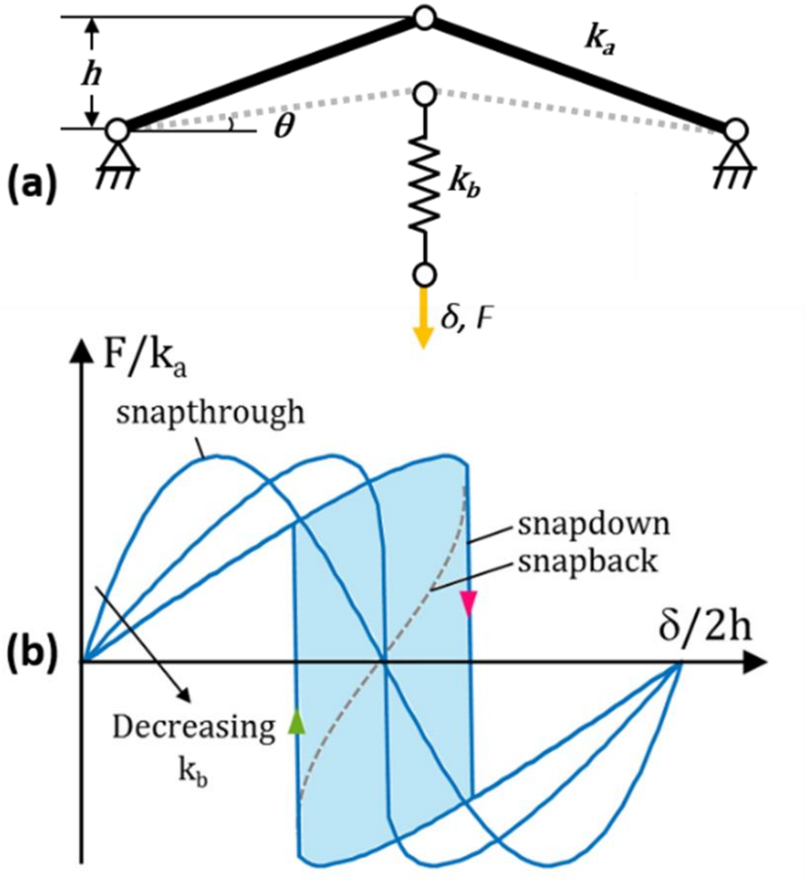

Figure 1-12: Two-bar shallow truss in series connection with a spring. (a) Schematic of the system. (b) Force-displacement response of the system.

Similarly, now considering *n* trusses connected in series by elastic springs and applying a displacement at the end of the series, as shown in Figure 1-13a. The applied displacement is shared by the trusses and the deformation of each truss started at a different increments of displacement. Therefore, each truss provides a single response path to the system response along the horizontal displacement axis.

The force-displacement of the system with *n* trusses in series connection is schematically illustrated in Figure 1-13b - Figure 1-13d, for different values of *n*. It can be seen when *n* is small, few available response paths, thus no overlap between the paths - no hysteresis. As *n* keeps increasing, a hysteresis area is formed in the response by increased equilibrium paths that are provided by each of the connected trusses and a shortened distance of the unstable ‘jumps’, thus providing energy dissipation in the loading cycle.

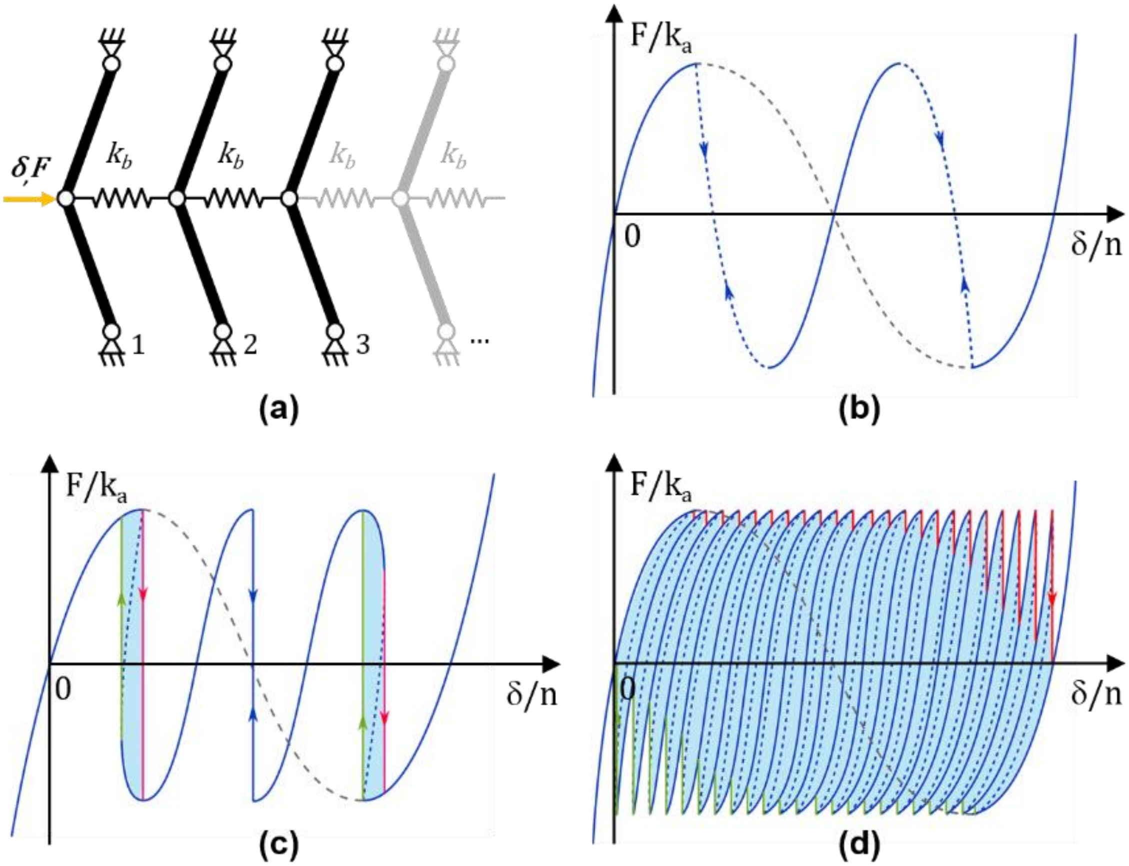

Figure 1-13: In series connected two-bar shallow trusses. (a) A chain of serially connected two-bar shallow trusses. (b) Force-displacement response path of 2 trusses (grey dashed line represents the path for 1 element). (c) Force-displacement response path of 3 trusses. (d) Force-displacement response path of *n* trusses.

The phenomenon just described can also be studied in a dynamic sense, in which the energy dissipation arises from the unstable ‘jumps’ as they generate an unbounded motion that allows the truss to travel back and forth between the two energy minima until the motion dies out due to friction, and the energy dissipation is a consequence of the release of the mechanical energy through unstable snap-through motions into kinetic energy that converts it into heat. This phenomenon, termed '*twinkling*,' has been studied thru a spring-mass chain with non-monotonic stiffness buckling elements that exhibiting oscillatory behavior of the inner masses [6-8].

Compared to structural systems that exhibit a single instability, systems with multiple instabilities in their elastic post-critical regime have more complex nonlinear responses. The multiple local potential energy extrema allow these systems, when acted upon continuous loading, to release and restore energy, have multiple unstable motions and shape configurations, etc. Responses with a post-critical behavior possessing multiple elastic instabilities give more design capabilities. The research aim of this dissertation was thus focused on controlling and harnessing this type of unstable behavior.

## 1.6 Engineering applications of elastic instabilities

As reviewed in Section 1.2, the history of studying structural instability goes back centuries, and it has been paramount for engineering design that it has been commonly aimed at preventing instability for safe design guidance. However, elastic instability have been recently reconsidered as a mechanism to provide functionality instead of defining a failure limit sate. The features of mechanical elastic instabilities to release and restore energy, set critical stress threshold, provide discrete stiffness, and allow reversible shape reconfiguration and dynamic motion make them a perfect mechanism for many practical and technological applications. These include, as summarized in Figure 1-14, adaptive structures and morphing surfaces, micro/nano electro-mechanical systems, soft robotics and devices, composites and metamaterials. Examples of how elastic instabilities are being used for engineering applications across different length and time scales, and for a variety of smart uses, are reviewed in this section. A couple recent review papers on this topic provide complimentary information to the following discussion [86-89].

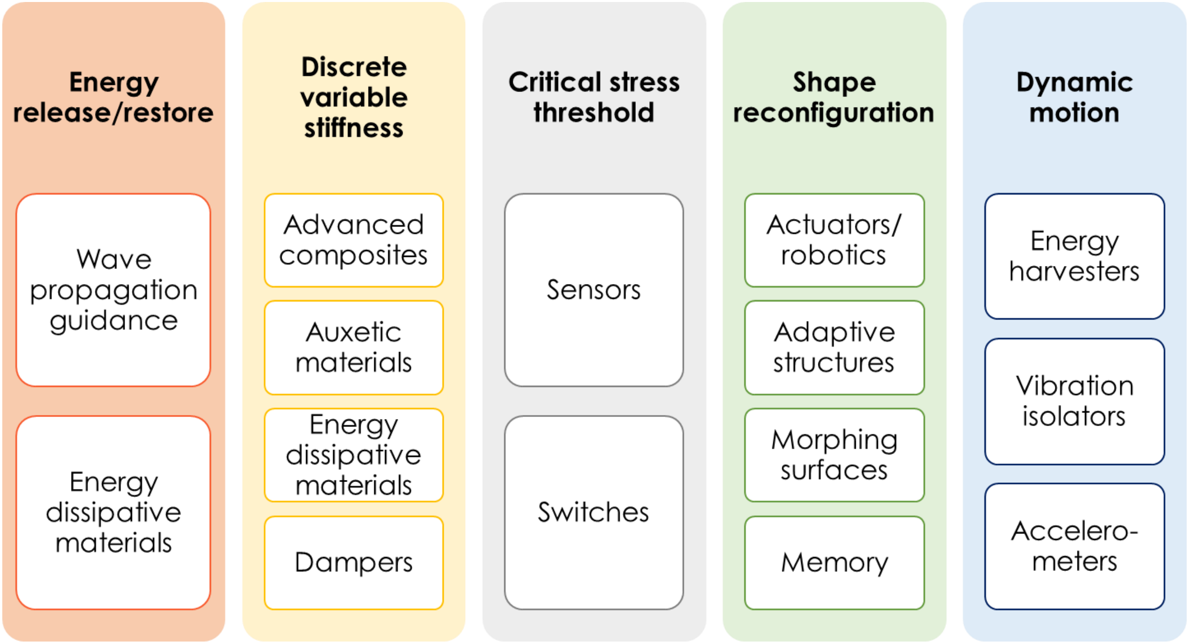

Figure 1-14: Engineering applications of elastic instabilities.

### 1.6.1 Adaptive structures

Structures with multiple stable/unstable equilibriums have multiple self-maintained discrete stable positions and undergo large and reversible shape changes in response to diverse external stimuli, including: kinematic [1], magnetic [90-92], thermal [93-95], electric [96-98], and electrostatic [99-103], during deformations over the unstable transition threshold. This ability to adapt their shape and properties in response to stimuli makes multistable structures ideal for adaptive systems undergoing reconfiguration in a programmable manner without a continuous power supply in different fields, such as architecture, robotics, and aeronautics [104]. These adaptive systems typically utilize specific material compounds exhibiting multi-physics couplings, e.g., piezoelectric, magnetostrictive, and shape memory materials, for generating functions that include shape adaptation, actuation, sensing, and energy harvesting [105].

In morphing surface applications, a structure's shape changes in order to adapt to different environmental conditions. This feature is used often in aerodynamic designs, which also require light weight and high-strength design solutions. Multistable composite laminates are thus favored in the design of morphing structures due to their high stiffness-to-mass ratio, long fatigue life, and could also consist fewer components [106, 107]. Different concepts have been investigated to introduce multistable structures into piezoelectrically actuated morphing applications [96, 97, 108-113], and aircraft systems such as wings, air inlets, blended winglets or wind turbines [94, 114-117]. Geometric change between stable branches provides alternative stiffness; therefore, approaches for varying stiffness in multistable composite laminates have also been exploited [118, 119]. Several review papers can be found related to this topic, including the use of bistable composite laminates for morphing structures [120], morphing structures for aircraft [106, 121-123] and automobile uses [124], and stiffness variability for morphing applications [125, 126].

Deployable structures, which can be self-maintained in a significantly compressed shape as a consequence of multistability for ease of transportation storage are ideal for space [127-129], robotic [130-134], and architectural applications [135-137]. A commonly used deployable multistable structure is a bistable tape spring for deployable reflectors [138, 139] and antennas [140, 141]. Monolithic deployable structures that are load bearing and possess multiple, predictable, activated geometries have been shown to be possible via 3D printing from a flat surface incorporating a hierarchical framework, where a bistable actuator serves as the building block [142]. For example, a deployable structure using soft composite actuators for hinge-like movement was developed as a prototype for a deployable mirror to reflect sunlight onto a solar panel [143]. Tensegrity structures are perfect candidates for deployable structures, as they can change their shape and size from a compact state to the service state with improved packaging efficiency and a reduced number of joints [144]. They are also able to capture the essential qualitative features of cytoskeletal shape distortion in adherent cells and to underlie the shape stability of the cytoskeleton [145-147]. In robotic applications, multistable tensegrity structures are used for the locomotion of robots [131-134] and grippers [148-150]. Designs based on multistable origami, bistable cylindrical shells with Kresling [151] or Miura patterns [152] have been studied and shown to be foldable in the axial direction to a flat state, while keeping their axis and internal envelope like a bellow. Moreover, Kresling patterned multistable origami actuated by DC motors have been used to achieve forward locomotion and steering for robots [153, 154].

### 1.6.2 Sensing and actuating devices

For sensing applications, the tunable unstable transition limits between stable states are often used for threshold-type sensing. For example, latching accelerometers that can function without electrical power for shock sensing [155, 156], accelerometers capable of accurate threshold sensing [157-159], and a bidirectional acceleration switch using magnetic fields based on a tristable mechanism [160]. For actuation applications, multistability allows a system to maintain distinct positions while saving energy consumption, since continuous driving power is not required. For example, a bistable response thru the use of a dielectric elastomer for minimum energy structures has been proposed to achieve large angular deformations due to small voltage-induced strains [161]. Shape memory actuators using bistable metallic foils have been proposed as switches for tactile graphic displays [162]. An electrostatic-driven large-displacement micro actuator incorporating multiple serially connected bistable arch-shaped beams was shown to have improved larger stable displacements compared to conventional comb drive actuators with low voltage input [163]. An energy saving actuator with multistable composites and electromechanical motor was exploited for exoskeleton applications [164]. A multistable linear actuation mechanism articulated with electroactive polymer actuators was shown to accurately transform angular displacement into rectilinear displacement [165].

The nature of bistable mechanisms is ideal for switch-type applications. Examples include mechanically bistable switching micro-devices [166]; mechanically tristable switch mechanisms (based on a laterally moving electrostatic curved-electrode actuators) configured in a ‘true’ single-pole-double-throw configuration [167]; a bistable micro-actuator that uses a laser heated shape memory alloy for selective addressing capability in optical filters [168]; a bistable micro-hemisphere actuated electrostatically to switch between two stable curvatures for valve design [169]; a bistable thermos-pneumatic actuated micro-valve that can withstand high pressure loads [170, 171]; a nonvolatile bistable optomechanical switch comprising of two parallel buckling waveguides for all-optical writing and reading processes that involves relatively strong and relatively weak optical pulses with no maintenance power requirement [172]; a silicon-based high-frequency nano-mechanical device capable of switching controllably between two states in the hysteretic nonlinear regime at room temperature for a low-power and high-speed mechanical switch [173]; a chevron-type bi-stable micro-actuator optical switch [174]; and a bistable dc-switch designed for an implantable electrode multiplexer for medicine delivery [175].

For memory applications, instead of storing the information in the form of a packet of electric charge, the single bits of information (“0” and “1”) can be retained by mechanically bistable elements having two stable states separated by a strain energy barrier. This concept was first proposed 40 years ago [176] and later developed by [177, 178] using an electrostatically actuated silicon micro-bridge, in which the read and write operation is performed by sensing the capacitance of the two stable states of the bridge. In recent applications, a nano-dot silicon electromechanical memory device was incorporated into a bistable floating gate beam to realize about 1 GHz switching speed and nonvolatile memory operation [179]; high-speed nano-mechanical memory cells that consist of clamped beams that are driven into transverse oscillation with the use of a radiofrequency source have been explored [180]; a static memory micro-mechanical device was designed using a bistable nanowire that is actuated between two stable positions in order to store information in a mechanical way [181, 182]; and a micromechanical static memory device based on a bistable buckling beam with on-chip readout was shown to perform stable data storage after a stress-relaxation “burn-in” period [183].

### 1.6.3 Energy harvesting devices

Harnessing elastic instabilities has found its way towards the enhancement of energy harvesters by using the snap-through behavior of pre-buckled elements to introduce nonlinear behavior to linear generators, and thus overcome bandwidth limitations for higher efficiency. Jung and Yun [184] proposed an energy-harvesting device with buckled bridges to up-convert the generator’s resonate frequency under low-frequency vibration excitation. An experimental investigation conducted by Sneller et al. [185] showed that a post-buckled piezoelectric beam with attached central mass can achieve a broadened the frequency range over snap-through under a lower harmonic forcing amplitude. Enhanced power generations have also been found when thin piezoelectric beams are used in their buckled configuration under random vibrations [186] and chaotic vibrations [187]. For a bistable system with non-monotonic response under vibrational load, three distinct dynamic operating regimes can be obtained as the excitation amplitude increases: intrawell vibrations, aperiodic or chaotic vibrations between wells, and periodic interwell oscillations. Depending on the excitation level and frequency, these devices can exhibit either periodic or chaotic inter-well vibration, have been shown promising performance as used for nonlinear energy harvesters. Further, the snapthrough is triggered independently from the external excitation for a wider bandwidth [188, 189], which allows operating under low frequency vibrations [190] or even quasi-static input [191-193]. A detailed review on the dynamics of bistable structures for vibration, energy harvesting, and sensing can be found in [194, 195].

### 1.6.4 Energy dissipative/absorptive materials

Elements that experience elastic instabilities have be increasingly used as the microstructures in design novel materials with tunable functionality. One of the prominent properties that achieved materials based on instabilities is high energy dissipation/absorption/damping. For example, enhanced overall stiffness and mechanical damping can be achieved in composite materials by adding negative stiffness inclusions in a positive stiffness viscoelastic matrix [196-202]. Using a snap fit structure as the unit element in design mechanical materials can achieve tunable compressive behavior with energy absorption [203]. An elastomeric architected material with unit strut has independently tailorable compression and shear response with negative shear stiffness [204]. A 3D printed cellular material at the millimeter-scale was demonstrated to yield a serrated force–displacement behavior similar to martensitic transformations in shape memory alloys for large energy dissipation in 2D [205] or 3D configurations [206, 207]. A honeycomb consisting bistable negative stiffness elements fabricated in nylon 11 using selective laser sintering has been shown to exhibit relatively large positive stiffness, followed by a stress plateau region with hysteresis, with full recovery after compression [208, 209]. Further, by changing the geometry of the unit cell, the sequence of snapthrough deformation can also be predicted and controlled [210]. Shape reconfigurable materials based on bistable units have been shown to achieve independent multi-axial deformation with high volumetric and morphological change in 1D, 2D and 3D configurations, with energy dissipative behavior due to negative stiffness [211]. As final examples, bistable elements with two asymmetric energy wells have been used as microstructures in design metamaterials that allow energy trapping under tension [212] and compression [27, 213-215].

## 1.7 Problem statement and research hypothesis

In ordinary elastic structures and materials, the functional states are stable (i.e. positive definite) for load carrying purpose, and strain energy is simply accumulated in deformed objects and could eventually leads to damage or failure. As described in section 1.5, the presence of multiple elastic instabilities in a structure or solid allow strain energy imposed from external mechanical deformations to store during the stable states, and then release during the unstable states through dynamic motions. Therefore, the research hypothesis behind this dissertation is that if multiple elastic instabilities in a mechanical system are harnessed, then energy transduction in bio systems can be mimicked to design smart structural systems that allow conveying strain energy to drive predefined responses or to do desirable work. This process is illustrated and compared to the photosynthesis and respiration processes in biological systems in Figure 1-15.

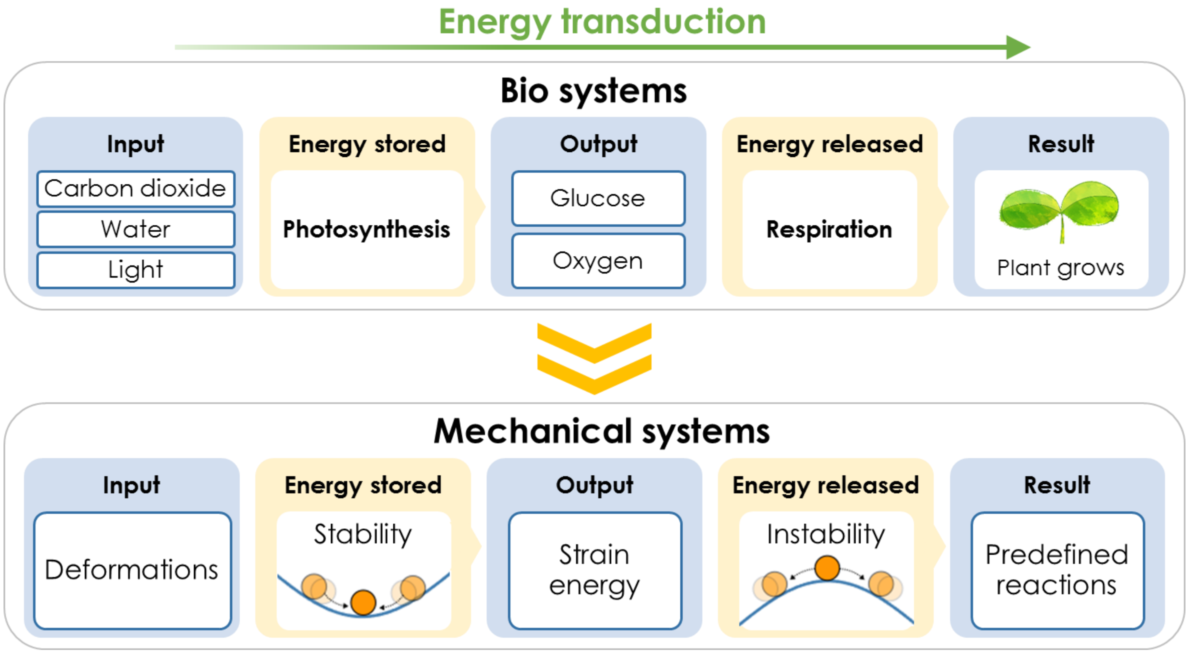

Figure 1-15: Energy transduction in biological and mechanical systems.

The research objectives in this dissertation aim to address two challenges through mechanical energy transduction: (1) harvest electric energy from low frequency quasi-static mechanical deformations, and (2) dissipate energy in materials subject to cyclic shear deformations in a recoverable and rate-independent manner.

### 1.7.1 Piezoelectric energy harvesting from quasi-static mechanical deformations

The basic concept of energy harvesting is to generate electric power from ambient mechanical energy. The most common energy harvesting approach is to use piezoelectric materials, whose direct piezoelectric effect allows the materials to transform mechanical strain into electrical charge. Many ambient mechanical energy sources can induce deformations in solids and structures that develop strain energy, including forces, displacements, pressures, vibrations, temperature variation, and etc. Sources of ambient mechanical energy available for conversion include forces, displacements, pressures, and vibrations. To date, vibration is the most used and efficient mechanical energy source since it can generate large strain changes at high rates and thus lead to relatively high-level continuous power generation. However, vibration-based energy harvesters have a narrow operating frequency bandwidth and perform poorly under low frequency excitation sources [194, 216, 217]. Low frequency quasi-static (<<1 Hz) deformation sources are very common in daily life – from deformations in large civil structures to biomechanical motions such as human walking or heart beats [218]. Yet, much less attention has been paid to harnessing power from low frequency excitation sources because, contrary to vibration, they are well below the resonance frequency of piezoelectric materials and generate small strain changes at low rates [219].

Since the unstable motions due to elastic instabilities are rate-independent of the externally applied deformation, the hypothesis is that use of elastic instabilities as the fundamental mechanism for energy harvesting can overcome the disadvantage of low frequency deformations to effectively harvest energy directly from quasi-static mechanical sources.

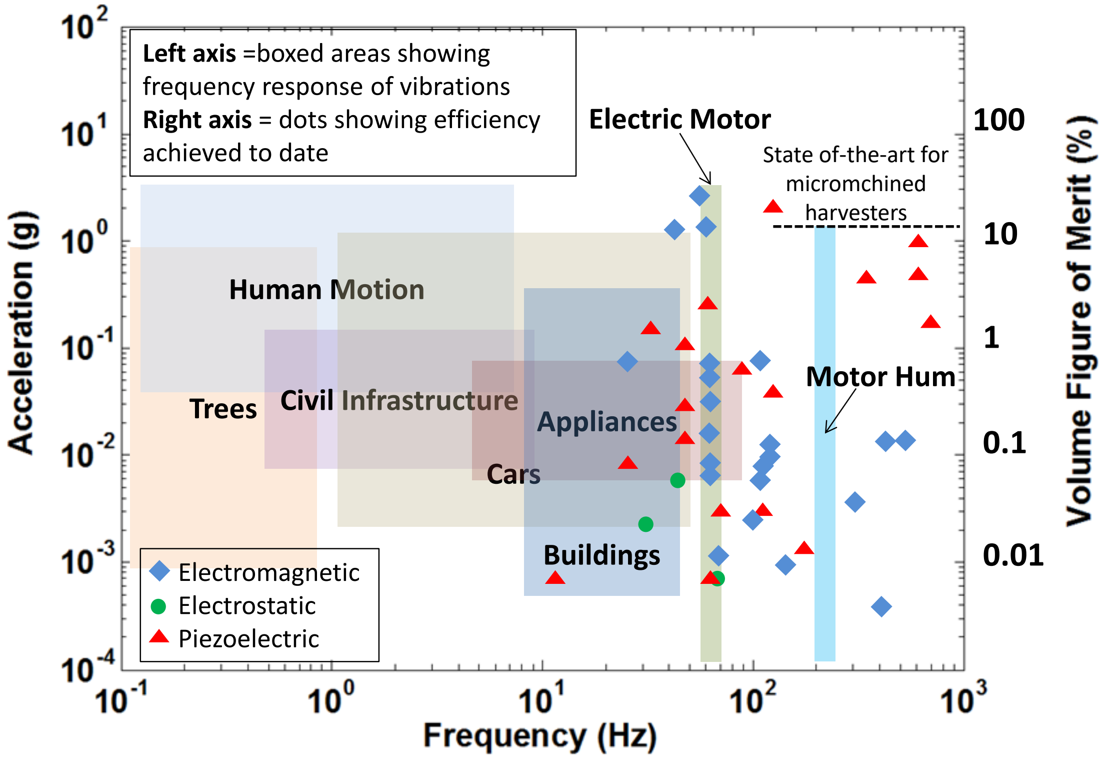

Figure 1-16: Frequency response of the vibrations found in various applications [220].

### 1.7.2 Energy dissipation in materials subject to cyclic shear deformations

Energy dissipation, an important and desirable material property to be used in mechanical and civil engineering applications, consists of an irreversible energy loss in solids and structures as a result of the conversion of mechanical energy into heat [221]. The ability to dissipate energy enables materials to undergo large deformations at limited stresses, which is imperative for enhancing damage tolerance. The common mechanisms to achieve this goal, such as plastic yielding (associated with permanent deformations) and rate dependent viscosity, perform poorly under repetitive loading cycles or low strain-rate deformations. Recently, elastic instabilities are attracting increased attention for use as the fundamental mechanism in the design of energy dissipating/absorbing mechanical metamaterials [87-89] due to their rate-independent and motion-recoverable nature. Many material porotypes have realized this concept for uniaxial tension [212] or compression loading conditions [27, 203, 205-209, 214, 215], but little attention has been given to shear behavior.

Shear deformations often occurs in materials when subjected to relative in-plane motion. Materials that can dissipate energy under shear are necessary for public safety and personnel protection purposes, and could be deployed in applications such as helmets to prevent energy transfer to the brain due to glancing blows, backpacks to limit impact on the wearer, and civil structures to limit damage from ground motions (see Figure 1-17).

It has been demonstrated that the connection of a large number of snapping elements in series can lead to energy dissipation. Thus, the research hypothesis is that by using elastic instabilities as the fundamental mechanism, high energy-dissipative materials can be designed in a recoverable and rate-independent manner under shear deformations.

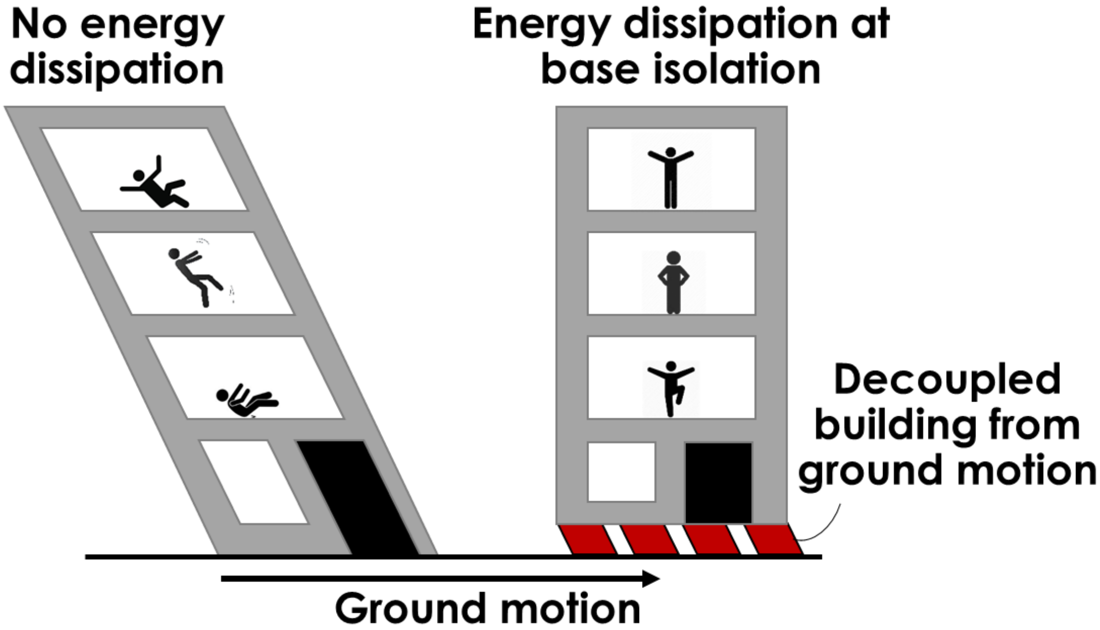

Figure 1-17: A building with and without shear energy dissipation at the base.

## 1.8 Overall research approach

The presence of multiple elastic instabilities in structural elements was used as the fundamental mechanism for all design concepts. For each of the problems stated in Section 1.7, integrated novel structural systems were proposed. Multi-material 3D printing was used to manufacture table-size prototypes to serve as physical demonstrators of the novel structural concepts, and tested experimentally to verify the expected behavior. For each structural system, a theoretical model was developed based on energy methods, and numerical simulations were carried out by finite element analyses (FEA) using the commercial software package ABAQUS. After validating the theoretical models and numerical simulation with experiments, they were used to predict system response and explore the design space for each concept.

## 1.9 Dissertation outline

This dissertation presents an investigation on the nonlinear post-critical behavior structures with multiple elastic instabilities such as to harness this behavior for energy transduction in mechanical systems. This dissertation consists of six chapters and is organized as follows.

Chapter 1 gives a general introduction to the topic of elastic structural instabilities, summarizes current developments and applications on their use, states the two research problems and hypotheses guiding the study, and discusses the general research approach.

Chapter 2 proposes the concept for piezoelectric energy harvesting from low frequency quasi-static mechanical deformations by using the nonlinear response of axially compressed bilaterally constrained columns that are coupled with the electro-mechanical effect of piezoelectric materials. Existing strategies and relevant investigations of the topic are reviewed, two design models are proposed, and the detailed methodology to investigate the proposed systems through 3D prototyping, experimental evaluations, theoretical analyses, and numerical simulations are presented. The content for design I of this concept has been published in [222], and the content for design II was published in [191, 223, 224].

Chapter 3 proposes a concept to dissipate energy in materials subjected to cyclic shear deformations, by using the sequential snapthrough behavior of architected materials that feature inclined beams in their microstructure. Similar to Chapter 2, the existing strategies and relevant investigations on the topic are reviewed, two design layouts are proposed, and the detailed methodology to investigate the proposed systems through 3D prototyping, experimental evaluations, theoretical analyses, and numerical simulations are presented. The content of this concept have been published in [225].

Chapter 4 presents the results the proposed energy harvesting concept from two structural models: a bilaterally constrained prismatic column (BCPC) with a bonded PZT film layer, and a bilaterally constrained non-prismatic column (BCNC) with a PZT oscillator. Experimental results from the prototyped systems show that, due to the controlled and tailored postbuckling behavior, effective energy harvesting from quasi-static deformations was obtained with enhanced performance. A theoretical model and numerical investigations are shown to have good agreement to the experiments, predict the behavior, and used to explore the parameter space of the system with different form-factor requirements.

Chapter 5 presents the results the proposed energy dissipative material concept under two loading conditions: half-cycle and full-cycle shear deformations. Experimental results from 3D printed material multi-unit prototypes verify their recoverable and repeatable response and rate-independent energy dissipation under cyclic shear loading. Numerical results predict the behavior of the single-beam unit element with different geometries, and theoretical results obtain the optimal energy dissipation of the multi-unit material systems for a given unit geometry. Results from parametric studies based on the theoretical model are presented to explore the design space of the proposed materials.

Finally, the findings of the study presented in this dissertation are concluded in Chapter 6, and possible future works extended from the current investigation are also discussed.

# Chapter 2

# QUASI-STATIC ENERGY HARVESTING – CONCEPT AND METHODS

## 2.1 Background

### 2.1.1 Energy harvesting from quasi-static loads

Structural vibrations, coupled with piezoelectric transducers, are the still most used and efficient mechanical energy source since they can generate large strain changes at high rates and thus lead to relatively high-level continuous power generation. However, several studies have investigated harvesting energy directly from quasi-static loading conditions, a common situation in large civil structure deformations to biomechanical motions, and which can be sufficient to power low energy budget devices. Theoretical and experimental studies on PVDF (polyvinylidene fluoride) film energy harvesters for MEMS (micro-electro-mechanical systems) power sources have shown that the maximum power output of a 1 $cm^2$ piezo-film is in the range 0.0025-0.37 μW, depending on its geometry and thickness [226]. This level of harvested power could be sufficient for a DNA (deoxyribonucleic acid) detection chip, which requires 10 mW to activate twice a day [227]. Energy harvesting from arterial blood pressure was investigated theoretically and numerically, and the results show that about 20 μW of peak power can be converted at a blood impulse rate of 0.89 Hz [228]. It is widely agreed that ~ 100 μW of continuous power is the minimum requirement to operate a single sensor. However, as technologies advance, some sensors, or *in vivo* bio-MEMS, are highly energy-efficient and can operate at a power budget level < 1 μW [229, 230]. For example, a data computation and logging system for sensing applications developed at Michigan State University can achieve data processing and storage at power levels below 1 μW [231]; and a brain micro stimulation device for treatment of Parkinson's disease, epilepsy, spinal cord injuries, and neurological disorders requires less than 1 $\mu$W to stimulate a single neuron [232].

### 2.1.2 Energy harvesting using buckling instabilities

The new vision of harnessing structural instabilities has found its way towards the enhancement of energy harvesters by using the snap-through behavior of pre-buckled elements to introduce nonlinear behavior in linear piezoelectric generators, and thus overcome bandwidth limitations for higher efficiency. Jung and Yun [184] proposed an energy-harvesting device with buckled bridges to up-convert the generator's resonate frequency under low-frequency vibration excitation. An experimental investigation conducted by Sneller et al. [185] showed that a post-buckled piezoelectric beam with attached central mass can achieve a broadened the frequency range over snap-through under a lower harmonic forcing amplitude. Nano-scaled buckled PZT ribbons reveal an enhancement in their stretchability by an order-of magnitude, and an amplified piezoelectric effect of up to 70% [233]. A random analysis was conducted on a controlled buckling structure for energy harvesting that shows the optimal locations of electrodes are robust to the upper bound of environmental excitation [234]. Controlled buckling of piezoelectric beams were used to generate electricity from the weight of passing cars and crowds [235]. Enhanced power generations have also been found when thin piezoelectric beams are used in their buckled configuration under random vibrations [186] and chaotic vibrations [187]. Other attempts to expand the operational bandwidth of vibration harvesters include magnetic interactions [186, 236, 237], tunable resonators [238], amplitude limiters [239] and other concepts [194, 240]. However, even with a widened operational band frequency, all the previously noted harvesters are still limited to an external vibration input, and are thus inadequate for operating under quasi-static input sources.

### 2.1.3 A quasi-static energy harvester: concept, prototype and limitations

A concept for a quasi-static micro-energy harvester that made use of buckling instabilities originally proposed by Burgueño and Lajnef [192, 241] is shown in Figure 2-1. The structural model consists a bilaterally constrained prismatic column (BCPC) with a cantilever configured piezoelectric energy transducer attached to the mid-length of the column. This model demonstrated that the mechanism of buckling instabilities provided by a bilaterally constrained axially compressed columns can be used as mechanical triggers to transform external quasi-static global displacement input (< 1 Hz) to local high-rate motions and excite vibration-based piezoelectric transducers for energy harvesting devices [192, 241, 242]. The local high-rate motions are due to the local bifurcations, which are sensitive to their location along the column. A small local motion may generate a large acceleration at that location but it could correspond to a relatively small global kinetic energy release.

In the original energy harvester model, the buckling location at each mode transition changes along the column length. Thus, the cantilever configured piezoelectric energy transducer cannot be strategically placed on the column for optimal energy generation, and the performance of energy generation was affected. Therefore, two energy harvester designs were developed based on this concept in this research to improve the original design.

In the first design, the cantilever configured piezoelectric energy transducer was replaced by a piezoelectric layer bonded to the column surface. The continuously elastic postbuckling deformation of the column provides axial strain directly for the bounded piezoelectric film to generate electric power. For the second design, the aim was controlling the location of local buckling events at each mode transitions such as to strategically place the piezoelectric oscillator for enhanced energy harvesting performance. Each of these two design strategies are discussed in details in the section 2.3.

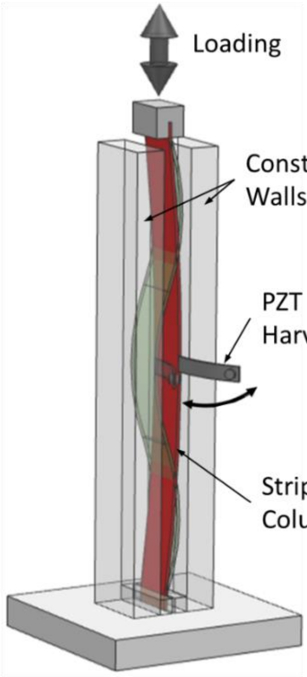

Figure 2-1: Original energy harvester design prototype: bilaterally constrained prismatic column (BCPC) with PZT oscillator [192].

## 2.2 Postbuckling behavior of bilaterally constrained columns

### 2.2.1 Development of local contact zone

Multiple buckling instabilities behavior in the elastic postbuckling regime of axially compressed slender columns can be obtained by the provision of bilateral rigid constrains (i.e., walls) to the transverse deformations of the element [85, 243, 244]. A homogeneous prismatic column with symmetric boundary conditions and subjected to an axial compressive load reaches its first critical stability point and buckles with a maximum transverse deformation amplitude at mid-span. If the column is provided with continuous rigid parallel lateral supports, a contact zone develops between the element and the constraints, which grows from a condition of point contact to line contact with increasing load [243]. The first few buckling modes for the case in which the axially loaded column is initially placed adjacent to one of the constraining walls are shown in Figure 2-2, which shows the transition from point to line contact for the different buckling modes. After a line contact condition has developed, the bending moment vanishes within this region due to the lack of curvature and independent boundary conditions form for the segment, equivalent to clamped-clamped ends in an Euler column, develop. Local buckling occurs in the longest flattened region when the critical load within this segment is reached [3, 85, 243]. The higher order buckled configuration forms after the buckling event corresponds to a lower state of energy.

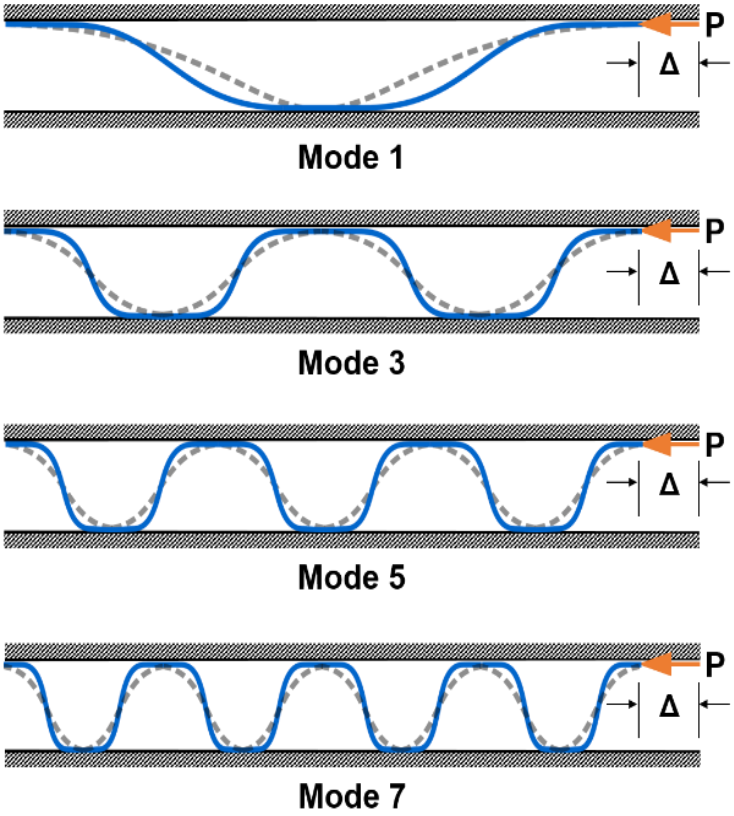

Figure 2-2: Schematic of the elastic postbuckling response of an axially compressed bilaterally constrained column at the first few buckling modes, with profiles for point contact (dashed line) and line contact (solid line).

### 2.2.2 Buckling configuration based on energy considerations

For an axially compressed column the equilibrium shape is determined by a competition between the column's bending and compressive energy due to the external applied force. For a bilaterally constrained column, the shape during the deformation process is divided into flat and curved segments before each critical buckling mode transition (Figure 2-2). The key parameter triggering the buckling mode transitions is the length of the isolated line contact sections [3, 243]. Taking the first buckling mode as an example (shown in Figure 2-3), the column total length is defined $L_0$ and the curved and flat segments have projected length $L_2$ and $L_1$, respectively. For a given end shortening $\Delta L$, the constraint on the column total length yields $\Sigma L_2 + \Sigma L_1 = L_0 - \Delta L$.

At the same total strain energy level (i.e., the same $L_2$), three conditions can be considered to form different buckled equilibrium shapes by redistribution of the flat segments (i.e., $\Sigma L_1$) along the column: symmetric, upper limit, and lower limit cases [3]. For a buckled column in an ideal condition, a symmetric wave shape is assumed to accommodate the end shorting $\Delta L$, with the flat segment symmetrically arranged next to curved segments [85, 243]. Based on Euler's buckling equation the critical buckling load is inversely proportional to the critical length [245]; that is, the longer the column the easier it is for it to buckle. Thus, upper and lower limits can be considered for the generation of mode transitions. In the upper limit, each straight segment needs to be as short as possible, which makes instability more difficult, and they are thus distributed evenly at each line contact zone. In the lower limit case, which is opposite to the upper limit one, the straight segments mere into a single line contact zone at the middle of the column to form a single straight segment and thus facilitate buckling.

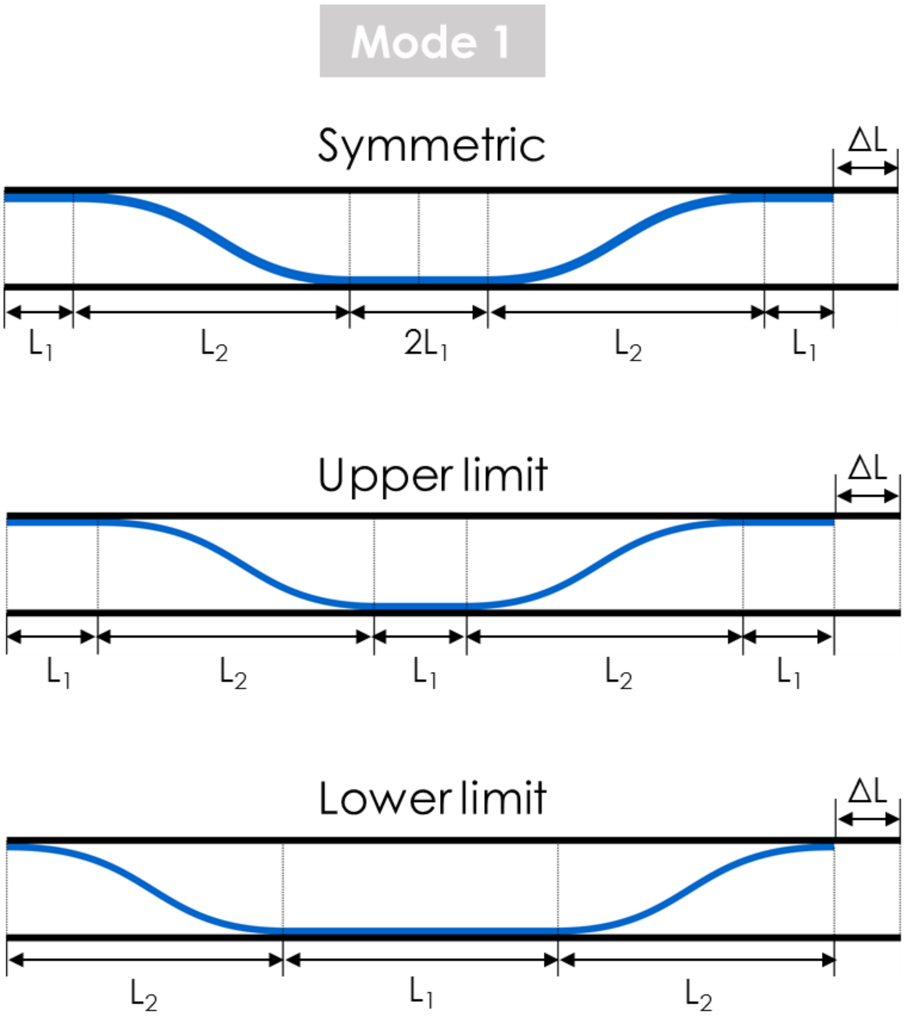

Figure 2-3: Schematic depiction of different buckling shapes for modes 1 based on energy consideration: symmetric case, upper and lower limit cases.

The buckling shape of mode 1 and mode 3 for bilaterally constrained prismatic columns under a symmetric assumption is schematically shown in Figure 2-4. It can be seen, that for mode 1 the longest straight segment first forms at the middle section of the column, where buckling occurs. However, three equal length straight segments form in mode 3, and buckling can be triggered in any of these segments. In addition, asymmetry occurs due to the presence of friction between the column and the side walls [85, 243] and causes the buckling shape to be sensitive to imperfection. Therefore, the maximum buckling location cannot be controlled in prismatic columns.

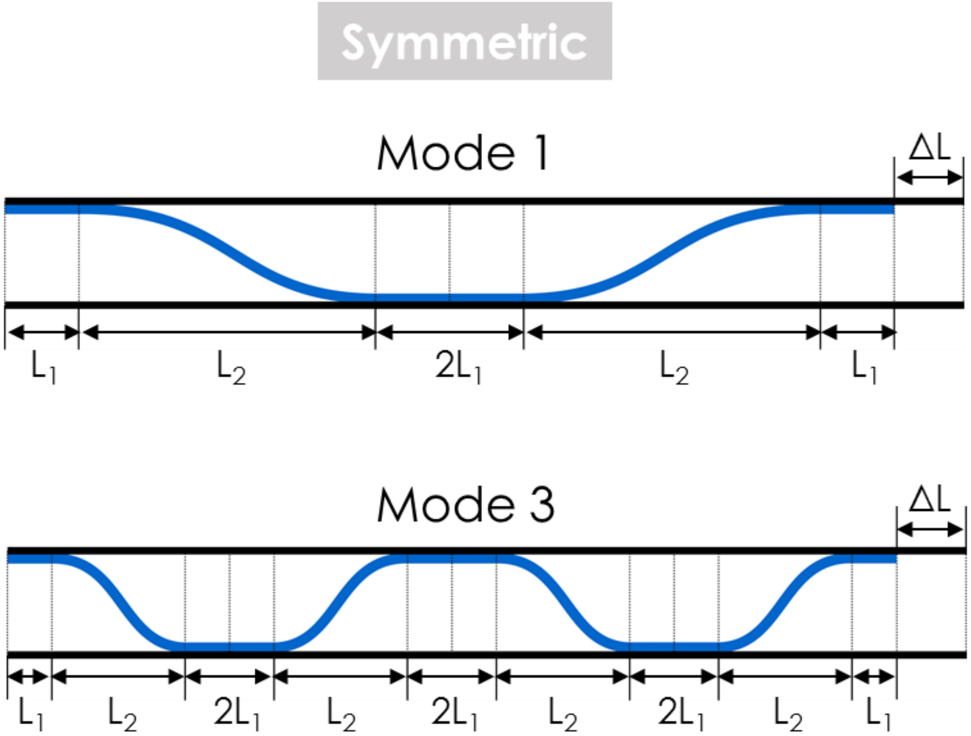

Figure 2-4: Schematic depiction of symmetric buckling shapes for modes 1 and mode 3.

### 2.2.3 Tailoring postbuckling response through non-uniform stiffness

Studies related to the stability of non-uniform columns and the advantage that they could offer for controlling static and dynamic response date back to more than a century. However, most efforts have focused on determining the critical buckling load of non-uniform beams/columns/rods subject to varying axial loads and boundary conditions with [246, 247] or without laterally restraints [248-251] through closed-form solutions, and also via a semi-analytical procedures [252] and a higher-order perturbation approach [14]. Details on these solutions can be found in reference [253]. The use of non-uniform strip elements for controlling static and dynamic response by strategic selection of non-uniform cross-section geometry and materials has also been explored [254-257]. However, the studies conducted thus far focused on the onset of buckling and up to the first bifurcation in the postbuckling response. Yet, recent related studies by our group [258, 259] have shown that the elastic postbuckling response of cylindrical shells can be tailored by introducing non-uniform stiffness distributions. It follows that the multi-stable response of non-prismatic columns in the far elastic postbuckling regime remains unexplored and that non-prismatic column designs are a viable way to tailor the desired elastic instabilities.

## 2.3 Model designs

### 2.3.1 Design I - Bilaterally constrained prismatic column (BCPC) with a bonded PZT film layer

Eliminating the protruding PZT oscillator and replacing it as a PZT film layer bonded directly to the column surface would permit future miniaturization and packaging of the harvesting device, as shown in Figure 2-5. The axially compressed BCPC allows a continuously large deformation in its elastic regime, thus providing axial strain for the bounded piezoelectric film to generate electric power. A theoretical model was developed to predict the corresponding strain of the buckled configuration of the strip, and thus calculate the electrical energy generation. An experimental investigation and finite element simulations were conducted to validate the theoretical results.

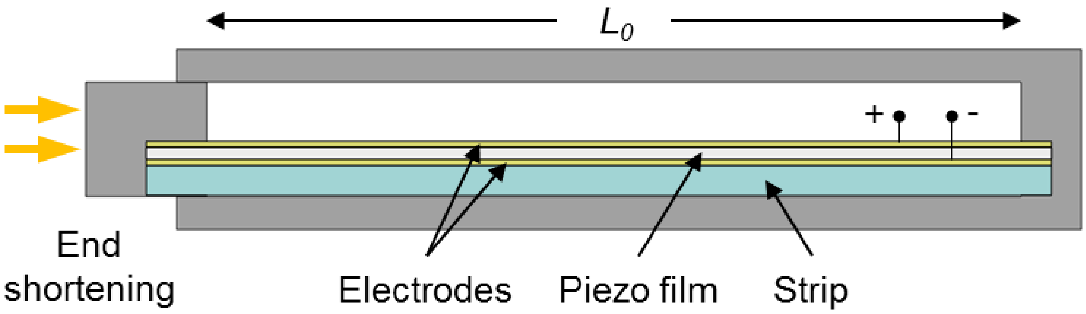

Figure 2-5: Schematic of design I - bilaterally constrained column with a bonded PZT film layer.

### 2.3.2 Design II - Bilaterally constrained non-prismatic column (BCNC) with a cantilever PZT oscillator

In this model, the bilateral constrained prismatic column was modified from a prismatic column to a non-prismatic column with thickness variation to control the buckling location for optimal placement of the cantilever PZT oscillator. Stiffness variation within a column was introduced by changing its thickness, which is the most effective parameter to control bending stiffness along segments of its length. Therefore, column designs with thickness variations in three segments along their length were considered, as shown in Figure 2-6.

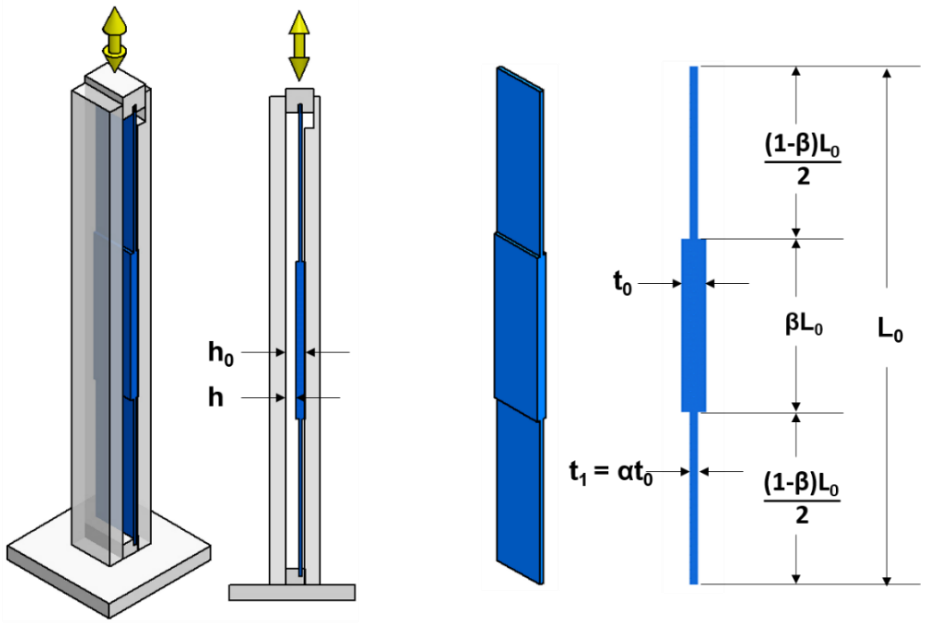

**Bilateral Constraints Setup** **Non-Prismatic Column Design**

Figure 2-6: Schematic of design II - bilaterally constrained non-prismatic column (BCNC) with a cantilever PZT oscillator.

Since the column configuration (i.e., deformed shape, or elastica) between the constraining walls is the one that accommodates the end shortening with the minimum potential energy, the hypothesis behind the non-prismatic column design is that the energetically favorable (lower) configuration is achieved by reducing the bending strain energy from stiff regions by introducing stiffness variations along the column length. The larger bending resistance of stiff segments will allow them to remain straight and develop a line contact with the constraints while flexible regions accommodate the end shortening primarily through bending. Therefore, to achieve a higher number of local instabilities and controlled (or predefined) buckling locations. The larger bending resistance of the thick segment in the middle section of the column makes it more favorable to remain straight and develop a line contact with the constraints while the two end flexible regions accommodate the end shortening primarily through bending, thus creating the condition for the column to behave towards the lower buckling limit case (see Figure 2-7).

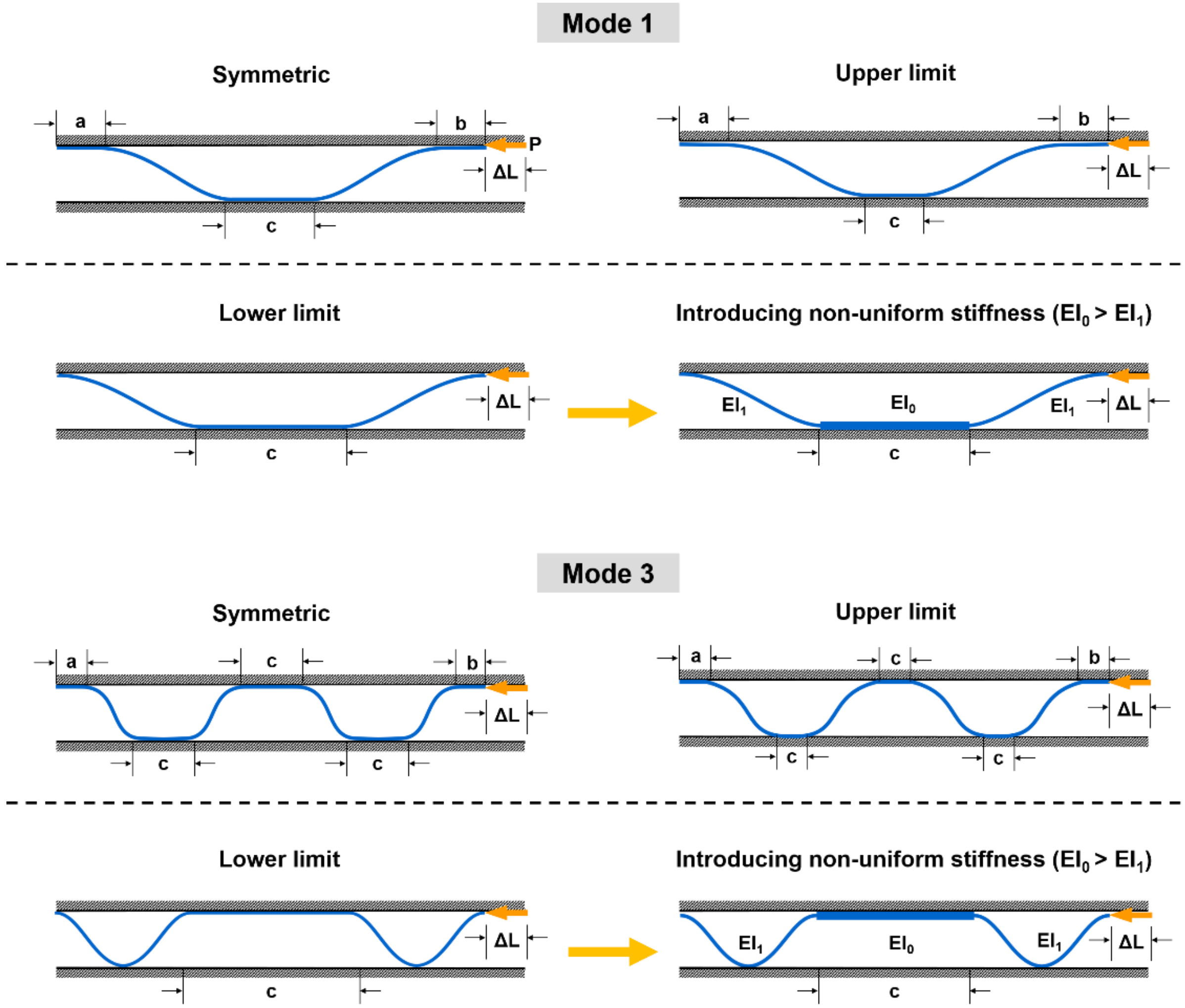

Figure 2-7: The effect of non-uniform stiffness on the buckling shapes.

## 2.4 Prototype fabrication

All the structure prototypes presented in this dissertation were fabricated with a 3D polymer printer (Objet Connex350, Stratasys Ltd., Eden Prairie, MN). A single rigid photo-polymer material (VeroWhite RGD835) was used for the prismatic and non-prismatic columns with material properties and geometry as shown in Table 2-1. The 3D printed column specimens are shown in Figure 2-8.

Table 2-1: Geometry and material properties of the baseline column.

| Property | Value |
|---|---|
| Elastic Modulus, $E$ | 2.5 GPa |
| Column Length, $L_0$ | 190 mm |
| Width, $b$ | 20 mm |
| Thickness of Prismatic Base Column, $t_0$ | 1.78 mm |

For the non-prismatic columns, the middle (thicker) segment thickness, $t_0$ was equal to the uniform thickness in the prismatic column. The ratio between the outer (thinner) segment thickness $t_1$ and the baseline column thickness was defined as $\alpha = t_1/t_0$; and the ratio between the thicker segment length to the column length $L_0$ was defined as $\beta$. The value of $\beta$ was limited as $0.25 \leq \beta \leq 0.65$ to avoid extreme values towards a prismatic column. The dimensionless parameters $\alpha$ and $\beta$ were varied to generate different designs, the parameters are defined in Figure 2-6. The postbuckling behavior of non-prismatic columns with different combinations of $\alpha$ and $\beta$ was experimentally and numerically investigated, and further analyzed by a theoretical model. The results were also compared with those from a prismatic column.

Prismatic column

Non-prismatic column

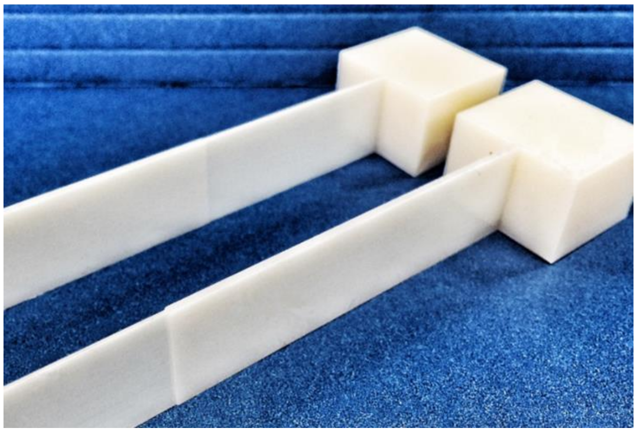

Figure 2-8: 3D printed prismatic and non-prismatic column specimens.

## 2.5 Experimental evaluation

A universal testing machine (Instron 5982) was used to obtain the stress-strain measurements for all the design prototypes with a 50/s data acquisition rate. The maximum loading rate of the machine is 16.9 mm/s. The deformation process of the specimens during the test was video recorded using a SONY Alpha a5000 digital camera.

The rigid constraints in the test setup consisted of aluminum plates (Figure 2-9 (a)). The walls were separated by a gap $h_0$, such that the $h_0/t_0$ ratio was kept constant at 1.7. The strip prototypes were printed integrally with top and bottom loading blocks (see Figure 2-8). The bottom end-block of the strip samples were fully fixed and rotations and transverse translations were constrained on the top end-block. For all cases, the strips were subjected to a full loading and unloading cycle (20 s period) of axial compression under controlled end shortening to a target of 3.8 mm (i.e., 2% global axial strain).

For the prismatic column with piezoelectric film layer design, a piezoelectric film was glued to one side of the strip surface using an epoxy adhesive, and the aluminum plates were glued with an electrical insulating layer on their surfaces. For the non-prismatic columns with cantilever piezoelectric oscillator design, a PVDF piezoelectric oscillator (with substrate) was mounted in a cantilever configuration at the mid-span of both prismatic and non-prismatic columns to compare the harvested energy levels. Considering the mass and beam length of the PVDF film, the bilaterally constrained column setup transforms the input deformation frequency from 0.05 Hz (20 s loading/unloading cycle period) to the harvester's natural frequency of 5.85 Hz. The piezoelectric and the substrate properties are listed in Table 2-2.

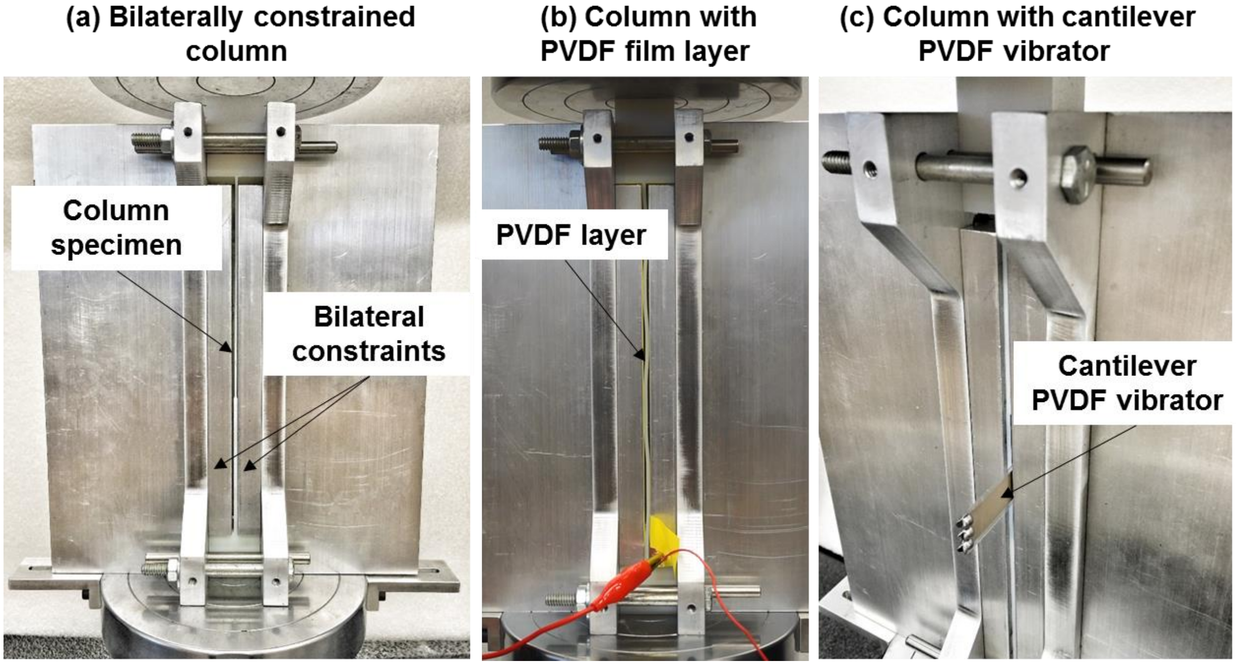

Figure 2-9: Test setup. a) Bilaterally constrained column. b) Prismatic column with PVDF film layer. c) Non-prismatic column with cantilever PVDF oscillator.

Table 2-2: Piezoelectric PVDF film properties.

| PVDF Film | Value |
|---|---|
| Longitudinal Elastic Modulus | 2 GPa |
| Density | 1780 kg/m$^3$ |
| Thickness (with electrodes) | 28 µm / 40 µm |
| Piezo Strain Constant $d_{31}$ | 23 × 10$^{-12}$ C/N |
| Piezo Strain Constant $d_{33}$ | -33 × 10$^{-12}$ C/N |
| Electrical Permittivity | 115 × 10$^{-12}$ F/m |
| Length | 190 mm |
| Width | 20 mm |

Table 2-3: Piezoelectric oscillator properties.

| PVDF oscillator | Value (piezoelectric PVDF/substrate) |
|---|---|
| Young's Modulus | 2 GPa / 2.4 GPa |
| Density | 1780 kg/m$^3$/ 1390 kg/m3 |
| Thickness | 28 µm / 205 µm |
| Width | 12 mm / 16 mm |
| Length | 27 mm |
| Tip Mass | 3.15 g |
| Piezo Strain Constant $d_{31}$ | 23 × 10$^{-12}$ C/N |
| Piezo Strain Constant $d_{33}$ | -33 × 10$^{-12}$ C/N |
| Piezo Stress Constant $g_{31}$ | 216 × 10$^{-3}$ Vm/N |
| Piezo Stress Constant $g_{33}$ | -330 × 10$^{-3}$ Vm/N |
| Electrical Permittivity | 115 × 10-12 F/m |
| Capacitance | 280 pF/cm$^2$ @ 1KHz |

To quantify the power output of the integrated column/piezoelectric device, the voltage as a function of load resistance was assessed. The generated voltage dissipates over time in a close circuit and depends on the load resistance, as shown in Equation 2-15. The outlets from two electrode layers of the piezoelectric film were connected in parallel with the load resistance, and the corresponding load circuit voltage and power were measured for various resistance values. PVDF has a very high output impedance under low frequency loading conditions. Thus, to properly interface it with the device, a JFET-based op-amp (TI LF411), which has a very high input impedance (1 TΩ), was used to minimize the effect of slow loading. The device was connected to the JFET op-amp buffer and the output was probed with an oscilloscope (RIGOL DS1102E, China). Data was collected at 0.1 s intervals. The interface circuit is shown in Figure 2-10.

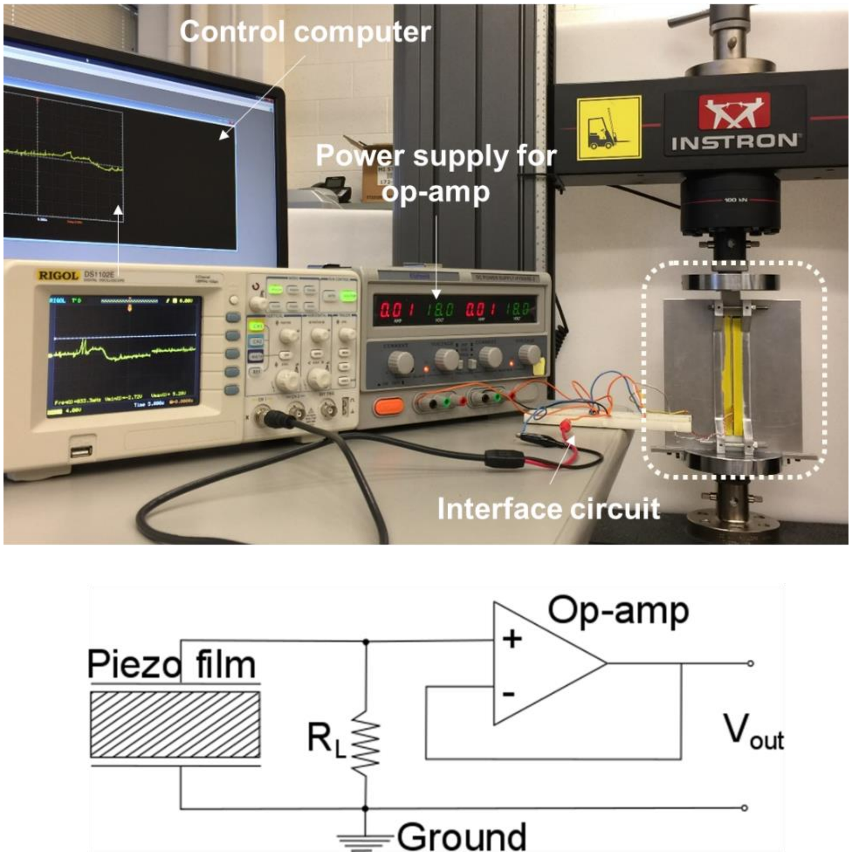

Figure 2-10: Interface circuit and data collection system.

## 2.6 Theoretical analysis

### 2.6.1 Postbuckling response of a BCPC

An analytical model based on the results of Chai [243] and the simplified approach of Xiao and Chen [3] to predict the mode transitions and the buckling shapes of the bilaterally constrained strip with clamped boundary condition under controlled end shortening was adopted, and the model was modified for the placement of the strip adjacent to one side of the constraint. The deformed shapes can be discretized into three parts (see Figure 2-11) [3, 85, 243]: the curved segment with projected length $L_2$, the straight segment $L_1$, and the end shortening $\Delta L$; which yield the column's total length $L_0 = \Sigma L_2 + L_1 + \Delta L$. Figure 2-11 also shows the first three buckling mode configurations for this theoretical model.

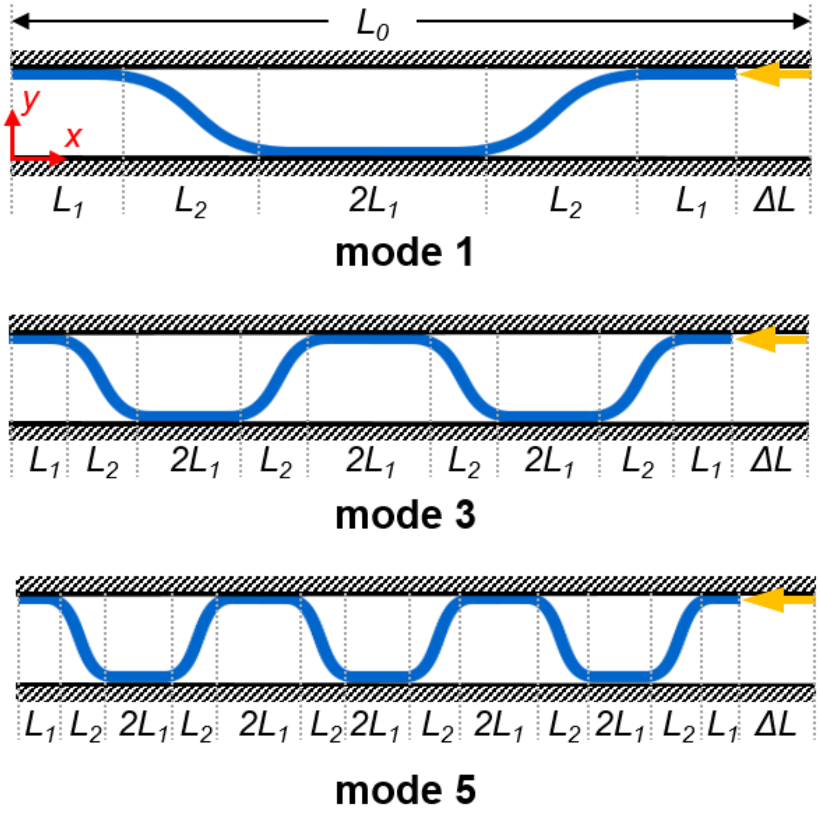

Figure 2-11: Schematic of the theoretical model with the first 3 buckling mode configurations.

The response of an elastic Euler beam under axial compression is defined as

$$y'''' + k^2 y'' = 0, \qquad k^2 \equiv \frac{P}{EI} \qquad \text{Equation 2-1}$$

where $y(x)$ is the transverse displacement of the beam as a function of the axial coordinate $x$, the compression force $P$ and the moment of inertia $I$. Under a symmetry assumption, taking mode 1 as an example, the shape of the curved sections between $x = [L_1, L_1+L_2]$ and $x = [3L_1+L_2, 3L_1+2L_2]$ can be written as in Equation 2-2 and Equation 2-3:

$$y = \frac{h_0}{L_2}(x - L_1) - \frac{h_0}{2\pi}\sin\left(\frac{2\pi}{L_2}(x - L_1)\right) \qquad \text{Equation 2-2}$$

$$y = -\frac{h_0}{L_2}(x - 3L_1 - L_2) + \frac{h_0}{2\pi}\sin\left(\frac{2\pi}{L_2}(x - 3L_1 - L_2)\right) + h \qquad \text{Equation 2-3}$$

where $h_0$ is the gap between the constraining walls. The constraint of coefficient $k$ in Equation 2-1 satisfies $kL_1/2\pi = 1$. The shape of the curved segments in other modes can be represented in a similar manner. Therefore, the length of the curved segments can be calculated as:

$$L_{curved} = \sum \int_L \sqrt{1 + (y')^2}\, dx \qquad \text{Equation 2-4}$$

The total length of the deformed strip is $L_{deformed} = \sum L_{curved} + \sum L_1$. The linear axial strain is

$$\varepsilon_1 = \frac{L_{deformed} - L_0}{L_0} \qquad \text{Equation 2-5}$$

and the axial stress of the strip due to bending and compression is

$$\sigma_1 = E\varepsilon_1 = E\,\frac{L_{deformed} - L_0}{L_0} \qquad \text{Equation 2-6}$$

The potential energy of the strip in this model is considered to consist two parts: compression energy and bending energy. The compression energy is assumed to be uniform per cross-sectional area along the strip and the bending energy is assumed to only exist in the curved segments [3]. Therefore, the compression energy of the strip is

$$E_{compression} = \frac{1}{2} E {\varepsilon_1}^2 A_0 L_{deformed} \qquad \text{Equation 2-7}$$

The curvature of the curved segments is

$$\kappa = \frac{y''}{(1 + y'^2)^{3/2}} \qquad \text{Equation 2-8}$$

The bending energy of the curved segments is

$$E_{bending} = \frac{EI}{2} \int_L \frac{(y'')^2}{(1 + y'^2)^3} dx \qquad \text{Equation 2-9}$$

Therefore, for a given end shortening $\Delta L$, the length of the straight segment length, $L_1$, and the projection of the curved segment, $L_2$, can be determined at the minimum strain energy (i.e., $E_{compression} + E_{bending}$). Thus, the buckling shape configurations can be estimated accordingly. The buckling amplitude increases with $\Delta L$ and the deformed strip makes lateral contact with the constraint that forms straight segments $L_1$. The straight segment keeps growing until the compression strain in the longest straight segment (i.e., the length is $2L_1$ for the symmetric condition) exceeds the critical strain, at which point the strip transitions to a higher mode configuration. The critical strain for the straight segment $2L_1$ is calculated as

$$\varepsilon_{cr} = \frac{\pi^2 I}{(K2L_1)^2 A_0} \qquad \text{Equation 2-10}$$

However, the effective length factor, $K$, is unknown since the boundary conditions of the straight segment $L_1$ are somewhere between pin-pin ($K$ = 1) and fixed-fixed ($K$ = 0.5). The average value of $K$ = 0.75 was adopted in this study.

### 2.6.2 Piezoelectric response of a bounded PZT layer

The piezoelectric layer bonded to the column was modeled as a thin beam based on the Euler-Bernoulli beam theory, the cross section of the strip with a unimorph PVDF film is shown in Figure 2-5(a). Since the thickness of the piezoelectric layer is much smaller compared to that of the strip, only the axial stress component $\sigma_1$ of the strip is considered since all other stress components are negligible. The transverse electric displacement is given by

$$D_3 = d_{31}\sigma_1 + \varepsilon_{33}^{T} E_3 \qquad \text{Equation 2-11}$$

where subscripts *1* and *3* indicate the longitudinal and transverse (poling) directions; *s* is the compliance tensor (m$^2$/N); *d* is the piezo strain tensor (C/N); $\varepsilon^T$ is the permittivity tensor (F/m); *D* is the electric displacement (C/m$^2$); and $E_3$ is the electric field in the transverse direction (N/C). The total electric charge $Q$ is given by the integral of the effective piezoelectric surface area $A_p$ over the electric displacement, expressed by:

$$Q(t) = \int_{A_p} D_3 dA_p = \int_{A_p} (d_{31}\sigma_1 + \varepsilon_{33}^{T} E_3) dA_p \qquad \text{Equation 2-12}$$

The current *i* in a closed-circuit condition is the time derivative of charge Q:

$$i(t) = \frac{dQ(t)}{dt} = \frac{d}{dt}\int_{A_p} (d_{31}\sigma_1 + \varepsilon_{33}^{T} E_3) dA_p \qquad \text{Equation 2-13}$$

Thus, the voltage across a resistance load $R_L$ can be written as

$$V_{R_L}(t) = i(t)R_L = R_L \frac{d}{dt}\int_{A_p} (d_{31}\sigma_1 + \varepsilon_{33}^{T} E_3) dA_p \qquad \text{Equation 2-14}$$

Based on an equivalent current model for the piezoelectric energy harvester, an equivalent capacitance of the piezo-layer $C_p$ is connected in parallel with the resistive load $R_L$. Thus, the voltage across the equivalent capacitance of the piezoelectric patch $C_p$ is equal to the voltage across the resistive load $R_L$. With Maxwell's equation, the transverse electric field and voltage follows the relation $E_3 = -V(t)/h_p$, where $h_p$ is the thickness of the piezo-layer. Thus, Equation (14) can be rewritten as:

$$V_{R_L}(t) = R_L \frac{d}{dt}\int_{A_p}\left(d_{31}\sigma_1 - \frac{\varepsilon_{33}^{T} V(t)}{h_p}\right) dA_p \qquad \text{Equation 2-15}$$

$$\frac{\varepsilon_{33}^{T} A_p}{h_p}\frac{dV_{R_L}(t)}{dt} + \frac{V_{R_L}(t)}{R_L} = \frac{d}{dt}\int_{A_p}(d_{31}\sigma_1)dA_p \qquad \text{Equation 2-16}$$

where $\varepsilon_{33}^{T} A_p / h_p = C_p$. If we replace the above equation with the time constant $\tau = R_L C_p$, then the equation can be expressed as

$$\tau\frac{dV_{R_L}(t)}{dt} + V_{R_L}(t) = R_L\frac{d}{dt}\int_{A_p}(d_{31}\sigma_1)dA_p \qquad \text{Equation 2-17}$$

The electrical power generated is therefore written as

$$P(t) = \frac{1}{T}\int_0^T \frac{V_{R_L}(t)^2}{R_L}dt \qquad \text{Equation 2-18}$$

where $T$ is the total time and $t$ is the time variable. The electrical energy generated by the postbuckling of the strip is

$$U(t) = \frac{1}{2}Q(t)V(t) \qquad \text{Equation 2-19}$$

For an open-circuit condition $E_3$ equal to zero since there is no applied external electric field. Thus, from the relation $Q = C_p V(t)$, the voltage present at the electrodes is

$$V_{OC}(t) = \frac{Q(t)}{C_p} = \frac{h_p}{\varepsilon_{33}^{T} A_p}\int_{A_p}(d_{31}\sigma_1)dA_p \qquad \text{Equation 2-20}$$

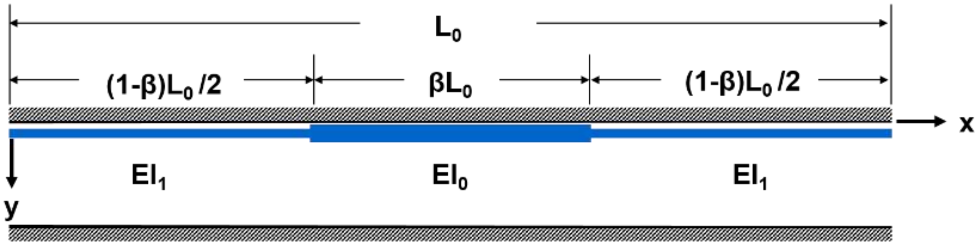

(a) Undeformed Shape

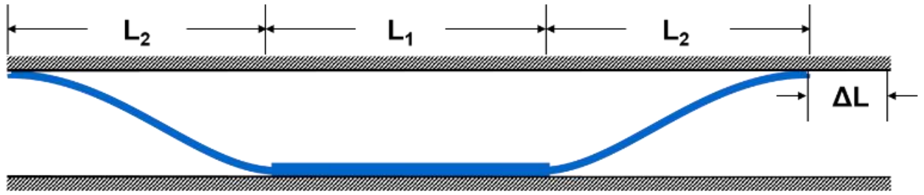

(b) Mode 1

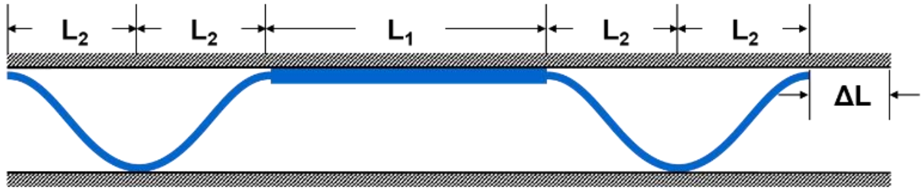

(c) Mode 3

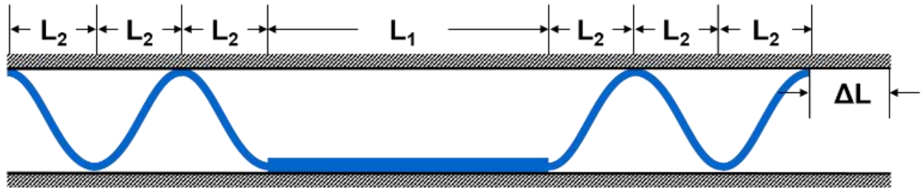

(d) Mode 5

Figure 2-12: Schematic of the theoretical model with the first 3 buckling mode configurations.

### 2.6.3 Postbuckling response of a BCNC

The same modeling concept as presented for the bilaterally constrained prismatic column (BCPC) in Section 2.6.1 was adopted for non-prismatic column, see Equation 2-1 to Equation 2-5, and the only change for this case is the cross-sectional stiffness as a piece-wise variable according to the sectional geometry. Figure 2-12(a) presents the undeformed column with two equal-length outer segments with flexural stiffness $EI_1 = Ebt_1^3/12$ and cross-sectional area $A_1 = bt_1$, and a middle segment with flexural stiffness $EI_0 = Ebt_0^3/12$ and cross-sectional area $A_0 = bt_0$. The other parameters were as described in Section 2.6 and contact friction was neglected. Under the assumption that the column stays at the lower limit configurations (see Figure 2-3), the first three buckling modes are as presented in Figure 2-12(a) to Figure 2-12(d), where the straight section only appears at the middle region of the column.

The potential energy for the column in this model is considered to consist of two parts: compression energy and bending energy. The compression energy is assumed to be uniform over cross-sectional area along the column and the bending energy is assumed to only exist in the curved sections [3]. Therefore, the compression energy of the column is

$$E_{compression} = \frac{E\varepsilon^2}{2}(A_0\beta L_{deformed} + A_1(1-\beta)L_{deformed}) \qquad \text{Equation 2-21}$$

The bending energy of the curved sections when $L_{curved} \leq (1-\beta)\, L_{deformed}$ is

$$E_{bending} = \frac{EI_1}{2}\int_L \frac{(y'')^2}{(1+y'^2)^3}dx \qquad \text{Equation 2-22}$$

and when $L_{curved} > (1-\beta)\, L_{deformed}$ is

$$E_{bending} = \frac{E}{2}\left[\left(\frac{L_{curved}}{L_{deformed}} - 1 + \beta\right)I_0 + (\beta - \frac{L_{curved}}{L_{deformed}})I_1\right]\int_L \frac{(y'')^2}{(1+y'^2)^3}dx \qquad \text{Equation 2-23}$$

Therefore, for a given end shortening $\Delta L$, either the length of the straight section length $L_1$ or the length of the curved section $L_2$ can be determined at the minimum potential energy (i.e., $E_{compression} + E_{bending}$). Thus, the buckling shape configurations can be estimated accordingly. Similarly, the critical strain of the straight section $L_1$ is calculated as

$$\varepsilon_{cr} = \frac{\pi^2 E}{\left(\frac{KL_1}{r}\right)^2}, \qquad r = \frac{1}{A_0^2} \qquad \text{Equation 2-24}$$

## 2.7 Numerical simulation

Numerical simulations were conducted using the finite element (FE) program ABAQUS (Simulia 2014). The column was modeled with 4-node quadrilateral finite-membrane-strain elements (S4). The analysis procedure followed two general steps: a linear eigenvalue analysis of the ideal column and a second-order elastic dynamic analysis of the column with artificial imperfections. In the linear analysis, the critical buckling loads and the corresponding mode shapes are found. The dynamic analysis was conducted using the implicit solver in ABAQUS with consideration of large deformations. An artificial imperfection based on the superposition of buckling mode shapes was added to the column's original geometry to trigger the second-order effects, the first three bucking mode shapes are shown in Figure 2-13. The seeded imperfection had contributions from four mode shapes with gradually decreasing amplitude with respect to the column's thickness: 1st (3%), 3rd (0.23%), 5th (0.08%) and 7th (0.016%). Consistent with the experimental setup (Section 2.5) the column/strip in the model was placed so that it was adjacent to one of the constraining walls. Since shell elements have no physical thickness, the distance between the rigid walls and the strip was the net gap $h = h_0 - t_0$. An offset of 5% of the net gap was provided on the near wall side to accommodate seeding of the initial imperfections for the nonlinear analysis and to avoid interaction with the no penetration rigid wall boundary and the strip. The constraints were modeled with rigid shell elements with no-penetration contact behavior. The friction coefficient between the wall and the column surfaces was 0.2, chosen by calibration of the simulation results with test data.

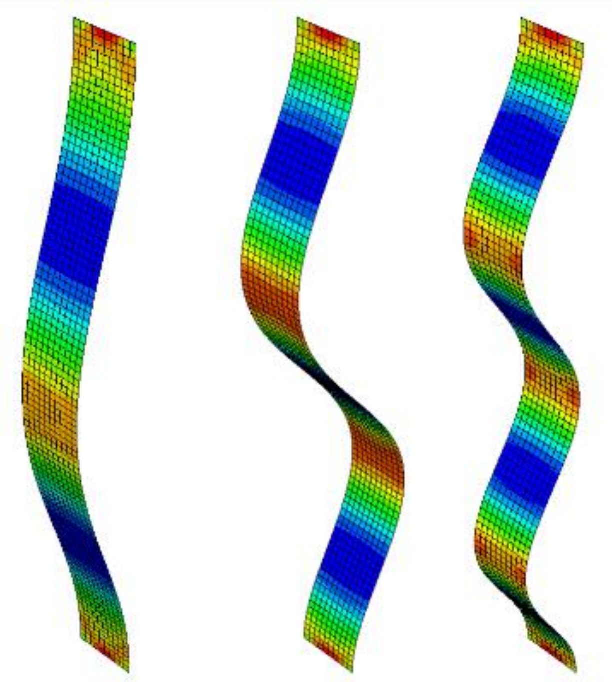

Figure 2-13: First three buckling mode shapes of the prismatic column.

For model I - bilaterally constrained prismatic column (BCPC) with a bonded PZT film layer, an additional piezoelectric film was also modeled using linear piezoelectric brick elements (C3D8E). The contacted side of the piezoelectric film surface was tie-constrained with the strip, thus enforcing equal deformations, and a ground electric potential boundary condition was assigned on the same surface of the piezo-layer to allow an electric potential difference to be generated. A reference point tied all the nodal electric potential degrees of freedom on the top free surface of the piezo-layer to add up the generated voltage.

# Chapter 3

# SHEAR ENERGY DISSIPATION – CONCEPT AND METHODS

## 3.1 Background

A single inclined elastic beam element under end shear deformation exhibits a negative stiffness region but follows the same load-deformation path upon unloading with no energy dissipation (Figure 3-1a). The proposed structures (see Figure 3-1b) consist of an array of $m \times n$ beam units, with $m$ units that are equally spaced in a vertical stack (rows) and rigidly connected to end-constraining segments, and $n$ repeating columns of the multi-row beam assemblies. Under in-plane shear motion, the beam units within a column respond simultaneously with the critical force being simply the summation of the individual critical forces of the $m$ elements in the column. Given the unavoidable geometric imperfections in the system, the $n$ coupled columns in series connection respond in sequential snap-through transitions, with the force-displacement response displaying $n$ 'jumps' and $n$ unstable paths, and the total deformation is equal to the summation of the displacements from the $n$ columns. Since the 'jumps' are due to unstable transitions of the beams within a column, the unit elements are able to experience unbounded motions between the two stable equilibrium states until the motion decays due to friction. Energy dissipation consequently occurs by the release of mechanical energy, through the unstable snap-through motions, and its conversion to kinetic energy and in turn into heat. This phenomenon has been termed 'twinkling' and can be modeled by a spring-mass chain with non-monotonic stiffness elements that permit oscillatory behavior of the inner masses [260-262].

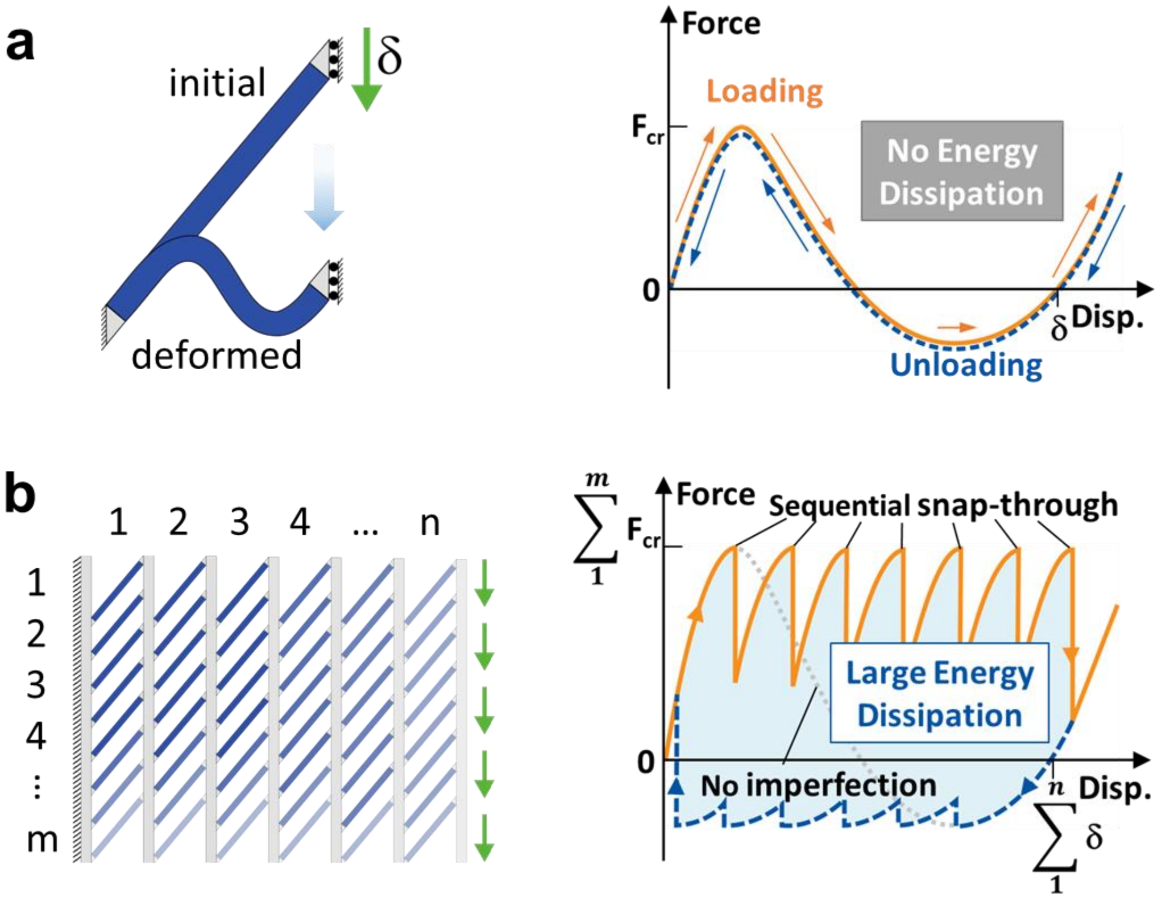

Figure 3-1: Schematic of snapping element(s) and their force-displacement response. a) A single unit elastic snapping beam element in its initial and deformed configuration (left), and its response curve under applied displacement with a negative stiffness region but no energy dissipation (right). b) An array of $m \times n$ connected units (left) and its sequential snap-through response curve under an applied displacement with energy dissipation (right), where the gray dotted line shows the response of the system when there is no imperfection.

## 3.2 Model designs

The design concept is illustrated in Figure 3-1b.Elastic inclined beams were chosen as the unit elements, which can experience limit-point snap-through instability under vertical displacement. The limit point is an inflection of the primary equilibrium path that causes a stiffness change from stable to unstable. This transition corresponds to a negative stiffness region, which leads to a rapid unstable motion that triggers a release of the system’s stored strain energy and is reflected in the energy-deformation curve as a loss of convexity. The unstable transition stops when the system reaches its next closest stable equilibrium path, and the rate of the motion is independent from the external deformation/load rate if it is not constrained by the system's boundary conditions.

The material structures (Figure 3-2) consist of elastic beam unit segments and rigid (much higher material stiffness) end-constraining segments. The rigid end-constraining segments feature a linear sliding mechanism at their ends (top and bottom) to allow relative vertical movement between adjacent columns but prevent lateral motion of the beam elements within a column. The effects of the two dominant parameters, initial angle $\theta$ and slenderness $t/L$, on the mechanical response of single inclined beams has been numerically investigated [27] with the aim of characterizing their energy trapping or energy restoring features. Based on the noted study, two beam geometries ($\theta = 25°$, $t/L = 0.17$ and $\theta = 40°$, $t/L = 0.18$) were used as the unit elements for all the test prototypes considered in this study; with all beam elements having constant 20 mm depth ($d$) and 7 mm length ($L$). For the proposed energy-dissipating material system, consisting of multiple-unit structures, all beams in the array had the same geometry and each column of beam elements deforms in a predefined direction.

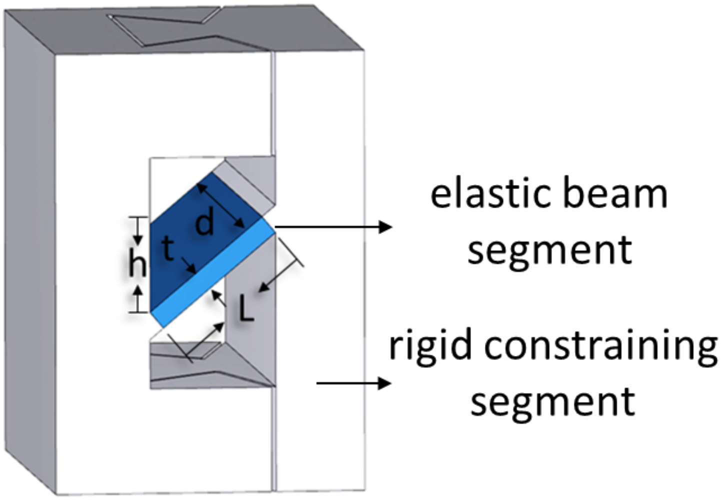

Figure 3-2: Schematic the proposed material model for a unit element with geometric illustrations.

Two multiple-unit design layouts, differing in the arrangement of the columns' beam orientation, were designed to operate under half-cycle (i.e., only positive loading-unloading) and full-cycle (i.e., positive and negative loading-unloading) cyclic in-plane shear demands. For the half-cycle conditions, the loading cycles were applied in the positive direction, imposing a stress-strain response that occurred in the positive domain only. For the full-cycle conditions the loading cycles were applied in both positive and negative directions, resulting in a full stress-strain response. Both loading conditions are illustrated in Figure 3-3.

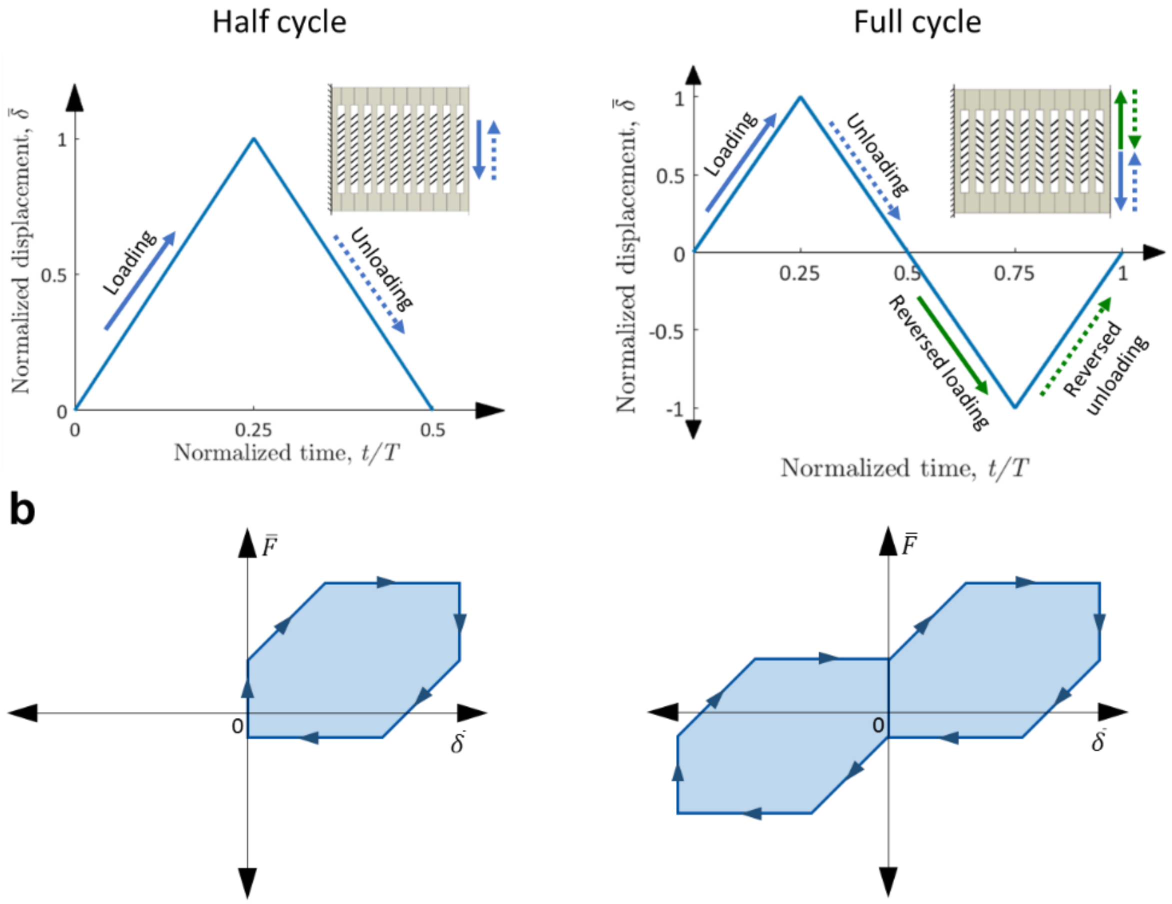

Figure 3-3: a) Strain-controlled loading cycle: half cycle (left) and full cycle (right) conditions. Time is normalized by the time period T for one complete cycle of loading. b) Schematics of the stress-strain response under half cycle (left) and full cycle (right) loading conditions.

## 3.3 Prototype fabrication

Structure prototypes were fabricated using a 3D polymer printer (Objet350 Connex3, Stratasys Ltd., Eden Prairie, MN) that allows monolithic multi-material printing by jetting microscopic layers of liquid photopolymer and instantly curing them with UV light. A soft rubber-like polymer (TangoBlackPlus) was used for the elastic beam segment and a stiff polymer (VeroWhite) was used for the rigid end-constraining segments. The initial and deformed configuration of a 3D printed unit under vertical displacement (shear deformation) are shown in Figure 3-4.

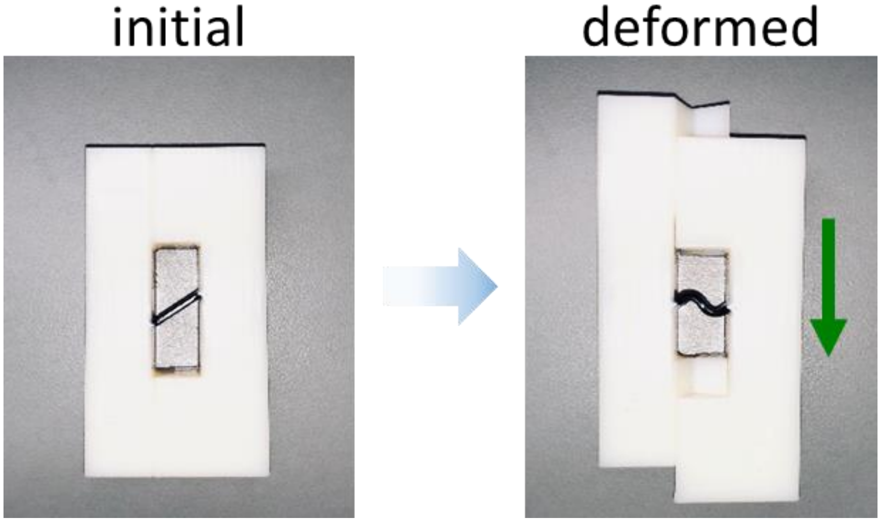

Figure 3-4: Initial and deformed configuration of a 3D printed unit beam.

Two single-beam unit elements with the geometries ($\theta = 25°$, $t/L = 0.17$ and $\theta = 40°$, $t/L = 0.18$) were 3D printed and tested to verify their snap-through behavior. The three 3D printed material multi-unit prototypes for the half- and full-cycle design layouts are shown in Figure 3-5a and Figure 3-5b, respectively.

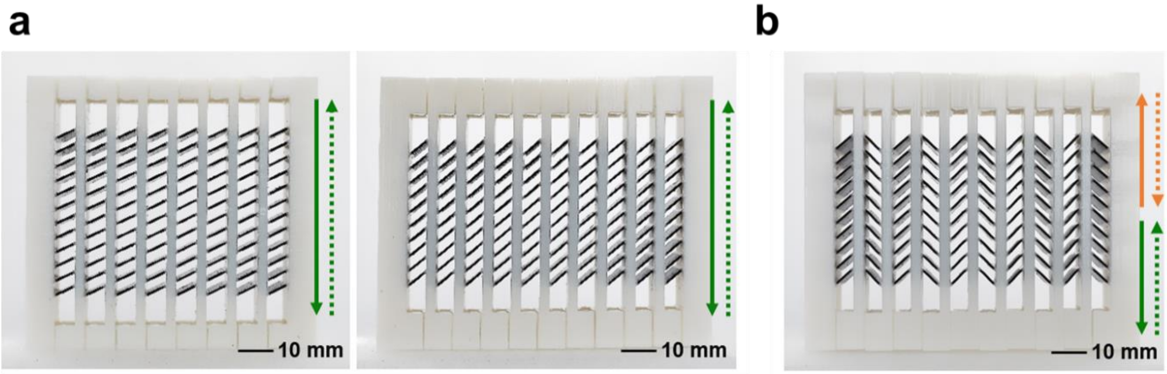

Figure 3-5: 3D printed material prototypes for a) half-cycle loading condition (left: θ = 25°, t/L = 0.17, m, n = 12, 8; right: θ = 40°, t/L = 0.18, m, n = 10, 10), and b) full-cycle loading condition (θ = 40°, t/L = 0.18, m, n = 10, 5×2). Solid and dashed line indicates loading and unloading direction respectively.

## 3.4 Experimental evaluation

A universal testing machine (Instron 5982) was used for the stress-strain measurements for all the design prototypes with a 50/s data acquisition rate. The maximum loading rate of the machine is 16.9 mm/s. The deformation process of the specimens during the test was video recorded using a SONY Alpha a5000 digital camera.

The loading frames were made of aluminum plates. The vertical flags of the two 'T' shape loading frames were bolt-tied with the specimens' vertical edges, and the lateral flags of the frames were bolt-tied with the top and bottom loading plates. The top end of the loading plate was fixed all the time during the test, and the shear deformation was applied to the specimens by the vertical movement of the bottom loading plate under strain control. The test setup is shown in Figure 3-6. The vertical displacement was applied until all columns aligned with the loading direction fully snapped to their deformed states, which varied with the geometry of the specimens. All the specimens were tested at three different loading rates: 5 mm/s, 10 mm/s and 15 mm/s, to verify the rate dependency of the responses.

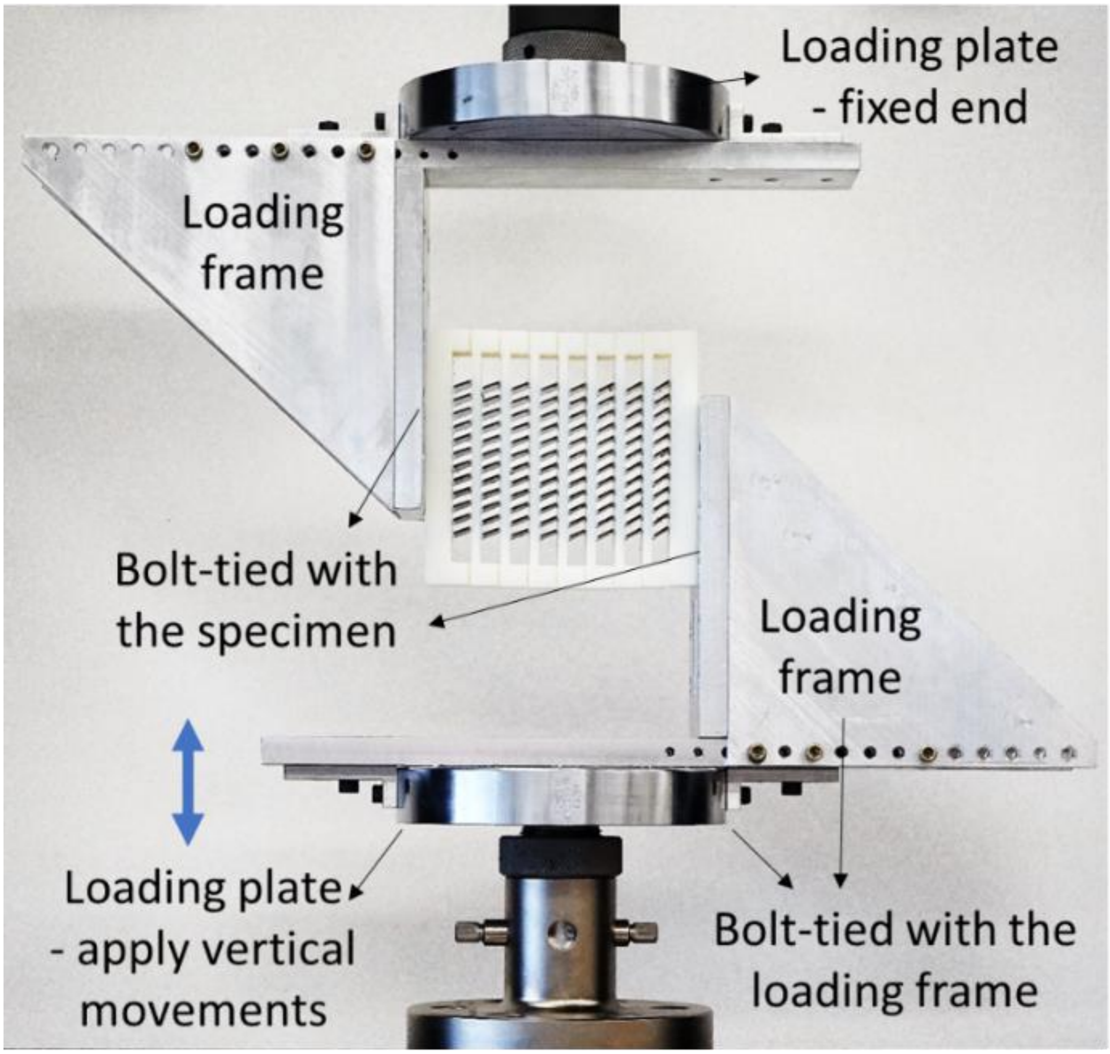

Figure 3-6: Test setup for architected materials.

## 3.5 Analog model

A simple analog model is used here to qualitatively capture the behavior of a system of snapping inclined beams. Instead of solving the large deformation problem, the analog model uses a linear spring $k_b$ to represent the bending stiffness of the beam and the beam only deforms axially with a stiffness $k_a$, as shown in Figure 3-7. Since lateral opening was observed during preliminary tests, resistance to the lateral expansion is introduced by the linear spring $k_L$. The height $h$ and the span $L$ define the beam's original geometry at its stress-free equilibrium state. The structure is deformed under displacement control by $\delta$ with the deformed angle $\theta$ and the reaction force $F$. This model has been analytically and experimentally studied in many works [14, 107, 207, 263, 264]. The potential energy of the beams in one column is given by:

$$U_i = \frac{m}{2}\left(k_a \Delta L^2 + {v_i}^2 k_L + k_b {\delta_i}^2\right),\ i = 1,2,\dots,n. \qquad \text{Equation 3-1}$$

$$\text{with } \Delta L = \sqrt{(L-v)^2 + (h-\delta)^2} - \sqrt{L^2 + h^2} \qquad \text{Equation 3-2}$$

Thus the reaction force of the system can be solved by the following coupled equilibrium equations:

$$\begin{pmatrix} \frac{\partial U_i}{\partial \delta_i} \\ \frac{\partial U_i}{\partial v_i} \end{pmatrix} = \begin{pmatrix} F_i \\ 0 \end{pmatrix} \qquad \text{Equation 3-3}$$

For the system response of multi-unit structures (Figure 3-5b), the unit beams are rigidly connected in parallel in a column that moves simultaneously, and the coupled behavior between columns in series connection was obtained by minimizing the total energy of the system for a given displacement (*Δ<sub>max</sub>*). The problem is formulated as:

$$\begin{gathered} min\ U_{total}(\delta_1, \delta_2,\ \dots, \delta_{n-1}, \delta_n) = \sum_{i=1}^{n} U_i \\ with\ respect\ to \quad \delta_1, \delta_2,\ \dots, \delta_{n-1} \\ where \quad \delta_n = \mathit{\Delta}_{max} - \sum_{i}^{n-1} \delta_i \end{gathered} \qquad \text{Equation 3-4}$$

Imperfection is introduced randomly to the beams in each column by varying the nominal Young's modulus by ± 0.01% to trigger the sequential snap-through transitions. This optimization problem was solved using Mathematica with the local minimization function *FindMinimum*, along with the constraints $\frac{\partial U}{\partial v} = 0$ and $\delta_n = \Delta_{max} - \sum_i^{n-1} \delta_i$. Since the total energy function contains multiple local minimums, the initial search point for each iteration as the total displacement proceeded was the result from the previous search step.

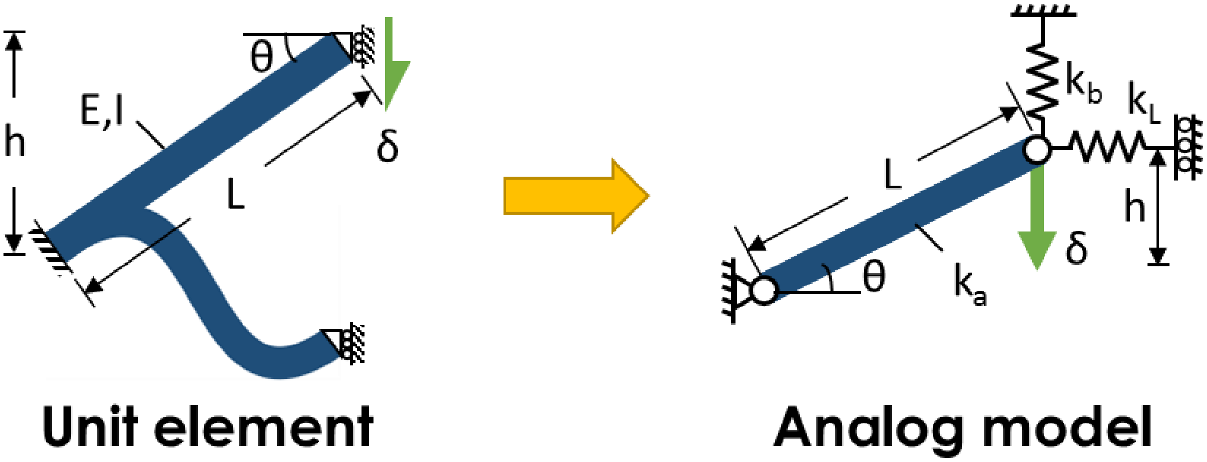

Figure 3-7: Analog model for theoretical analysis.

## 3.6 Numerical simulation*

(* The numerical model and analysis presented in this section was conducted by Ali Imani Azad.)

Finite element (FE) analyses were conducted using the program ABAQUS to explore the effect of beam unit geometry on the performance of the proposed material systems. Dynamic analyses were conducted using the program's implicit solver with consideration of large deformations under quasi-static conditions. The 2D continuum-type element CPE4 was used assuming plane strain conditions, and artificial imperfection was introduced to the system through mesh variation at one randomly selected beam unit in each column. For the single unit system, only the elastic beam element was modelled and each beam was deformed by applying a vertical displacement to one of the ends and fixing all motions of the other end. Out-of-plane movements were constrained. For the multiple-unit system, both the elastic beams and rigid constraining segments were modelled and their adjoining surfaces were constrained to each other (tie). A friction coefficient was assigned to the contacting surfaces to model the linear sliding mechanisms at the ends of the constraining columns. The response of the rubber-like polymer was simulated using a visco-hyper-elastic model (see Figure 3-8); and an elastic modulus of 2300 MPa and Poisson's ratio of 0.3 were used for the stiff polymer material.

The properties and rate-dependent viscoelastic effect on the behavior of the TangoBlackPlus material were determined through tensile tests based on the ASTM D638-14 standard at loading rates of 50 mm/min and 500 mm/min. The tensile stress-strain responses of 6 test specimens and the visco-hyper-elastic material model used in the numerical analysis are compared in Figure 3-8.

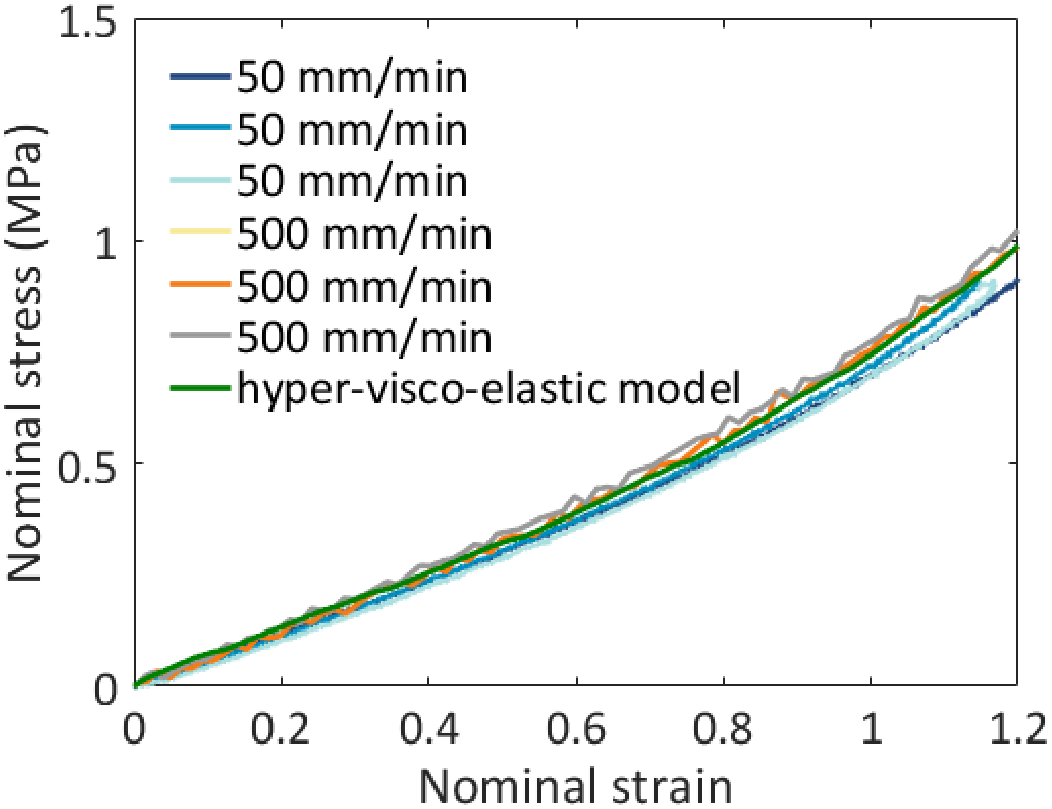

Figure 3-8: Nominal stress-strain curves of the TangoBlack material under tensile test.

Based on the observed behavior (in Figure 3-8) and modeling suggestions from [265], the material used in the numerical simulations was modelled as visco-hyper-elastic. Yeoh's model was used for the hyper-elastic behavior, with the strain energy as a function of the principle stretches as:

$$W = \sum_{i=1}^{n} C_i \, (I_1 - 3)^3, I_1 = \lambda_1 + \lambda_2 + \lambda_3 \qquad \text{Equation 3-5}$$

The material coefficients were determined through a calibration process with the experimental data as $C_1 = 0.1244$, and $C_2 = 0.005069$. The viscous behavior was modelled using Prony series as:

$$D(t) = 1 - \sum_{i=1}^{n} \gamma_i \qquad \text{Equation 3-6}$$

where $\tau_1 = 0.1, \gamma_i = 0.002;\ \tau_2 = 1, \gamma_2 = 0.2631; and\ \tau_3 = 100, \gamma_3 = 0.1529.$

# Chapter 4

# ENERGY HARVESTING DEVICES – RESULTS

Results from the experimental evaluations, theoretical analyses, and numerical simulations of the energy harvesting concept proposed in Chapter 2 for two structural models, bilaterally constrained prismatic column (BCPC) with a bonded PZT film layer and bilaterally constrained non-prismatic column (BCNC) with a PZT cantilever oscillator, are presented in this chapter. The results from the numerical and theoretical models are first validated with the experimental results, and then the models are further used to predict the postbuckling behavior of the considered structures. The experimental energy generations are compared and evaluated with other existing strategies, and results from parametric studies are presented at the end of this chapter to explore the design space of the proposed systems.

## 4.1 Model I - BCPC with a bonded PZT film layer

### 4.1.1 Model validation

The developed theoretical and numerical models were validated by comparing their response predictions with experiments. The mechanical response of the strip obtained from the theoretical model, the numerical simulation, and the experiment are compared in Figure 4-1, for a load cycle to 3.8 mm end shortening in 20 s (full loading-unloading cycle). It can be seen that the theoretical model and FE simulations adequately captured the number of buckling mode transitions, and the initial and end response stiffness. The mode jump triggering time is very sensitive and difficult to predict exactly, as eccentricities on the placement of the strip and loading plate, actual imperfections, and friction resistance between and strip and walls, will affect the onset of mode jumping. Therefore, differences between the results due to these modeling uncertainties are difficult to avoid. Nonetheless, the theoretical and numerical models are considered acceptable for the purposes of this study.

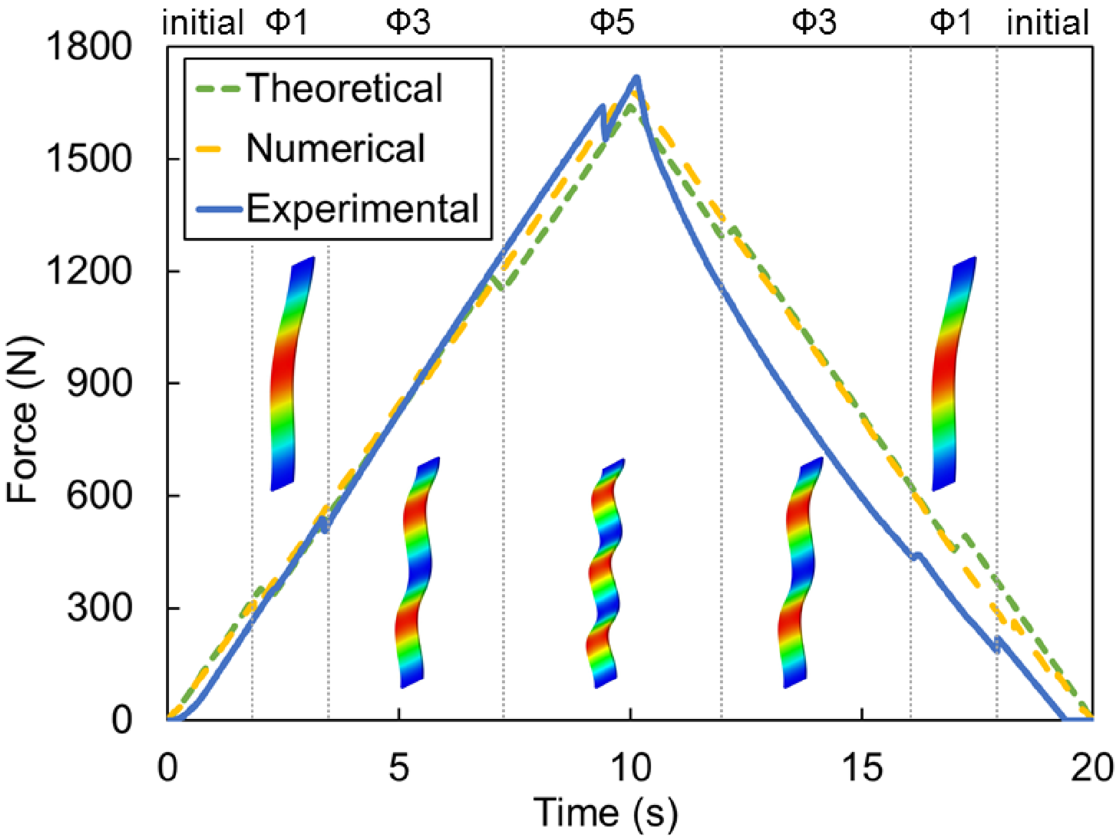

Figure 4-1: Mechanical response of the bilaterally constrained strip under 3.8 mm end shortening.

### 4.1.2 Mechanical response

The postbuckling transition process of the bilaterally constrained strip, in terms of the buckling shape configuration and the axial force, can be obtained from the theoretical model. The development of the curved segment length $L_2$ and the axial force of the strip versus the strip end shortening are shown in Figure 4-2. It can be seen that during the initial loading stage the strip is at its pre-buckled initial configuration, which is straight with no curved segment lengths. Two curved segments develop when the first buckling mode jump is triggered. The length of the curved segments decreases as the end shortening increases since more flat segments ($L_1$) develop as the strip contact with the constraint's surface grows. Once the flat segment increases to the critical length (i.e., the axial stress of an individual flat segment is higher than the overall axial stress of the strip), its buckling is triggered and the strip keeps deforming in a similar manner in the next buckling mode configuration until the next critical buckling limit is reached. The buckling configurations at the beginning and end of each buckling mode are shown in Figure 4-3, which also show the growth of the flat segments and the decrease of the curved segments (for each mode shape) as loading proceeds.

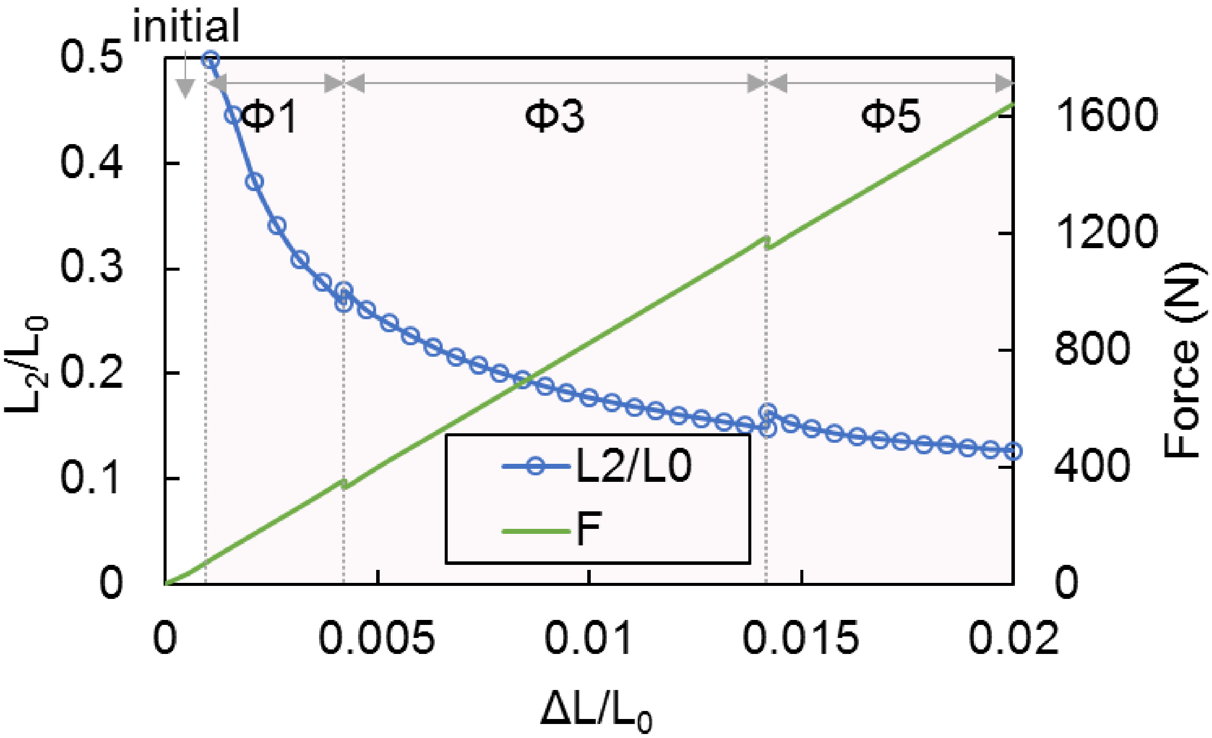

Figure 4-2: Postbuckling transition process as obtained from theoretical analysis for the development of curved segments and axial force on the strip versus the strip end shortening (normalized by the initial strip length).

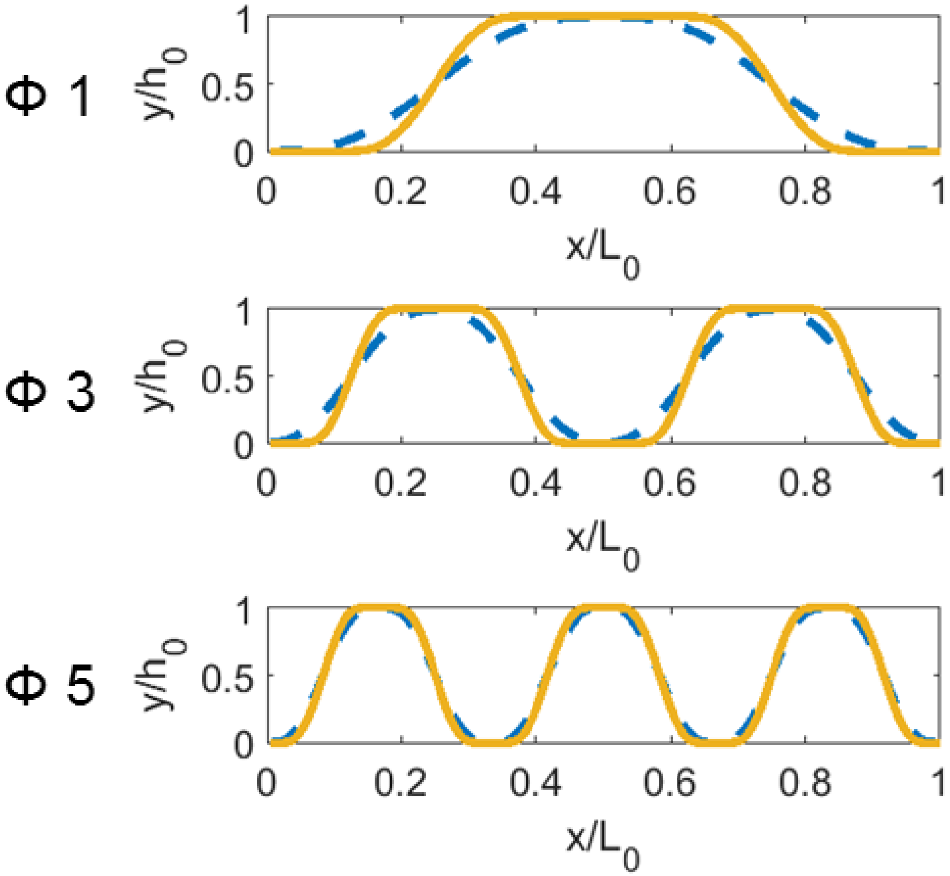

Figure 4-3: Profiles of buckled strip obtained from theoretical analysis at the beginning and the end of each buckling mode (height and length are normalized by the initial gap distance and strip length).

### 4.1.3 Piezoelectric response

The open-circuit voltage of the device obtained from the theoretical model (Equation 2-20) and the numerical simulation are shown in Figure 4-4. It can be seen that the models are in good agreement, predicting a peak voltage around 208V at a 3.8mm end shortening. It can also be observed that the voltage curve has the same shape as the load-history response curve (Figure 4-1). If the load resistance value is very high in a circuit, the resulting voltage is close to the theoretical open circuit voltage output. However, since the peak open-circuit voltage is much higher than the maximum voltage of the op-amp (~18V), only the load-circuit voltage output was verified experimentally.

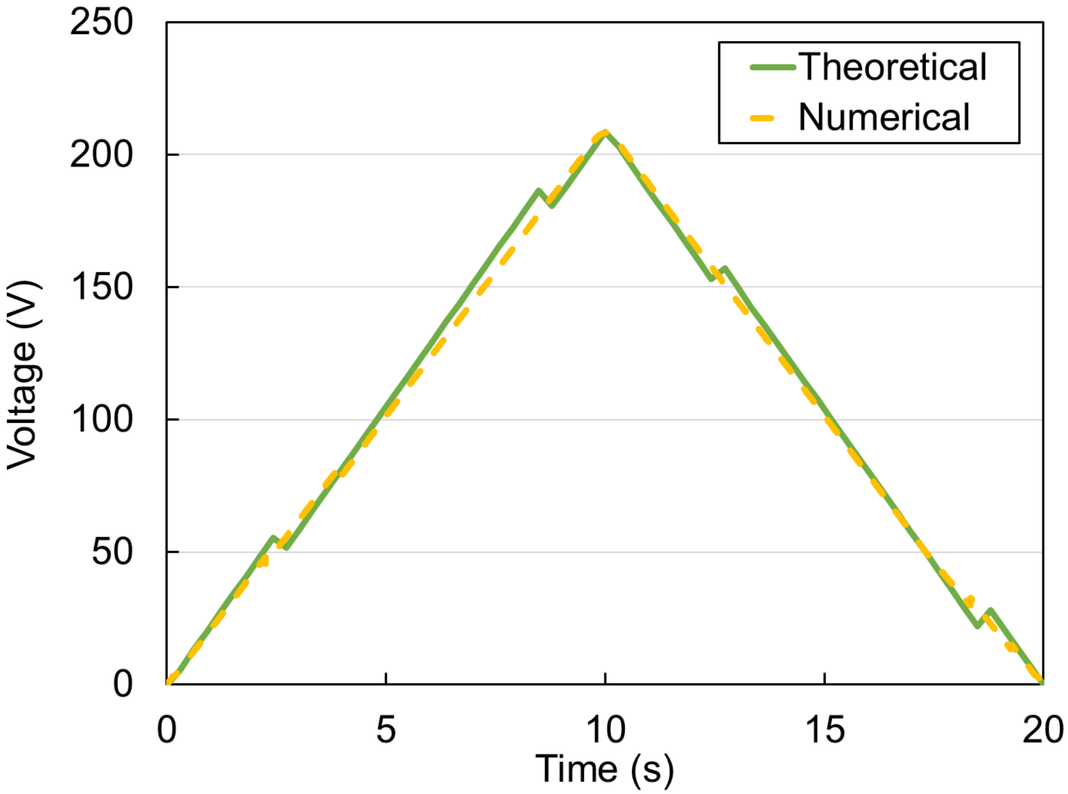

Figure 4-4: Open-circuit voltage of the energy harvesting device under 3.8mm end shortening in a 20s loading-unloading cycle.

The device was interfaced with a circuit containing a variable resistor and an op-amp, as shown in Figure 2-10. Two load resistance cases, 100 MΩ and 125 MΩ, are presented in Figure 4-5 to compare with the theoretical and numerical results. The frequency response needs to be considered for the analytical and numerical analyses since the device operates under a distribution of transient signals over a band of frequencies. The capacitance of the piezoelectric film and the resistive load in the interface circuit together form a divider network with a simple RC high-pass filter characteristic, which only passes a signal when the frequency of the input is higher than the "cut-off" frequency (i.e., 0.707 of the magnitude of the input quantity). Therefore, the raw time-domain voltage signal was filtered (using a fast Fourier transform (FFT) algorithm) to obtain the resulting output signal spectrum and the corresponding time-domain voltage output (by using inverse FFT), which gives an asymptotic curve of the output voltage in the corresponding time-domain.

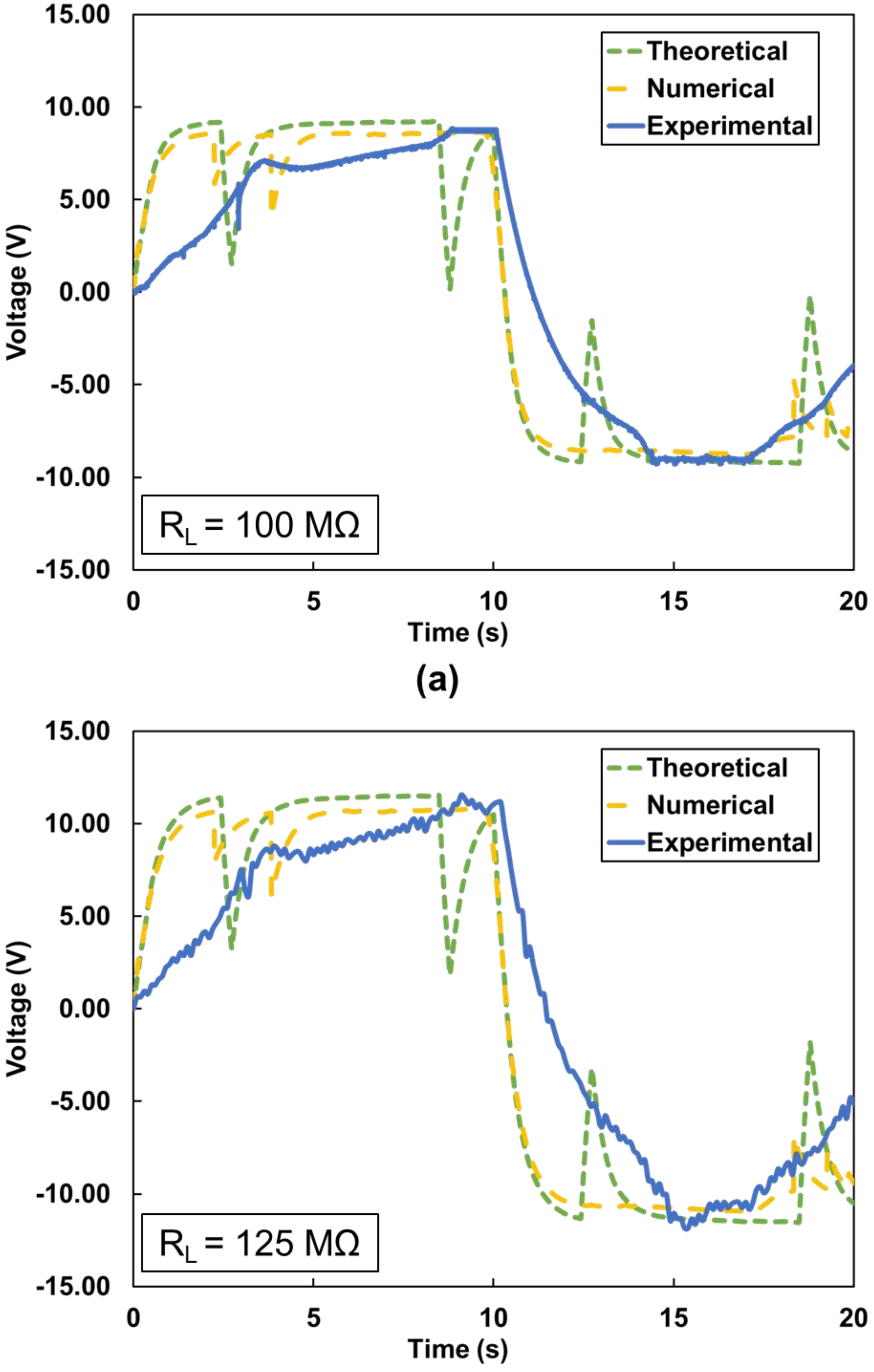

(a)

(b)

Figure 4-5: Load circuit voltage generated by the device for: (a) over 100 MΩ load resistance, and (b) over 125 MΩ load resistance.

The power-load curve shows the power generated at various load values, which represents the theoretical maximum power that can be generated by the device when it is impedance-matched with the resistance load for a given end shortening. Piezoelectric materials have a very high internal impedance. Under quasi-static deformations, loading effects are substantial when the circuit load is small, and the corresponding voltage and power output are low. When the circuit resistance load matches the piezo resistance value the generated power is maximum. As the load resistance increases beyond the piezo impedance the voltage remains almost constant and close to the open circuit voltage value, but the power will drop since the current will keep diminishing. To obtain the curve, only the voltage and load resistance are needed since the power can be calculated from both variables. The circuit used to obtain the load-voltage and the power-load curves is shown in Figure 2-10. The voltage output data collected from the oscilloscope was processed using MATLAB to be integrated using Equation 18, and the resulting power-load curve is shown in Figure 4-6 for the prototyped piezo-strip (properties are shown in Table 2-2) under three different deformation cycles with the same 3.8 mm end shortening. The power is given in $\mu$W per cm$^2$ of the PVDF surface area, and it is plotted versus the load resistance values in log scale. It can be seen that a peak power of 1.33 $\mu$W/cm$^2$ is obtained and remains unchanged with varying loading time. However, the duration (time) of the deformation cycle affects the dominant response frequency, which implies that the resistance load increases with the deformation cycle period. As seen in Figure 4-6 resistance loads of 1 GΩ, 2 GΩ, 3 GΩ matched piezoelectric resistance values for 20 s, 40 s and 60 s deformation cycles.

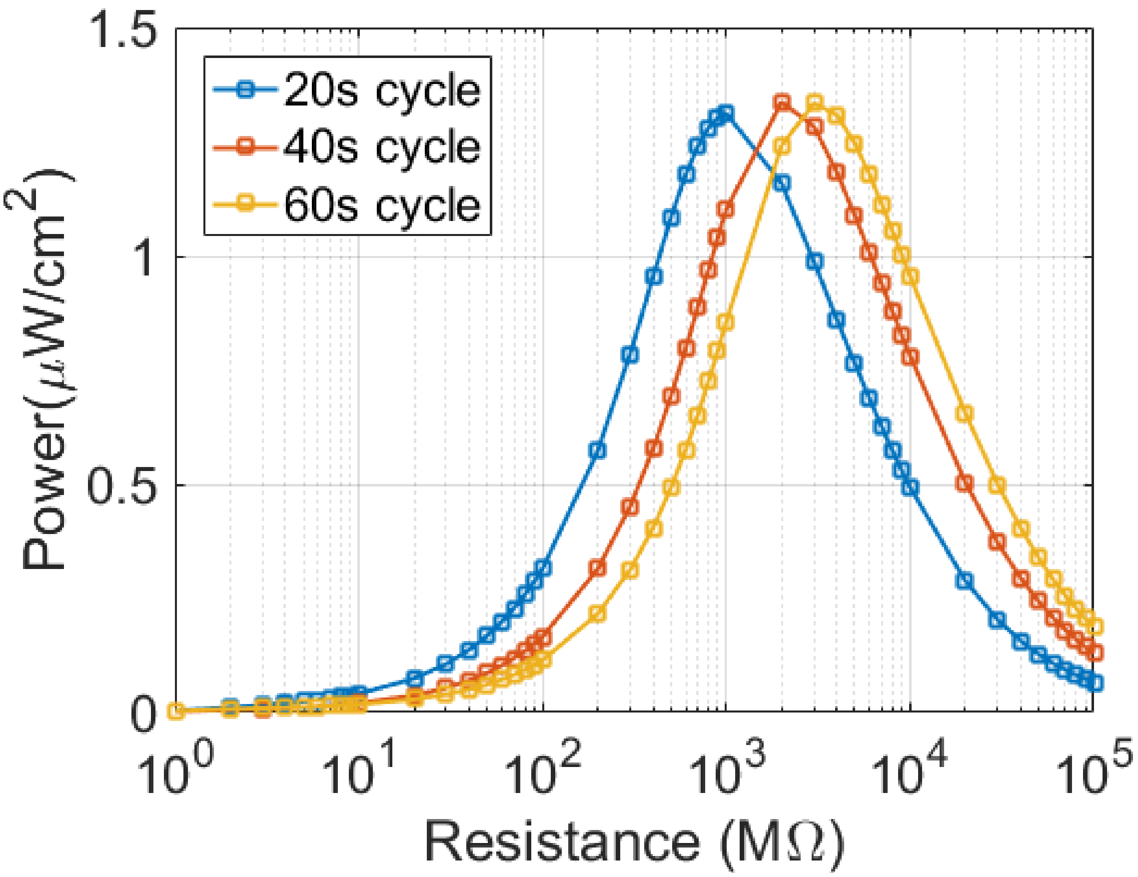

Figure 4-6: Power-load curves of the energy harvesting device under 3.8 mm end shortening for different duration deformation cycles. The power is given in µW per cm2 of the PVDF surface area.

A comparison between the proposed systems from this research with two other investigated strategies on harvesting energy from quasi-static loading conditions is shown in Table 4-1. Since the device dimensions for each system are different, the maximum power output is normalized by the piezoelectric surface area for a better comparison. It can be seen that the proposed system's performance is higher compared to the existing strategies. This demonstrates that the device concept developed through this research can adequately and efficiently provide power to devices with low-power budgets.

Table 4-1: Comparison between our system to other investigated strategies on harvesting energy from quasi-static loading conditions.

| Investigated strategies on harvesting energy from quasi-static loading conditions | Approaches | | | Max. Power Output (μW/cm$^2$) |
|---|---|---|---|---|
| | Analytical | Experimental | Numerical | |
| Sohn, Choi et al. [226] | √ | √ | | 0.0025-0.37 |
| Nanda and Karami [228] | √ | | √ | 0.58 |
| Our system | √ | √ | √ | 1.33 |

### 4.1.4 Parametric study

A parametric study was conducted using the FE model presented in Section 2.7 to determine the correlation between power generation and the device's dimensions. Prior studies on the postbuckling behavior of the bilaterally constrained strip, the strip thickness and gap distance were identified as the key parameters controlling the postbuckling response [192]. Therefore, Figure 4-7 shows how the peak power varies with changing strip thickness (specifically, 1.3 mm, 1.1 mm, 0.9 mm, 0.7 mm, 0.5 mm) and gap distance (specifically, 1.8 mm, 1.6 mm, 1.4 mm, 1.2 mm, and 1 mm) for 25 different case scenarios. Figure 4-7(a) plots the peak power generated in $\mu$W/cm$^2$, which increases as the gap distance decreases and the strip thickness increases. However, when the peak power is normalized by the maximum external work done, an inverse relation is observed as the normalized peak power increases with a decrease of the gap distance and the strip thickness, as shown in Figure 4-7(b). Therefore, the optimal dimension of the device is not absolute and it can be selected depending on shape factor requirements for placement within a structure or other energy-harvesting environment.

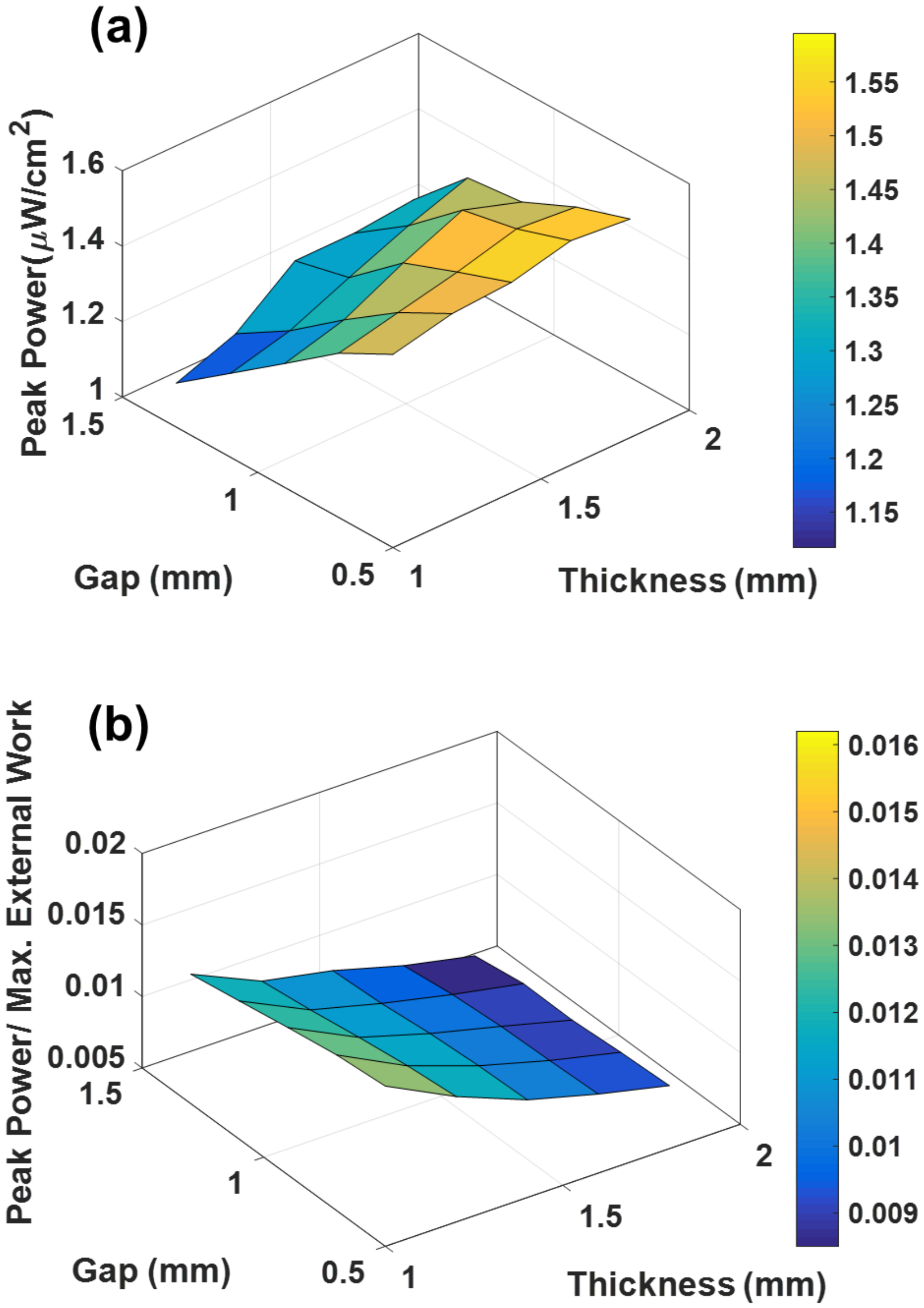

Figure 4-7: Parametric studies: (a) peak power with changing strip thickness and gap distance, and (b) peak power normalized with respect to the maximum external work done.

## 4.2 Model II - BCNC with a cantilever PZT oscillator

### 4.2.1 Model validation

The theoretical predictions and numerical simulations of the critical buckling configurations (i.e., buckling shapes right before mode transitions) of the first three modes for a non-prismatic column ($\alpha = 0.80$ / $\beta = 0.35$) are compared in Figure 4-8. It can be seen that the models are in good agreement in predicting the critical straight section length, which is the key factor for triggering the mode transitions. Larger discrepancies are found at the two outer curved sections, which are mainly caused by three reasons. First, the buckling shapes in the theoretical model assume that the flat segment only forms at the middle of the column. However, this ideal lower limit configuration cannot be achieved in reality. Second, the contact friction, which is neglected in the theoretical model, causes asymmetry on the buckling shapes of the numerical simulations. Third, using small deformation theory and linear strain leads to inaccuracies in the theoretical analysis as the buckling wave number and curvature increases [85, 243]. In spite of the noted shortcomings, the theoretical model is considered to provide an adequate prediction of the buckling morphologies and it was adopted to study the effect of the critical straight segment length on the column's local instabilities.

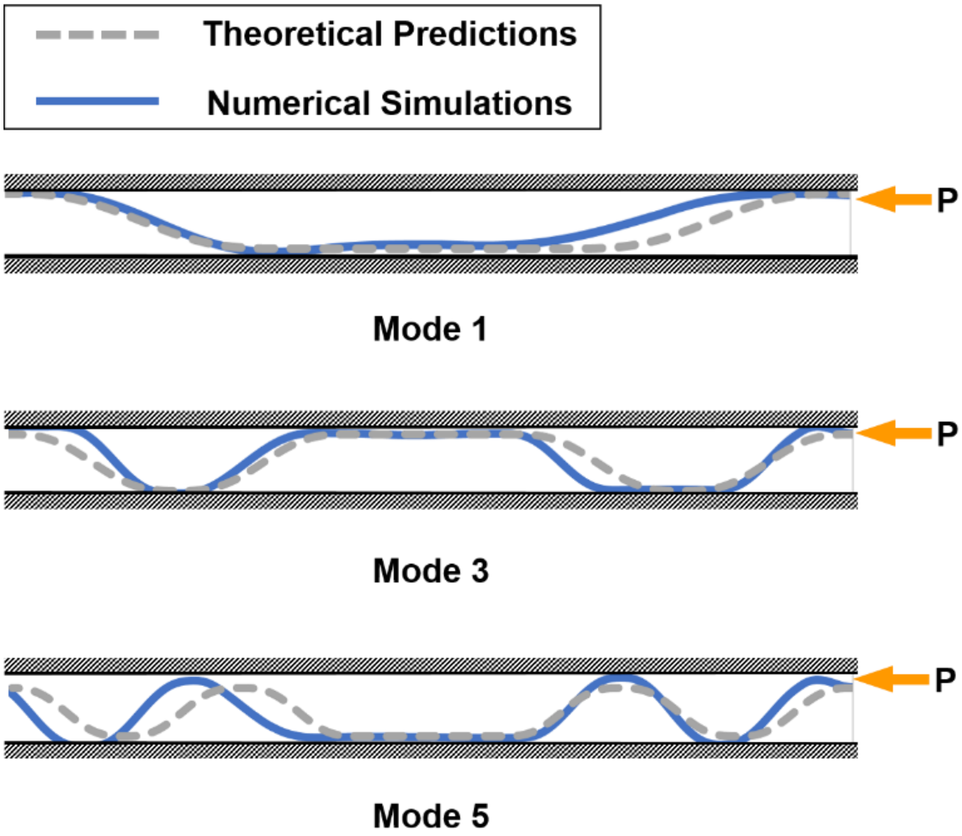

Figure 4-8: Comparison between the theoretical predictions and numerical simulations of the critical buckling configurations for the first three modes. The gap is scaled 3 times for clarity.

Experimental and simulation results for the first two mode transitions are summarized in Table 4-2. The force-displacement responses of the baseline design and two non-prismatic design cases ([$\alpha / \beta$] = [0.85/0.35] and [0.75/0.50]) are presented in Figure 4-9. The snap-through events for each buckling mode transition are circled. It can be seen that the FE simulations adequately captured the mode transitions, as well as the initial and end response stiffness. The differences between the simulated and experimental responses are due to uncertainty in modeling parameters, such as the actual imperfections, friction resistance between and strip and walls, and the boundary conditions. Nonetheless, the simulation approach is considered acceptable for the purpose of this study given that the simulations can adequately capture the number and onset of the mode transitions, the initial and end stiffness, and the magnitude of the load drops.

Table 4-2: Comparison of simulation and experimental postbuckling results.

| Case | | Mode 3 | | | | | | Mode 5 | | | | | |
|---|---|---|---|---|---|---|---|---|---|---|---|---|---|
| | | Disp. (mm) | | | Force (N) | | | Disp. (mm) | | | Force (N) | | |
| $\alpha$ | $\beta$ | Exp | Num | Diff | Exp | Num | Diff | Exp | Num | Diff | Exp | Num | Diff |
| 0.7 | 0.4 | 1.1 | 1.2 | 0.1 | 285 | 312 | 27 | 2.5 | 2.6 | 0.2 | 668 | 691 | 23 |
| 0.75 | 0.5 | 0.4 | 0.6 | 0.3 | 117 | 204 | 87 | 1.9 | 2.2 | 0.3 | 595 | 614 | 19 |
| 0.8 | 0.45 | 1.2 | 1.2 | 0.0 | 338 | 412 | 74 | 1.8 | 1.9 | 0.1 | 589 | 606 | 17 |
| 0.85 | 0.35 | 0.4 | 0.6 | 0.3 | 117 | 193 | 76 | 2.0 | 2.3 | 0.4 | 735 | 800 | 65 |
| 0.9 | 0.5 | 0.6 | 0.8 | 0.2 | 256 | 309 | 53 | 3.0 | 2.5 | 0.5 | 1216 | 1036 | 180 |
| Baseline | | 0.7 | 1.1 | 0.4 | 272 | 375 | 103 | 2.9 | 2.5 | 0.4 | 1083 | 962 | 121 |

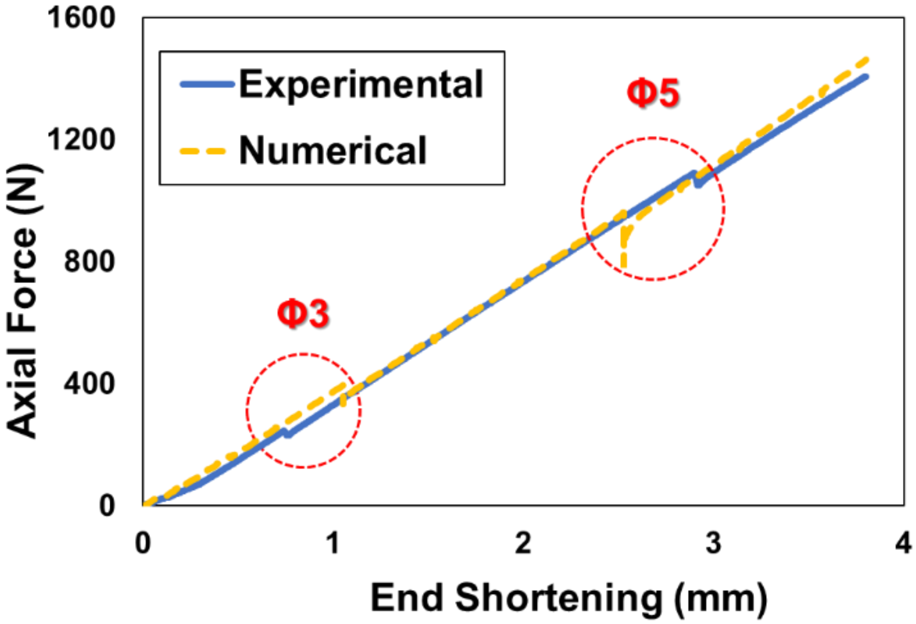

**(a) Baseline Prismatic Column**

Figure 4-9. Comparison of experimental and numerical force-displacement responses of the prismatic baseline column and two non-prismatic columns.

Figure 4-9 (cont'd)

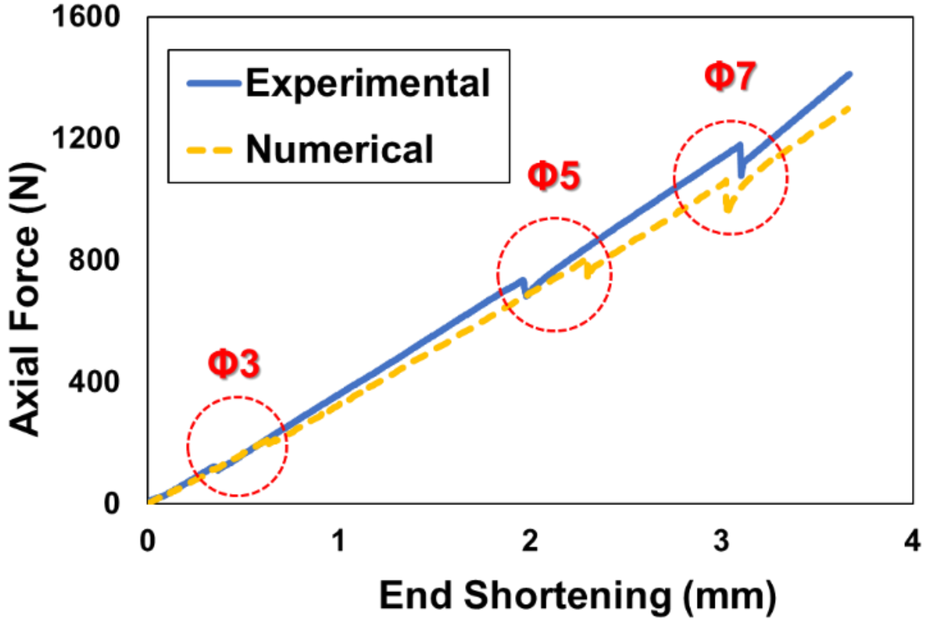

(b) Non-Prismatic Column (α = 0.75/ β = 0.50)

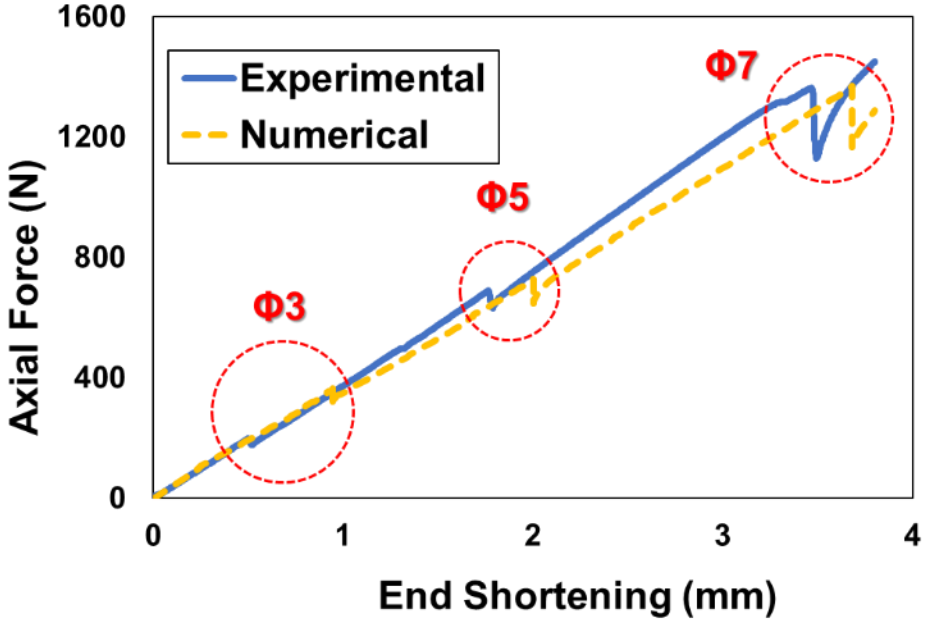

(c) Non-Prismatic Column (α = 0.85/ β = 0.35)

### 4.2.2 Mechanical response

The experimental configurations for each mode transition of the baseline column and a non-prismatic column ($\alpha$ = 0.85 / $\beta$ = 0.35) during the loading phase are shown in Figure 4-10. The line contact regions before each mode transition are also indicated in the figure. It can be observed that for both columns the snap-through events are always generated at the longest line contact region (shown by the red arrows). Thus, controlling the formation of the longest line contact region allows control of the buckling locations. The length of the straight segment increases with axial shortening. In the prismatic column there is no control of the buckling location since the distribution of the line contact segments changes as the mode configuration shifts. However, the longest straight segment is always located in the middle of the non-prismatic column (Figure 4-10 (b)) due to its larger bending resistance. This allows it to behave similar to the lower limit case proposed in Figure 2-6. The mode shapes of the non-prismatic strips also feature localized transverse deformations in the flexible segments that are superposed on the global buckling shape. This is due to the distribution of transverse deformations from traveling strain energy stress waves from the stiffer regions to the flexible ones after the snap-through mode transitions.

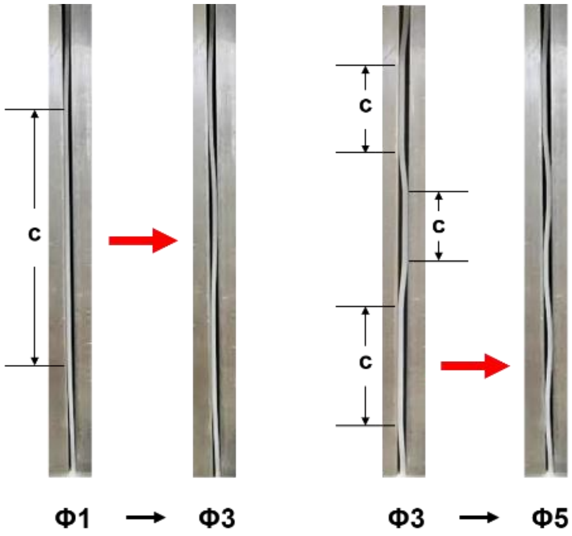

(a) Baseline Column

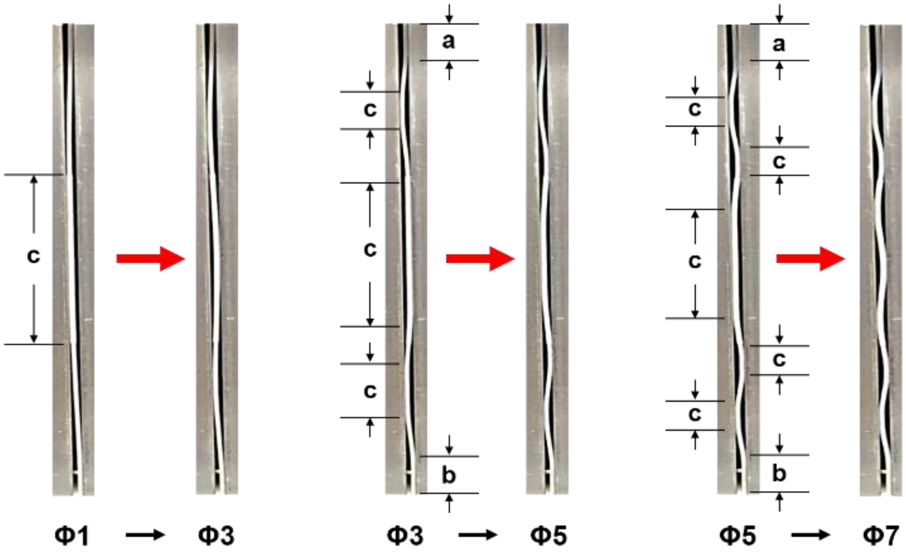

(b) Non-prismatic Column

Figure 4-10: Postbuckling transition process as obtained from experiments for (a) baseline design and (b) non-prismatic design case $\alpha = 0.85/\beta = 0.35$.

Figure 4-11 compares the change in length of the straight segment as a function of end shortening to a maximum of 2% strain for the baseline and non-prismatic columns ($\alpha = 0.85$ / $\beta = 0.35$), the results are from the theoretical model (Section 2.6.3) and normalized by the column length $L_0$. For both cases, the length of the straight section at the pre-buckling stage is clearly zero as end shortening increases until the column buckles and teaches one side of the walls. The line contact region keeps growing as compression proceeds and is followed by a downward jump upon reaching the critical point. The columns then re-stabilize at a higher buckling mode configuration until the next buckling limit is reached. The solid lines indicate the stable states during the postbuckling process and the dotted lines indicate the unstable mode transition phases. It can be seen that for the non-prismatic column the normalized critical straight section length at the transition to mode 3 is 0.35 (i.e., the same as $\beta$). This corresponds to the experimental results shown in Figure 4-10, where all of the middle segment length was in contact with the wall before buckling. As the buckling mode increases the line contact regions reduce in length to accommodate the increased number of buckling waves in the outer segments and the end shortening. Therefore, the middle straight section gets shorter each time the column jumps to a higher mode; which requires a larger end shortening to trigger the next buckling event, as shown in Figure 4-11.

Taking the transition to mode 3 as an example, the results in Figure 4-11 show that the non-prismatic column forms the straight line contact section quicker and reaches the critical limit sooner compared to the prismatic baseline column. This comparison holds true for every mode transitions shown, as indicated in Figure 4-11 by the much steeper slope of the curves representing the straight section length development with end shortening for the non-prismatic column. Therefore, in addition to permitting control of the buckling location, the non-prismatic design accelerates the development of local instabilities and is able to attain a higher number of buckling mode transitions under the same global deformation level (2% global axial strain) compared to the baseline uniform design.

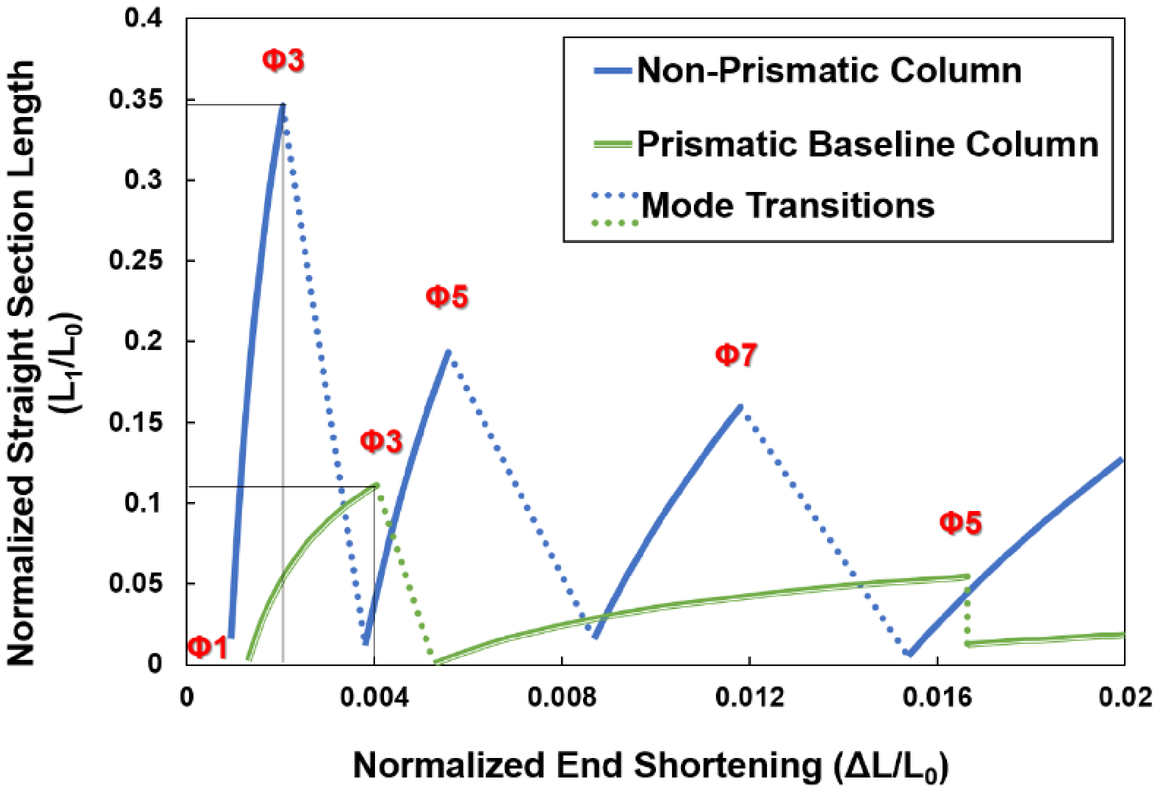

Figure 4-11: Development of the middle straight section length versus column end shortening from theoretical analysis (the data is normalized by the column length *L₀*) for the baseline design and non-prismatic design case $\alpha = 0.85/\beta = 0.35$.

The evolution of buckling shapes (i.e., normalized transverse deflection with respect to the gap distance $h_0$ of the strip) for each mode transition of the non-prismatic case ($\alpha = 0.85$ / $\beta = 0.35$) from the FE simulations is shown in Figure 4-12. The predicted buckling shapes and the mode transitions are consistent with experimental results in that every snap-through event is triggered at the middle thicker segment. Besides allowing control of the buckling location, stiffness variations along the column lead to a transient response after mode transitions that is quite different to that in prismatic columns. In the postbuckling response of a uniform strip the new mode shape stabilizes quickly after the snap-through buckling event and the column's deformed shape experiences minor changes until the next mode jump occurs. However, non-prismatic strips display a longer transient dynamic response following the snap-through buckling events and stress waves travel along the strip leading to the propagation of local buckling deformations within the global stable buckling shape. Once the stiffer region buckles a relatively larger deformation and curvature develops at the stiffer region compared to the rest of the column. However, the stored strain energy seeks minimization in its distribution along the strip and propagates to the thinner regions, which have lower bending stiffness, finally stabilizing at the lowest potential energy level. The wave's travelling direction is shown with arrows in Figure 4-12.

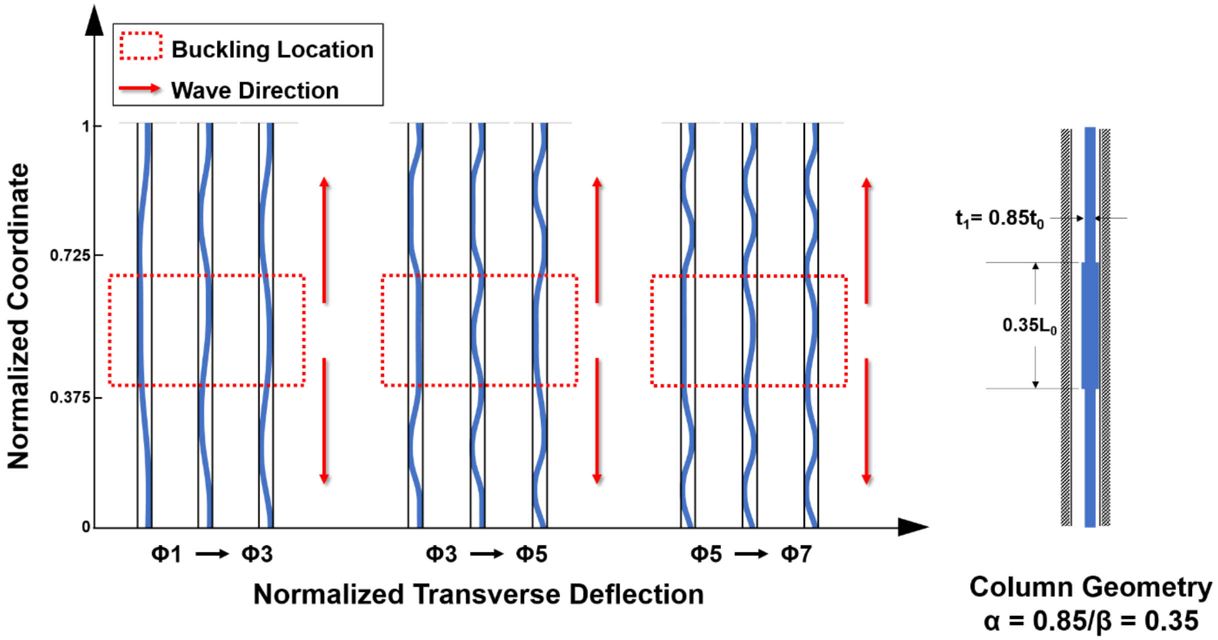

Figure 4-12: Postbuckling transition process as obtained from finite element simulations for non-prismatic design case $\alpha = 0.85 / \beta = 0.35$ ( the longitudinal coordinate is normalized by the column length $L_0$; the transverse deflection is normalized by the gap distance $h_0$).

It is also of interest to compare the postbuckling response features of different segments in the non-prismatic columns. The maximum acceleration, average acceleration and the number of acceleration impulses at the mid-span of each segment in the column are compared in Table 4-3 for five selected non-prismatic designs. The value shown for the outer segment is the average from the upper and lower thin segments. It can be seen that both the maximum and average acceleration at the controlled buckling location (thicker region) are significantly higher. This is attributed to a relatively larger mass and kinetic energy release at the middle thicker segment, where the buckling-induced high-rate motions were generated. Regarding the number of acceleration impulses: in most cases more events were found at the outer segments. This response feature is due to the propagation of stress waves towards these regions, which experience local motions in addition to the global mode transitions.

Table 4-3: Comparison of the absolute maximum acceleration, average acceleration of all impulses and the number of impulses at the mid-span of the thicker segment (controlled buckling location) and thinner segments for selected cases.

| Cases | | Abs. Max. Acc. ($10^3$ g) | | | Avg. Acc. ($10^3$ g) | | | No. of Acc. Impulses | | |
|---|---|---|---|---|---|---|---|---|---|---|
| $\alpha$ | $\beta$ | Outer Seg. | Middle Seg. | % Diff. | Outer Seg. | Middle Seg. | % Diff. | Outer Seg. | Middle Seg. | Diff. |
| 0.80 | 0.35 | 2.35 | 3.7 | 36.5 | 1.32 | 2.03 | 35.0 | 3 | 3 | 0 |
| 0.80 | 0.50 | 1.27 | 3.63 | 65.0 | 0.76 | 1.98 | 61.7 | 3 | 2 | 1 |
| 0.85 | 0.35 | 3.76 | 13.5 | 72.2 | 2.95 | 8.88 | 66.7 | 4 | 3 | 1 |
| 0.90 | 0.45 | 0.84 | 8.2 | 89.8 | 0.11 | 4.33 | 97.4 | 4 | 2 | 2 |
| 0.90 | 0.35 | 8.02 | 9.85 | 18.6 | 3.59 | 8.00 | 55.1 | 3 | 3 | 0 |

### 4.2.3 Parametric study

Experimental observations showed that when $\alpha$ was less than 0.7 the thicker segment would not be able to buckle due to insufficient force transfer from the thin segment and a kink was observed at the stiffness interface of the strip for the three segment case with $\alpha = 0.5$ during loading. When $\alpha$ was greater than 0.90 there was insufficient stiffness variation between the segments to make the non-prismatic column behave differently from a prismatic one. Thus, the range of $\alpha$ was selected to be $0.7 \leq \alpha \leq 0.9$. Forty-five cases of non-prismatic columns were numerically studied within this domain and the results are shown in Figure 4-13 as a response map for the non-prismatic column designs. The postbuckling response was evaluated by two parameters: the highest buckling mode shape reached and whether the buckling location was controlled (i.e., pre-determined) or uncontrolled. The design domains with a controlled buckling location are enclosed by the hatched region in the diagram. These results support the hypothesis that buckling location along the element can be contolled at the stiff segments by reducing the bending strain energy from these regions such that they remain straight and develop a line contact with the constraints, therefore dictating the triggering location of the snap-through buckling events. Limits to the influence of non-prismatic designs for controlled postbuckling response can also be identified in Figure 4-13 when the thickness and length ratios between segments reach extreme values. The response map thus provides guidance for designing non-prismatic column elements as energy concentrators to excite vibration-based piezoelectric transducers.

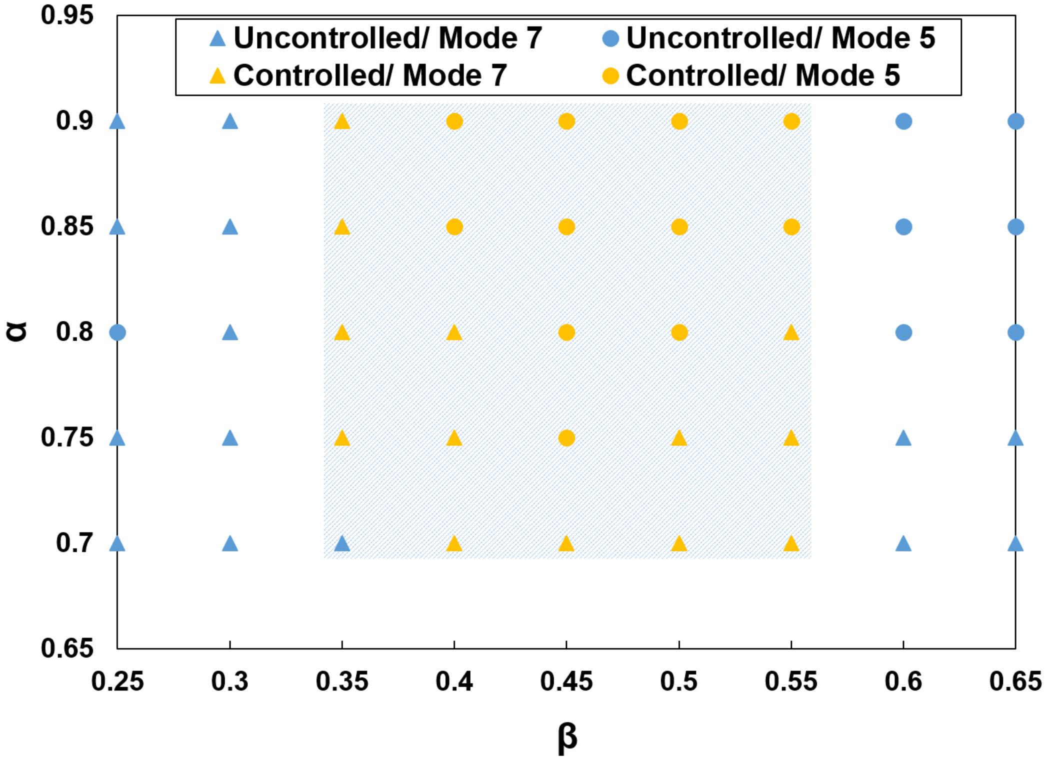

Figure 4-13: Effect of $\alpha$ and $\beta$ on the postbuckling location and highest achievable buckling mode for the non-prismatic column design. Hatched regions are design domains with controlled buckling response.

### 4.2.4 Dynamic features

The sequence of postbuckling events was assessed from the transverse accelerations at the top, middle (thickened), and bottom segments during the postbuckling response, since the buckling location is related to the place of highest kinetic energy release. Figure 4-14 shows the acceleration time history for each segment of the non-prismatic case ($\alpha$ = 0.85 / $\beta$ = 0.35) from the FE simulation. The buckling mode shapes are labeled according to each acceleration impulse. It can be seen that for each buckling event, the highest acceleration magnitude is always in the middle segment, albeit with a slight forward time shift. This means that buckling is triggered in the middle segment and that the energy propagates to the top and bottom segments. This result confirms that the sequence and location of the postbuckling events can be tailored and controlled through local stiffness variations on the strip. In addition, the small peaks on Figure 4-14 that are not labeled are due to the motion created by the noted traveling stress waves. Even though they are small compared to the other major impulses due to buckling, they are still large enough to count as a valid energy input to the target energy harvesters, that is, they exceed 10 g. Moreover, the non-uniform design largely increased the acceleration magnitude from the order of $10^3$ g to $10^4$ g for most of the non-prismatic cases.

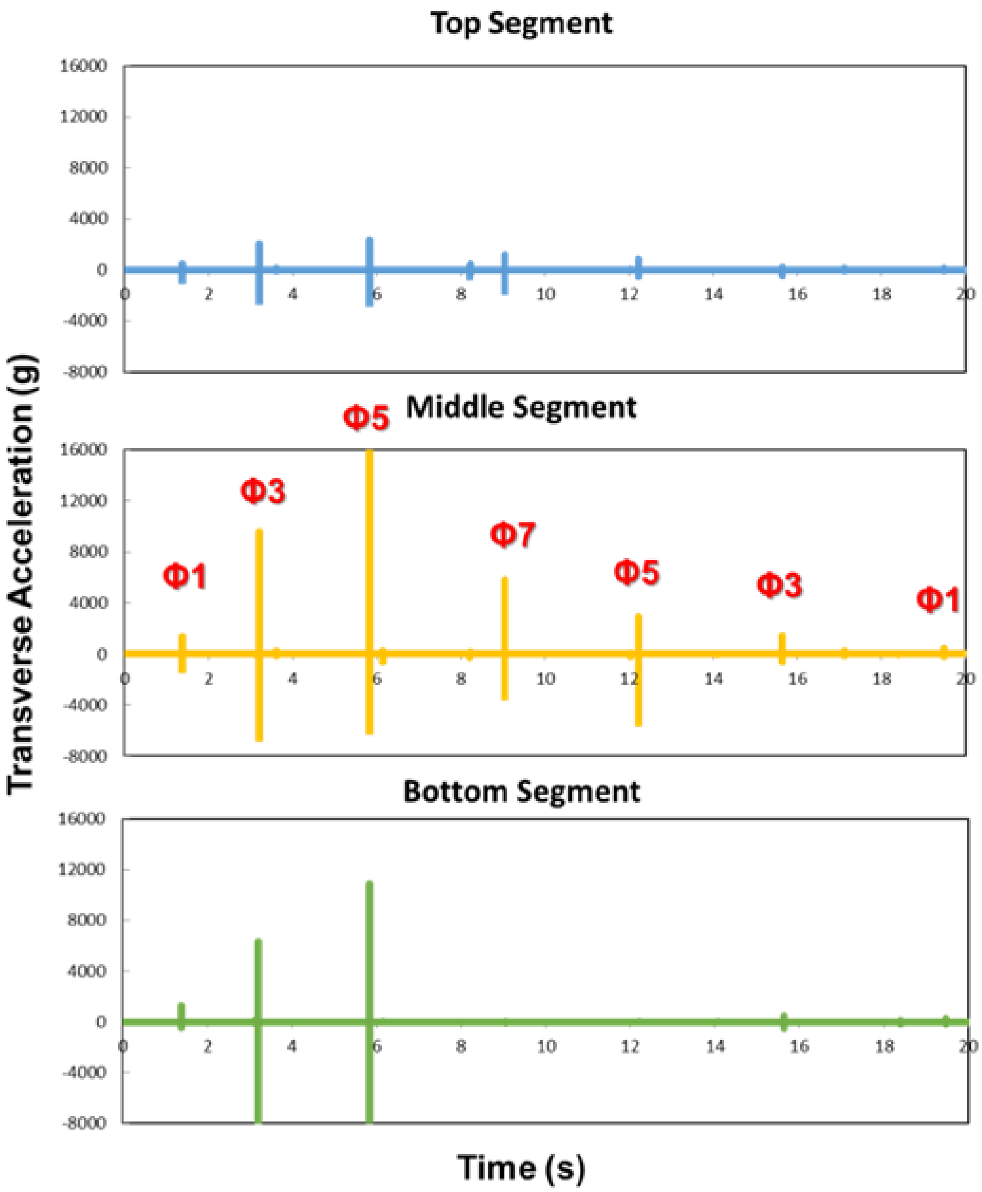

Figure 4-14: Acceleration time history of case ($\alpha = 0.85$ / $\beta = 0.35$) for each segment along the strip from a finite element simulation.

The acceleration impulses generated by the postbuckling mode transitions of the bilaterally constrained column act as a transverse base input excitation to a piezoelectric energy harvesting transducer (cantilever bimorph) to generate voltage output. The piezoelectric oscillator is attached to the slender axially loaded column element (with the cantilever's longitudinal axis perpendicular to the supporting column's own longitudinal axis so that it responds as a single-degree-of-freedom oscillator (Figure 2-9(c)). The correlation between the base acceleration input (resulting from the snap-buckling events of the axially loaded bilaterally constrained column) and the generated piezoelectric voltage output from a bimorph PVDF cantilever with properties shown in Table 2-3 is illustrated with simulated results in Figure 4-15. The acceleration impulses have positive and negative magnitudes (directions normal to the strip's surface) as a result of the column's wall impact and reaction directions. Therefore, a synthetic acceleration record (Figure 4-15 (a)) with impulses of varying magnitudes: equal values in both directions (1s – 3s), larger value in the positive direction (4s – 6s) and larger value in the negative direction (7s – 9s) was designed to represent different scenarios in the dynamic response of a bilaterally constrained strip during the elastic postbuckling response. The acceleration record was then used as the base excitation for the bimorph piezoelectric cantilever beam and the generated voltage output calculated using a simplified Rayleigh-Ritz approach [266] is shown in Figure 4-15 (b). As expected, the generated voltage clearly corresponds to the acceleration pulses. It can also be seen that the magnitude of the output voltage is directly proportional to the magnitude of the acceleration impulse. Therefore, enhanced performance of the energy harvesting device, from the system's mechanical aspect, requires that the targets for the elastic postbuckling behavior of the bilaterally constrained strip be: a) increasing the number of acceleration impulses or mode transitions, b) increasing the magnitude of the accelerations impulses, and c) controlling (or predetermining) the buckling locations. The piezoelectric responses are evaluated in later sections under these parameters. It is recognized that energy harvesting can also be enhanced by modifying the piezoelectric oscillator, but such an approach was within the scope of this study.

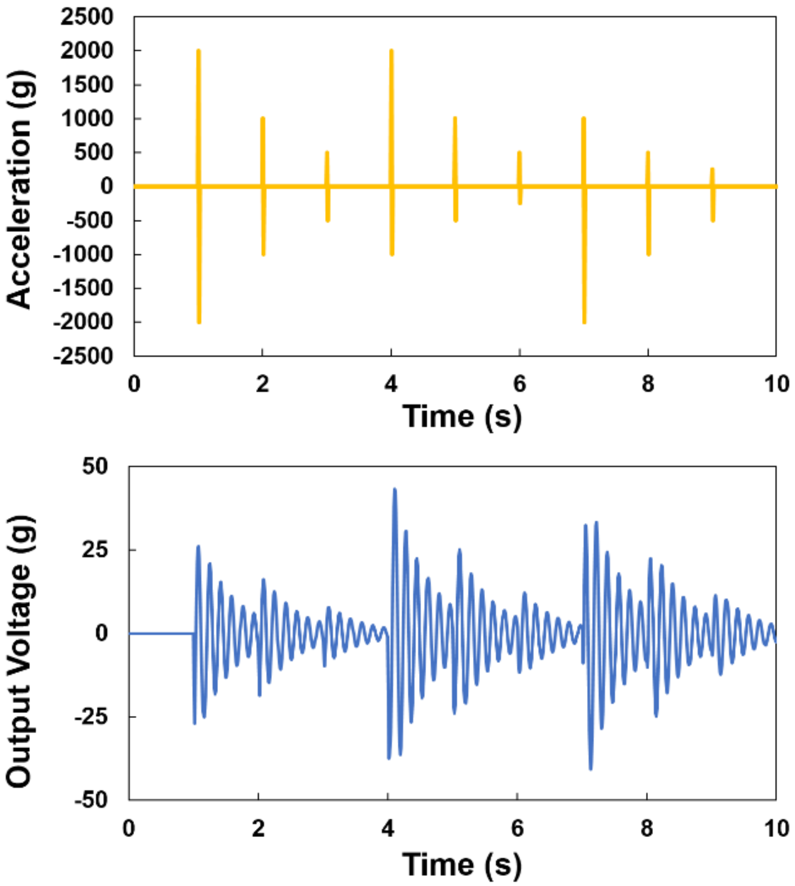

Figure 4-15: Piezoelectric voltage output by a bimorph piezoelectric oscillator from a set of acceleration impulses.

### 4.2.5 Piezoelectric response

Figure 4-16 presents, from experiments, the applied axial force and the output piezoelectric voltage of a PVDF oscillator transducer (Table 2-3) attached to a prismatic baseline column and a non-prismatic column ($\alpha = 0.80$ / $\beta = 0.40$) in the configuration shown in Figure 2-9(c), for a full loading/unloading 20 s cycle. It can be clearly seen that the non-prismatic column generated a higher level and more sustanable voltage output. Since the buckling location is uncontrolable in the prismatic column, the local buckling motions are not always at the mounting location of the harvester (column mid-height) for every mode, which leads to a much lower level of harvested power. By comparison with the baseline column, the increased number global mode transitions of the non-prismatic column provides a more continous series of acceleration impulses to the oscillator, and the predefined buckling location at the column mid-height allows all the mode transitions to create larger levels of acceleration input to the PVDF oscillator. Therefore, enhanced performance of the energy harvesting device was achieved by controlling the elastic postbuckling behavior of the non-prismatic strip with increased/enlarged acceleration impulses and a predefined and concentrated buckling location.

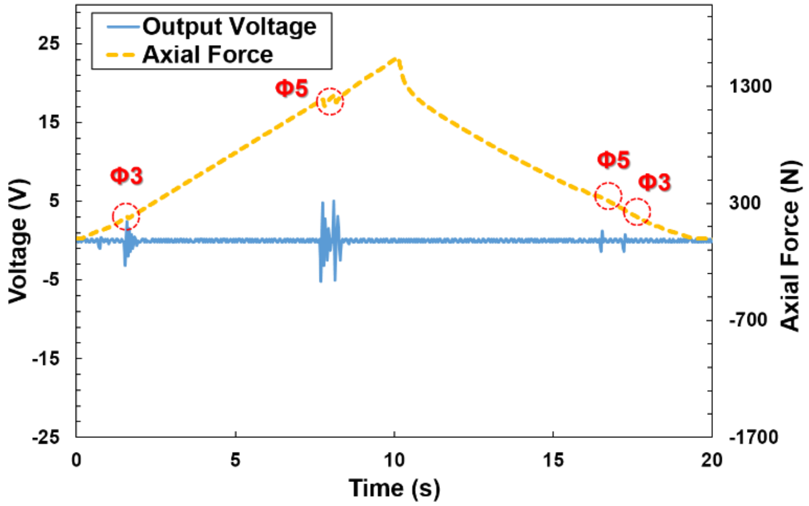

**(a) Prismatic Baseline Column**

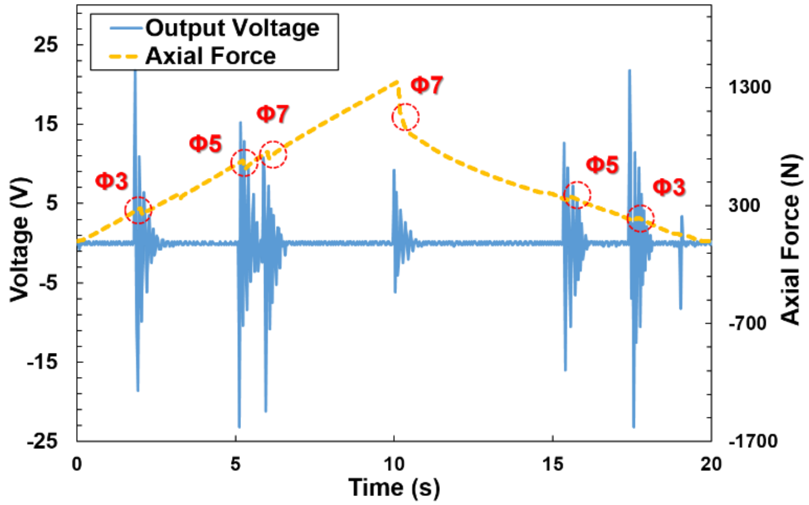

**(b) Non-Prismatic Column**

Figure 4-16: Piezoelectric output voltage generated for (a) prismatic baseline column and (b) non-prismatic column with $\alpha$ = 0.80/ $\beta$ = 0.40.

## 4.3 Conclusions

This chapter presented the evaluation of the approach for harnessing elastic postbuckling of axially compressed bilaterally constrained columns compounded with piezoelectric materials to convert strain energy into useful electric power. Two model designs based on this concept were evaluated: (1) bilaterally constrained column with a bonded PZT film layer, and (2) bilaterally constrained non-prismatic column with a PZT oscillator, through theoretical analyses, numerical simulations, and experimental evaluations. The following conclusions were drawn from the results presented in this chapter:

(1) A new approach for converting quasi-static deformations into usable electric energy to power energy-efficient micro- sensors and devices, by using an axially compressed bilaterally constrained strip with a bonded unimorph piezoelectric layer was demonstrated. A simple theoretical model, based on an energy-method, was used to predict the corresponding strain of the strip's buckled configuration for the purpose of calculating the electrical energy generation. An experimental investigation and finite element simulations were conducted to validate the theoretical results. The analytical model allows accurate prediction on the axial strain caused by the buckled configuration of the strip as a function of its axial shortening. Numerical and experimental results were shown to be in good agreement with the analytical analysis. Experimental results from the prototyped device show that a peak power of 1.33 $\mu$W/cm$^2$ can be generated, which is independent from the deformation loading rate, and which can adequately provide power supply for low-power budget devices. Results from a parametric study provide design guidance on selecting dimensions for the energy-harvesting device for different form-factor requirements.

(2) This design concept demonstrated that the buckling location of multiple mode transitions in bilaterally constrained columns under compression can be controlled by introducing flexural stiffness variations along the column length. A theoretical model was developed based on the stationary potential energy principle through a simplified approach for predicting growth of the critical line contact segment length and the column's buckling morphologies as axial compression proceeds. Non-prismatic designs (obtained through thickness variations in discrete form along the column length) increase local instabilities in the elastic postbuckling regime, which increases the number of buckling mode transitions compared to prismatic columns for the same global strain level. Results showed that increased stiffness regions in non-prismatic columns are able to define where local buckling will be triggered, such that columns with stiffness variations within an identified design domain can attain a controllable location for the buckling events. Therefore, a predefined high kinetic energy release spot can be designed on the strip. This feature allows predicting where buckling will occur so that piezoelectric oscillators can be optimally placed on the strip for use in energy harvesting devices. The direct relation between the acceleration base input and the voltage output of piezoelectric oscillator transducers allows the tailorable postbuckling response features of non-prismatic columns to be used as a multi-stable energy concentrator strip with enhanced performance, in terms of more sustainable voltage output from mounted piezoelectric oscillators, for use in quasi-static micro-energy harvesting devices.

# Chapter 5

# ENERGY DISSIPATIVE MATERIALS – RESULTS

Results from experimental evaluations, theoretical analyses, and numerical simulations of the energy dissipative materials concept proposed in Chapter 3 are presented in this chapter. Experimental results from 3D printed prototypes are shown to verify their recoverable and repeatable response and rate-independent energy dissipation of the multi-unit material systems under cyclic shear loading. After experimentally validating the theoretical models and numerical simulation, numerical results are used to predict the behavior of the single-beam unit element with different geometries, and theoretical results are obtained for the optimal energy dissipation of the multi-unit material systems for a given unit geometry. Results from parametric studies based on the theoretical model are presented at the end of the chapter to explore the design space of the proposed materials.

## 5.1 Experimental results

Two beam geometries ($\theta = 25°$, $t/L = 0.17$ and $\theta = 40°$, $t/L = 0.18$) were used as the unit elements for all the test prototypes presented in this chapter. Experiments were performed on two 3D printed single-beam units and three multiple-unit structures (Figure 3-5a and Figure 3-5b) to characterize their shear behavior and showcase the design concept under both half- and full-cycle loading. The tested structures were initially placed in their undeformed states, and the in-plane shear deformation was applied as a relative vertical displacement along one edge of the test sample with respect to the other fixed edge. Testing was conducted at three deformation rates: 5 mm/s, 10 m/s and 15 mm/s.

### 5.1.1 Single-unit beam response

Experiments on two 3D printed single-beam units with geometries ($\theta = 25°$, $t/L = 0.17$ and $\theta = 40°$, $t/L = 0.18$) were first performed. The mechanical responses of the single-beam units are shown in Figure 5-1a and Figure 5-1b. To better compare between different structure geometries, a stress measure was calculated by normalizing the reaction force by the number of beam elements in the columns (i.e., $m$) and their unit geometry; and the strain is the displacement normalized by the maximum displacement applied during the test ($\Delta_{max}$). Two observations are noted. First, the response curves of both units are consistent for the different deformation rates, which is indicative of a small rate effect from the viscoelastic nature of the polymer material in the 3D printed samples. Second, there is a small deviation between the loading and unloading paths. From experimental observation, this deviation is due to the unavoidable eccentricity from the alignment between the loading frames when shear deformation was applied (see Figure 3-6). Nonetheless, the resulting enclosed areas are small and it is not considered to contribute towards energy dissipation in the system.

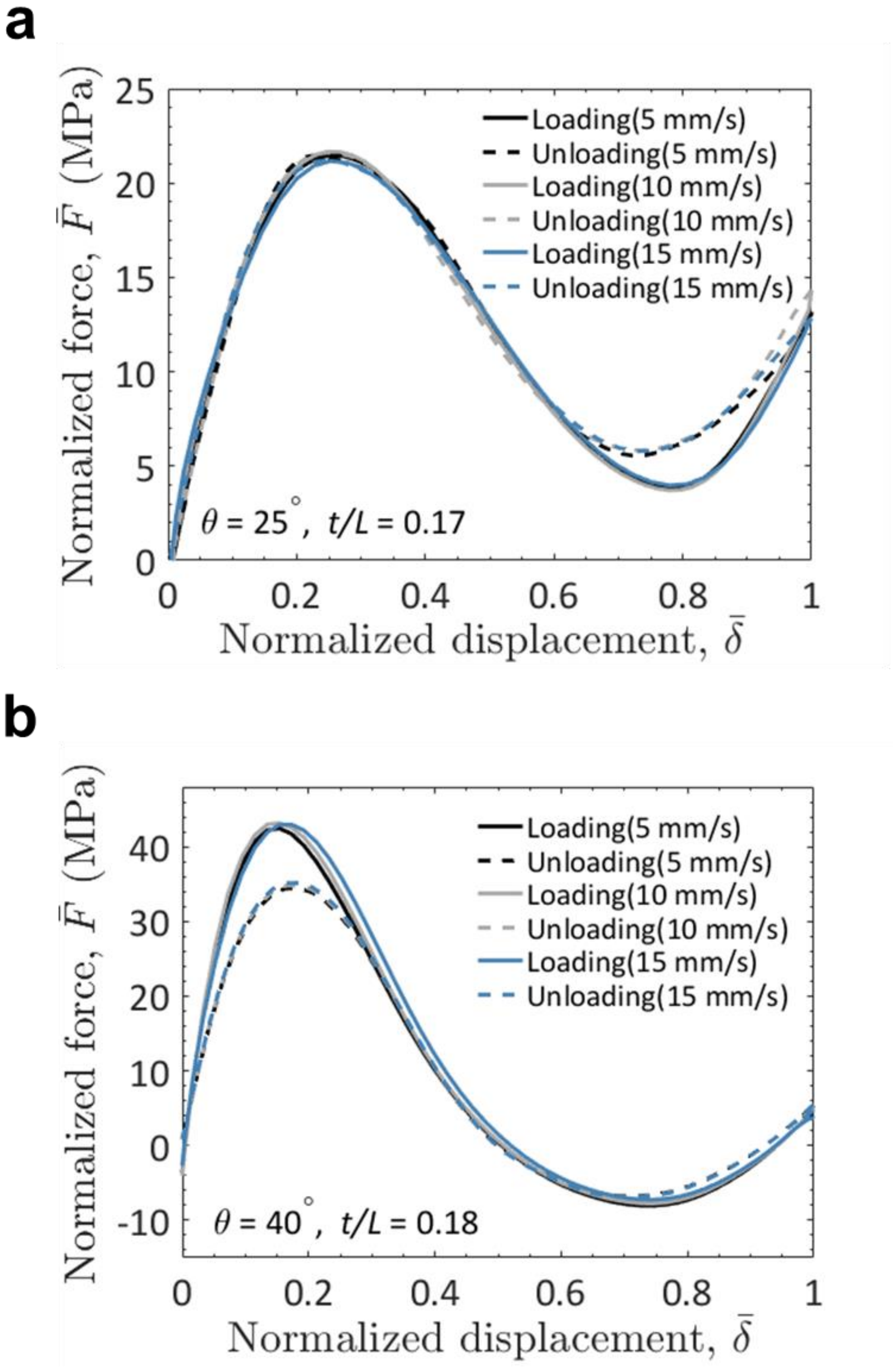

Figure 5-1: Experimental results of single beam units. a) Stress-strain response of single beam ($\theta$ = 25°, $t/L$ = 0.17). b) Stress-strain response of sample ($\theta$ = 40°, $t/L$ = 0.18). All samples were loaded at various strain rates (5 mm/s, 10 mm/s, and 15 mm/s). Note: the normalized force (stress) $\bar{F}$ equals to $FL^3/mIh$, and the normalized displacement (strain) is defined as $\Sigma\delta/\Delta_{max}$.

### 5.1.2 Multiple-unit system response

The two multiple-unit structures in Figure 3-5a were also loaded at the three noted deformation rates, and the measured shear stress-strain responses for the $\theta = 25°$ and $\theta = 40°$ systems are shown in Figure 5-2c and Figure 5-2d, respectively. It is immediately obvious that, unlike the single-beam units, the multi-unit structures display hysteretic force-deformation responses with a large enclosed areas and thus energy dissipating capacity. Under the applied shear deformation, the beam elements within the columns deform simultaneously and snap to their deformed state once their critical stress is reached. Due to manufacturing imperfections a given beam in the column stack will reach its critical stress first, and this effect will lead to one column reaching essentially simultaneous snap-through buckling of all its beams. This deformation process is passed on to another column as loading proceeds. The applied shear deformation was stopped when all columns switched to their buckled configuration. The test unit was then unloaded by reversing the deformation to the initial positon and the structure snapped back column by column during this process until all columns (and their beams) returned to their initial undeformed configuration in sequential snap-through motions. Because of manufacturing imperfections, the snap-through sequence of the columns may vary in different loading cycles. Sequential images at different strains of the deformation response of the one half-cycle structure ($\theta = 25°$, $t/L = 0.17$, $m, n = 12, 8$) due to the applied shear during loading and unloading are shown in Figure 5-3.

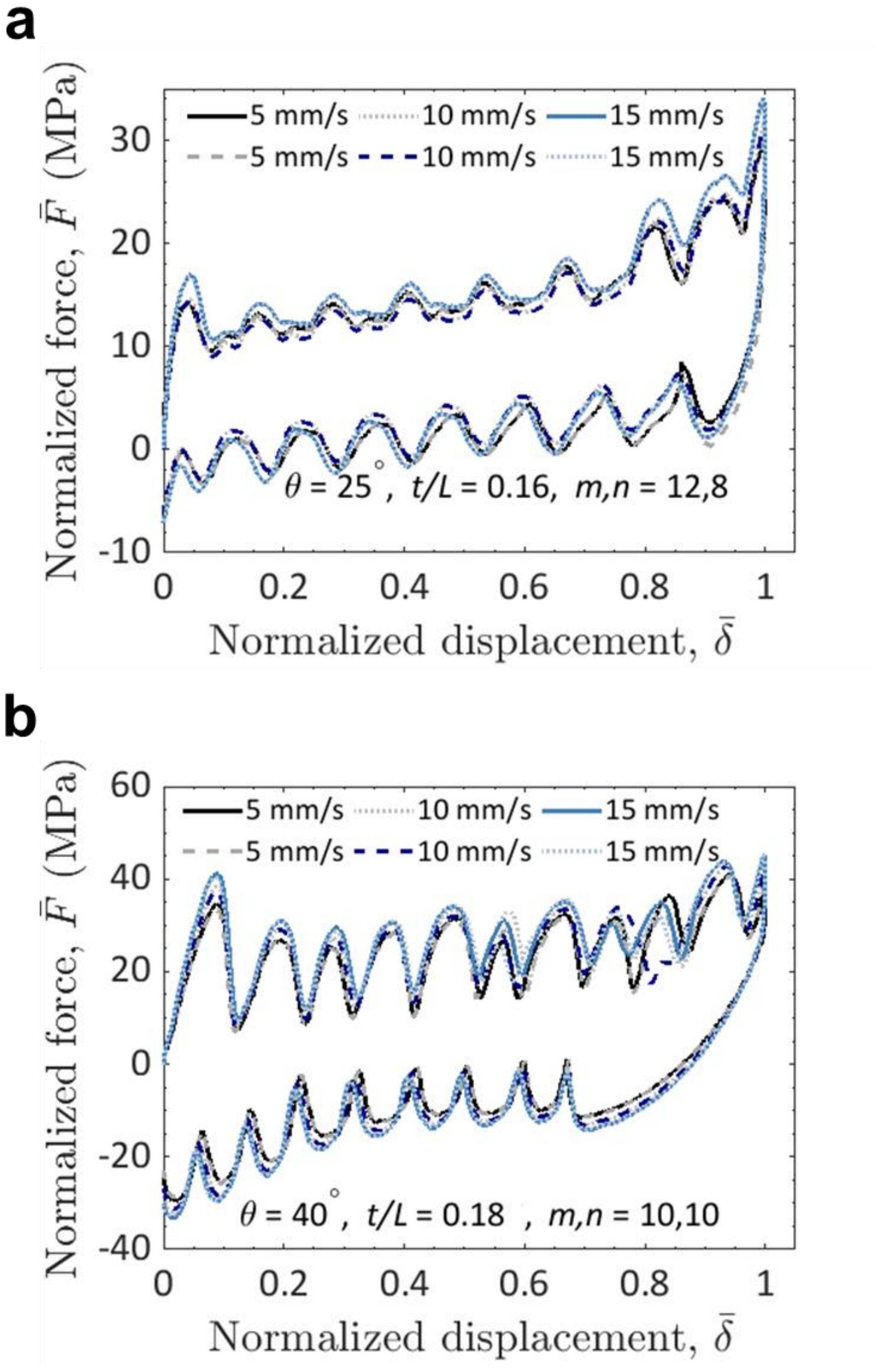

Figure 5-2: Stress-strain response of multiple-unit material prototypes for half-cycle shear loading condition with (a) $\theta = 25°$, $t/L = 0.17$, $m, n = 12, 8$), and (b) $\theta = 40°$, $t/L = 0.18$,7 $m, n = 10, 10$. All samples were loaded at various strain rates (5 mm/s, 10 mm/s, and 15 mm/s). Note: the normalized force (stress) $\bar{F}$ equals to $FL^3/mIh$, and the normalized displacement (strain) is defined as $\Sigma\delta/\Delta_{max}$.

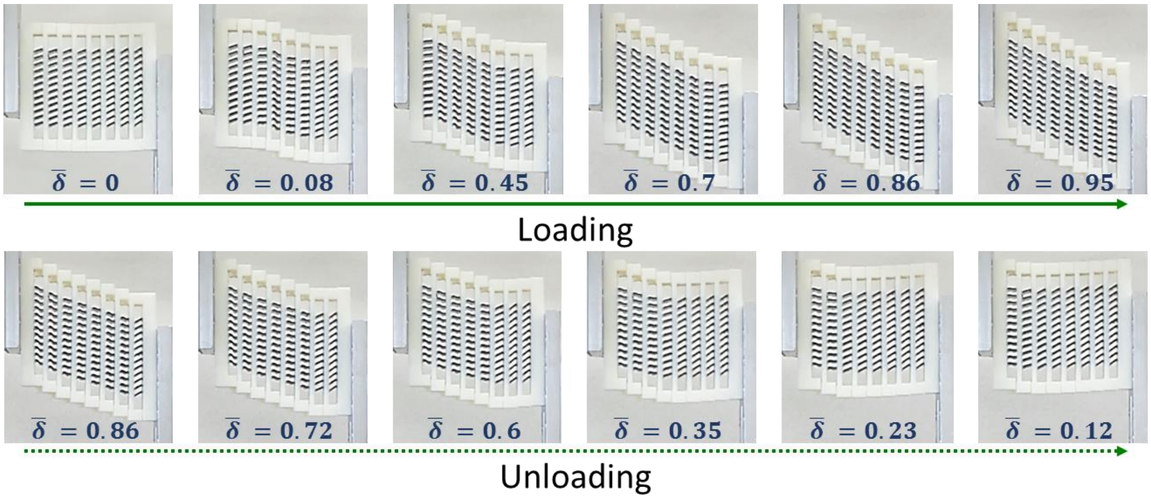

Figure 5-3: Sequential deformation process of the sample ($\theta = 25°$, $t/L = 0.17$, $m, n = 12, 8$) under a shear loading/unloading cycle.

For a given base material, the critical stress limit is defined by the beam unit geometry. Figure 5-2a and Figure 5-2b show that the structure with $\theta = 25°$, $t/L = 0.17$ has average peaks around 20 MPa and the structure with $\theta = 40°$, $t/L = 0.18$ has average peaks around 40 MPa, which are consistent with the responses of the corresponding single-beam geometry, see Figure 5-1a and Figure 5-1b. As each column snaps-through at the critical stress limit, it results in a peak on the stress-strain curve and followed by a negative stiffness region. The system regains a positive stiffness as the load resisted by the un-buckled columns provide a stable equilibrium path until another undeformed column reaches its critical stress limit. Thus, the number of units in a row, or number of columns, (i.e., *n*) controls the number of peaks and the number of unstable regions in the response. Ideally all the peaks in the response should be identical since the columns are in a series connection that deforms sequentially (one at a time) under the applied end displacement, and the columns that experience snap-through buckling should not deform further as the total displacement increases. However, gravity and friction resistance at the sliding mechanisms on the rigid end-constraining segments affect the experimental response and lead to additional displacement transfer to the snapped columns that deforms them beyond their snapped state. These factors in the experiments added a stiffening effect on the response curves and also resulted in a residual force on the structure when the applied displacement was removed. Nonetheless, it is clear the response is repeatable and stable under cyclic shear loading, and that its features are characterized by the structures' unit geometry and the number of units in series connection ($n$).

### 5.1.3 Full-cycle loading condition

In the material structures designed for a half-cycle condition (Figure 3-5a), the shear deformation takes place in a single direction, and the response cycle only occurs in the positive domain of the stress-strain diagram. The deformation process of the full-cycle structure prototype (Figure 3-5b), for which a fully-reversed shear deformation cycle takes place, is shown in Figure 5-4a. Of the ten columns in this structure, five have their beam units tilted to permit deformation in one direction while the other five feature a beam inclination that allows deformation in the other direction, and the columns were alternatively arranged to allow fully reversed cyclic loading within a single structure. Under an applied displacement, the columns with beams aligned with the active loading direction deform in a sequential manner while the columns with beams aligned in the opposite direction remain at their undeformed states. The same deformation process takes place by the columns with oppositely aligned beams when loading reverses to the other direction. Each loading direction activates snap-through instabilities in five columns, which leads to five jumps in the stress-strain curves in both the positive and negative domains; and generates a hysteresis area that covers the entire response diagram. This sample was also tested at three different deformation rates and the shear stress-strain responses are shown in Figure 5-4b. As learned from the half-cycle test units, the response was also repeatable and rate-independent under full-cycle shear deformations.

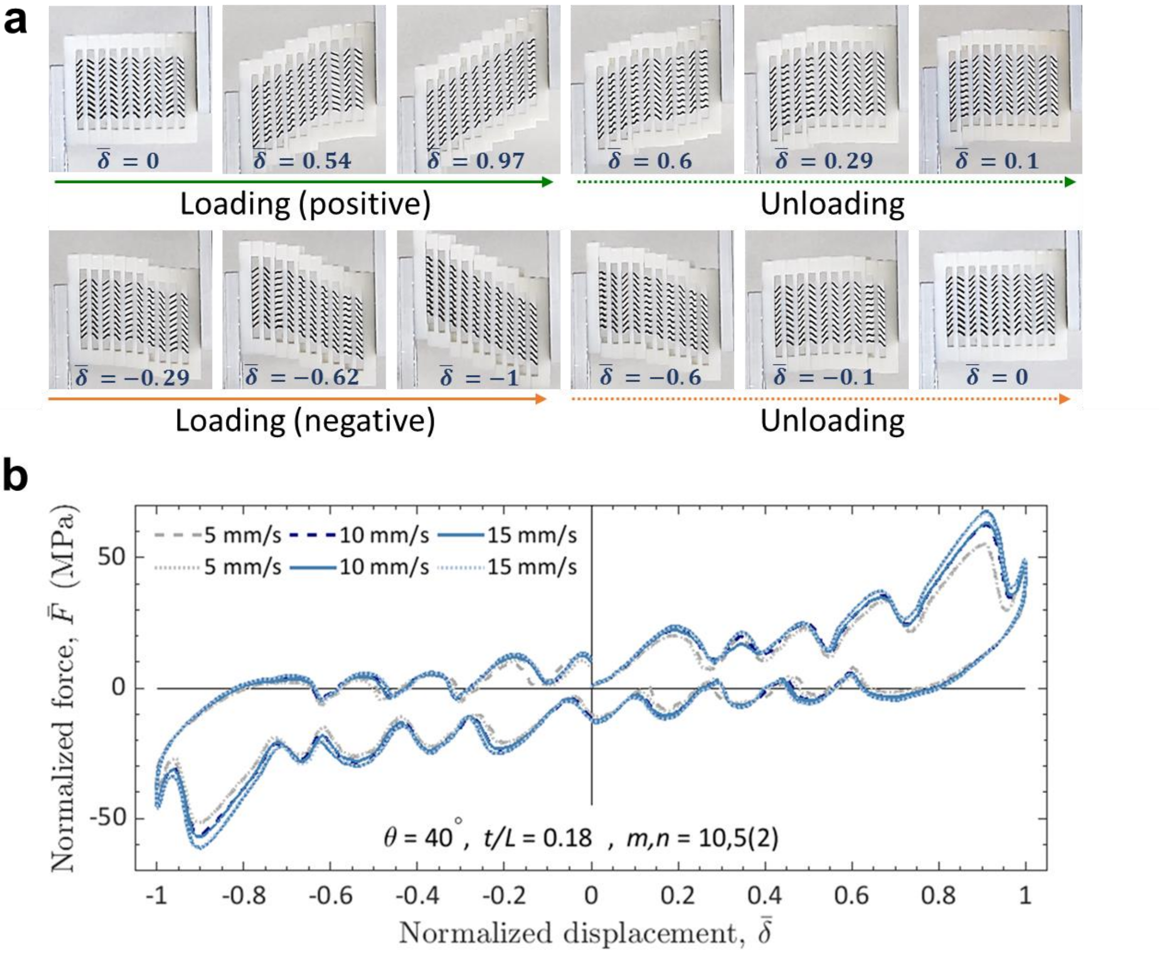

Figure 5-4: Experimental results of a multiple-unit material prototype for full-cycle shear loading condition ($\theta$ = 40°, $t/L$ = 0.18, $m$, $n$ = 10, 5×2). a) Sequential deformation process of the sample under a full-cycle of shear deformation. b) Stress-strain response of the sample at various strain rates. All samples were loaded at various strain rates (5 mm/s, 10 mm/s, and 15 mm/s). Note: the normalized force (stress) $\bar{F}$ equals to $FL^3/mIh$, and the normalized displacement (strain) is defined as $\Sigma\delta/\Delta_{max}$.

### 5.1.4 Discussions

The polymer material used for the elastic beam units (TangoBlackPlus) is known to have hyperelastic behavior (see Figure 3-8). However, the mechanism used in the proposed design concept to realize energy dissipation is based on the 'twinkling' phenomena and not the viscoelastic nature of the base material. This is confirmed by noting from Figure 5-2a, Figure 5-2b , and Figure 5-4a that there is only a small difference between the response curves of the multiple-unit structures when tested at different strain rates. While the small differences in the responses can be attributed to the viscoelasticity of the base material, its effect is small and it can be concluded that proposed energy dissipation mechanism is preserved without any viscous material effects. This claim is also supported by the analytical model presented in Section 3.5. Thus, the shear stress-strain response of the designed material system is dependent on its architecture but independent from the external loading rate.

## 5.2 Model validation

The numerical (see Section 3.6 for details) and experimental stress-strain responses of two structures with multiple units ($\theta = 25°$, $t/L = 0.17$, $m, n = 12, 8$ and $\theta = 40°$, $t/L = 0.18$, $m, n = 10, 10$) are compared in Figure 5-5. The numerical simulation takes into consideration the friction between the rigid constraining segments when the structures open up during loading, and is considered to be in good agreement with the experimental traces. However, the numerical simulations become computational expensive when the number of unit elements increases and were further used only for predicting single element response. Thus, the simplified analytical model presented in Section 3.5 was used to explore the effect of number of unit elements $n$ on the material structure behavior for a given unit geometry.

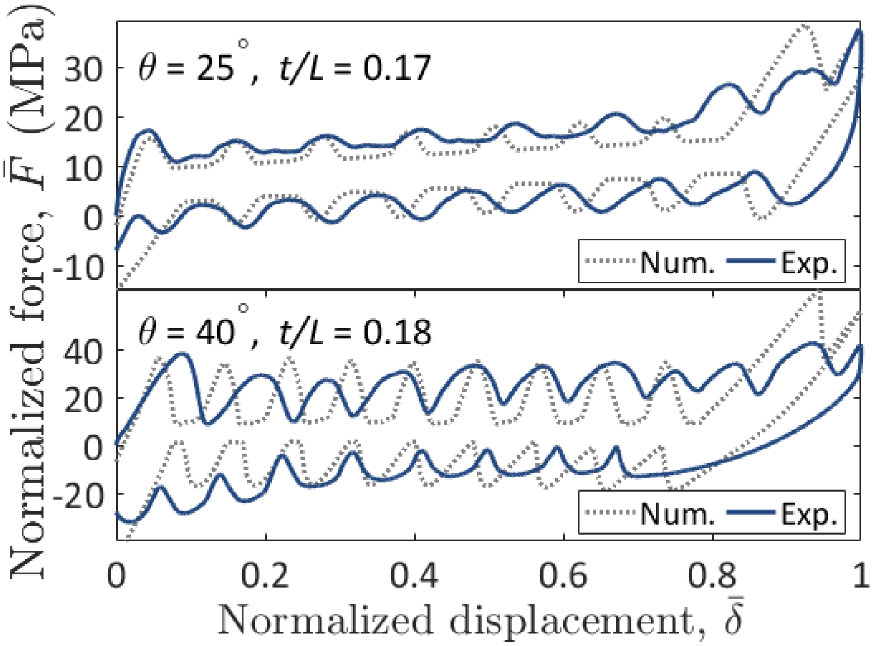

Figure 5-5: Experimental and numerical stress-strain response for two multiple-unit structures for *θ* = (25°, 40°), *t/L* = (0.17, 018), and *m*, *n* = (12, 8; 10, 10).

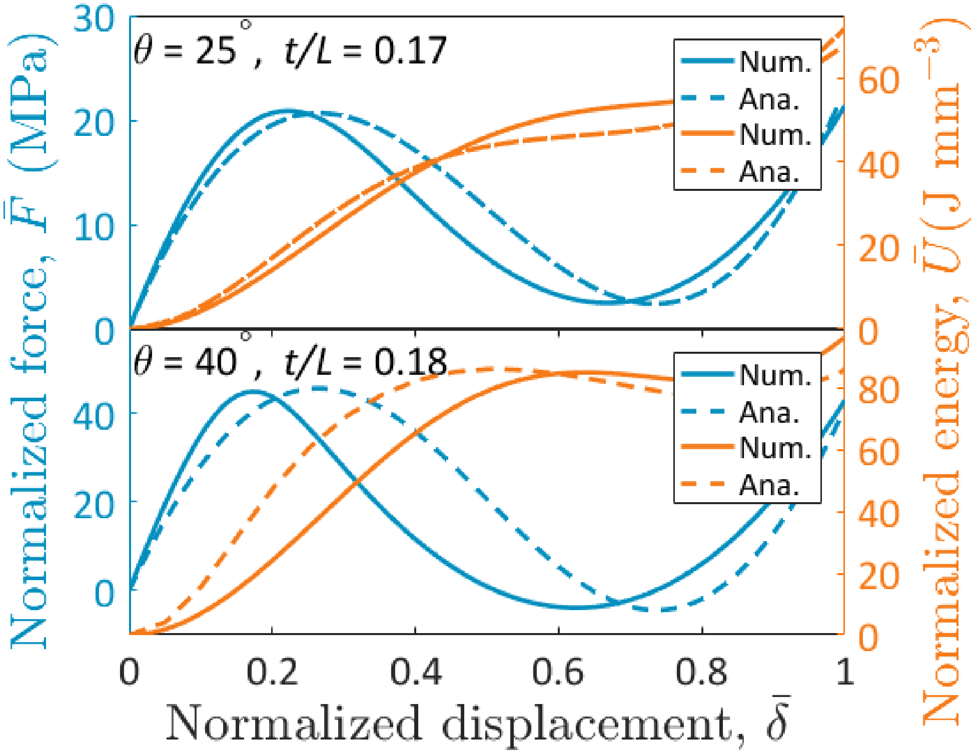

Figure 5-6: Numerical and analytical stress-strain and strain energy responses for two unit beams for *θ* = (25°, 40°) and *t/L* = (0.17, 0.18). The normalized strain energy equals to $UL^3/mnIh$ with the unit in MPa or J/mm$^3$.

Figure 5-6 compares numerical and analytical results of the stress-strain and strain energy responses of single elements with $\theta = 25^{\mathrm{o}}$ and $\theta = 40^{\mathrm{o}}$. It can be seen that the negative stiffness region caused by a release of the system stored strain energy is reflected as a non-convex energy curve. The simplified model can qualitatively capture the snap-through behavior of the unit beams in terms of critical forces, as well as the maximum and minimum energy; which is adequate to predict the multi-unit system response for a given material architecture.

## 5.3 Optimal energy dissipation

The effect of $n$ on the amount of energy dissipated in the structure was explored analytically using unit elements with $\theta = 25°$ and $t/L = 0.174$. The force-deformation response for a half-cycle shear loading condition is presented in Figure 5-7. It can be seen that when the number of units is lower than three the loading and unloading paths are coincident, with negative stiffness regions but no energy dissipation. This response follows from the fact that the unstable motion of the unit's DOFs (degrees-of-freedom) are imposed/stabilized by the applied deformation and the boundary conditions. When $n$ increases to three the middle element's DOF is free to become unstable under the applied displacement, which leads to energy dissipation of the system – as seen by the areas defined by the different loading and unloading paths. As $n$ is further increased, more DOFs from the inner connected elements are free to experience an unstable response, which leads to higher energy dissipation and reflected as an enlarged hysteresis area. The distance (deformation) between the unstable 'jumps' in the force-deformation response curve reduces as more stable equilibrium paths are provided by the increased number of elements in the system, which in the limit results in a smooth response curve that encloses a region such that it becomes defined by two flat horizontal lines at the critical stress values and the two stable equilibrium paths. This leads to an elastic-plastic-type behavior [267, 268] of the proposed structures that is recoverable.

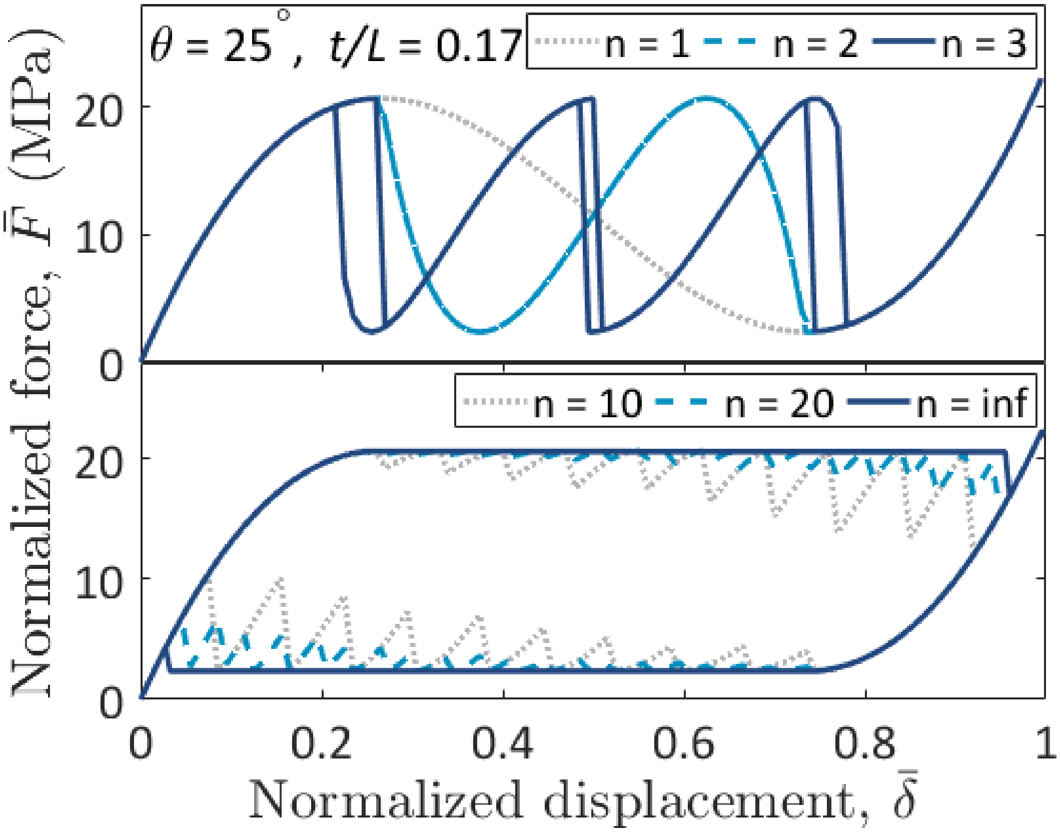

Figure 5-7: Effect of *n* on the stress-strain response for a given unit geometry ($\theta = 25°$, *t/L* = 0.17).

Taking into consideration the work energy imposed to the system, energy dissipation efficiency can be quantified by the loss factor, $\eta = \bar{D}/\pi\bar{U}_{max}$, where $\bar{D}$ is the dissipated energy per loading-unloading cycle (area enclosed by the $\bar{F} - \bar{\delta}$ curve), $\bar{U}_{max}$ is the strain energy at $\Delta_{max}$, and $\pi$ is used instead of $2\pi$ since only the positive stress-strain cycle is considered in this case (because the cyclic integral extends only over a half cycle.) The loss factor for material systems with five different unit beam geometries are presented as a function of *n* in Figure 5-8. The effect of system architecture on the stress-strain response of the structures can also be observed by the $\eta$-$n$ curves. The results show that no energy dissipation occurs, and $\eta$ equals to zero, when *n* is less than three (i.e., grey region in Figure 5-8). As *n* increases beyond three $\eta$ has a dramatic growth with increasing *n* and keeps rising towards a plateau. When *n* exceeds one-hundred $\eta$ stabilizes at a plateau value based on the unit geometry and becomes independent of *n*. This plateau is reached as the loading and unloading paths in the stress-strain response of the multi-unit material structure become bounded by two horizontal lines at the critical snap-buckling stresses, leading to the maximum hysteresis area. From the $\eta$-*n* diagram, we can see that once the number of units reaches a 'saturation' point the optimal energy dissipating performance of the proposed material structures is solely based on the beam unit geometry. Therefore, properties of the proposed material systems at their optimal condition for a given unit geometry can be calculated.

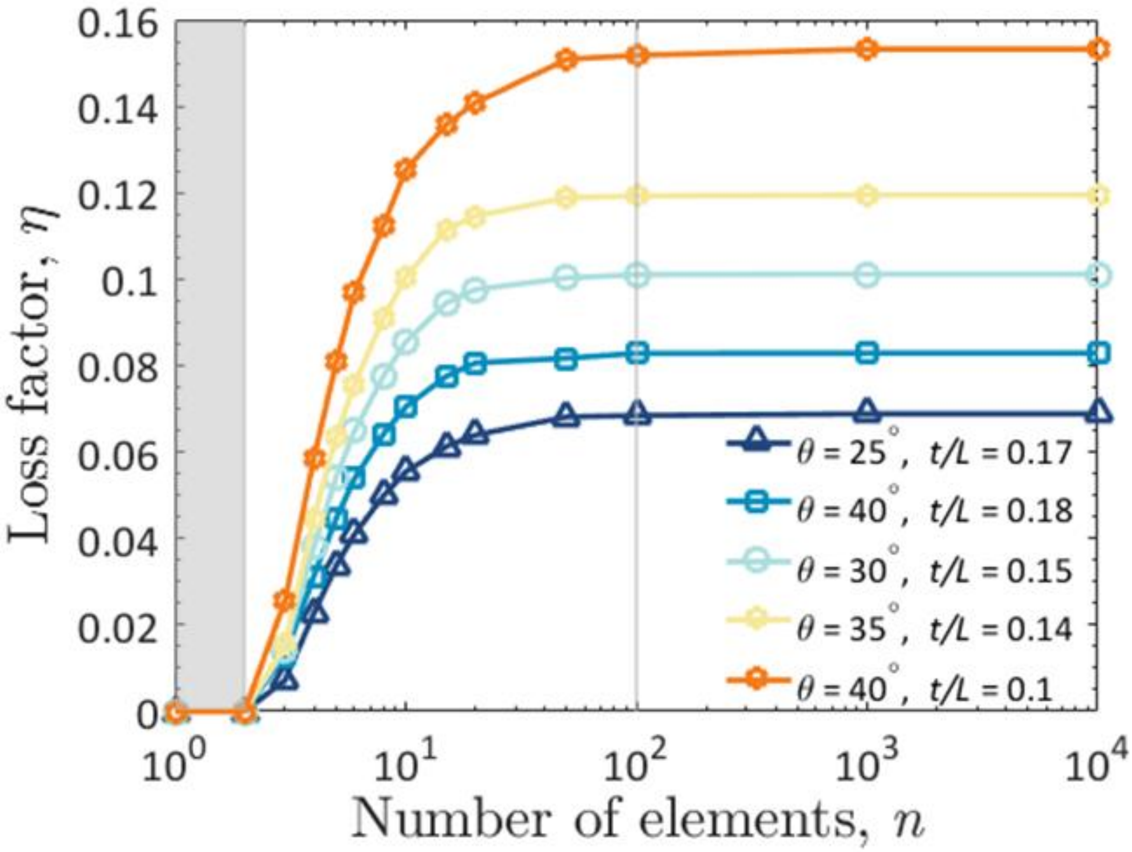

Figure 5-8: Effect of the unit geometry on the energy dissipation efficiency (loss factor) for five unit beams for $\theta$ = (25°, 40°, 30°, 35°, 40°) and $t/L$ = (0.17, 0.18,0.15,0.14,0.1).

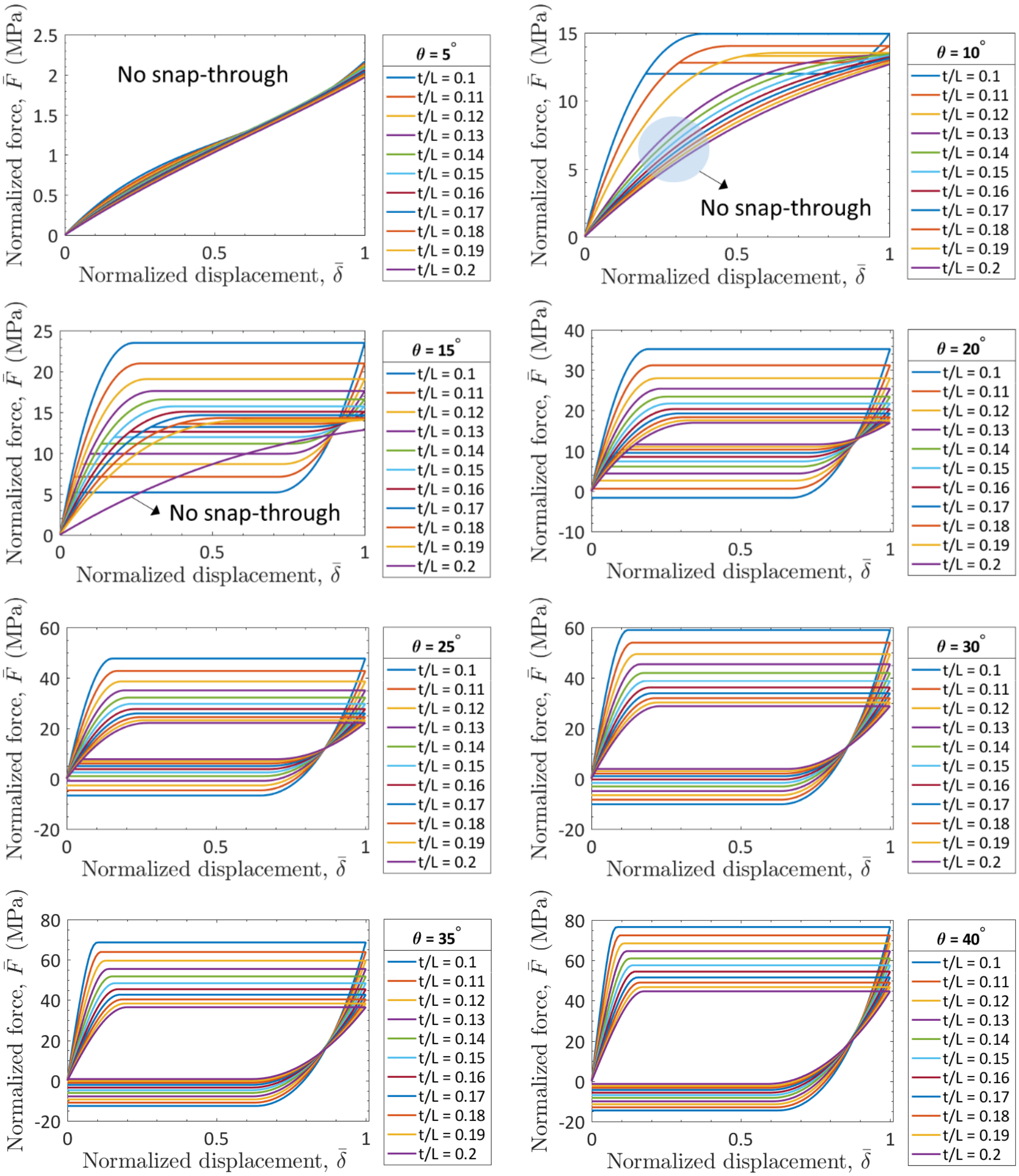

Figure 5-9: Stress-strain response of structures at their optimal performance ($n$ = inf) with a given unit geometry for different values of $\theta$ and $t/L$.

Figure 5-9 (cont'd)

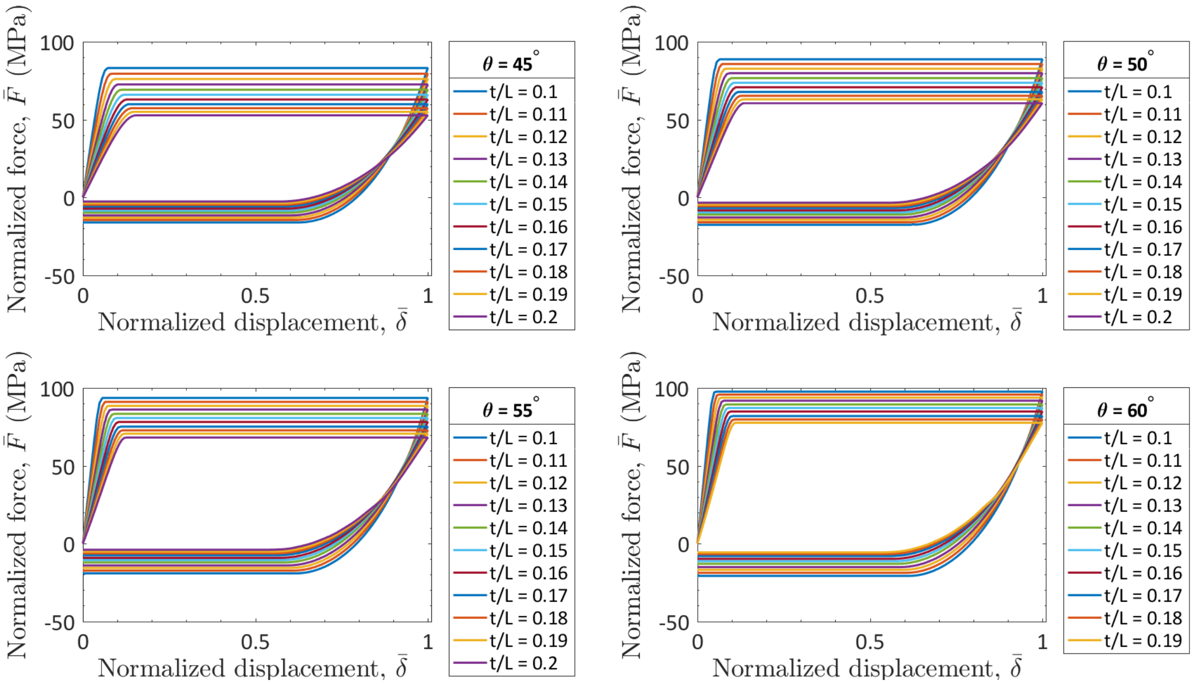

## 5.4 Parametric study

A parametric study was conducted to explore the effect of unit geometry on the structures' energy dissipation properties at their optimal performance. Stress-strain responses for single beam element within the given range of $\theta$ and *t/L*, for a total of 132 combinations, were obtained from numerical simulations and post-processed (see Figure 5-9). Under the assumption of optimal performance, that is *n* = infinite, the response curve is defined as the two stable equilibrium paths and the two flat horizontal paths at the structures' critical stress limits. Thus, the maximum and minimum critical snap-through points of a curve are searched. If the limit points exist then the optimal response curve is defined by the two initial stable equilibrium paths and the two flat horizontal paths connecting the limit point to the closest equilibrium path with an enclosed hysteresis area, and the maximum energy dissipation can be calculated. If there is no limit points on the curve then a snap-though response does not occur and there is no energy dissipation. The simulation was terminated if a self-contact condition was detected.

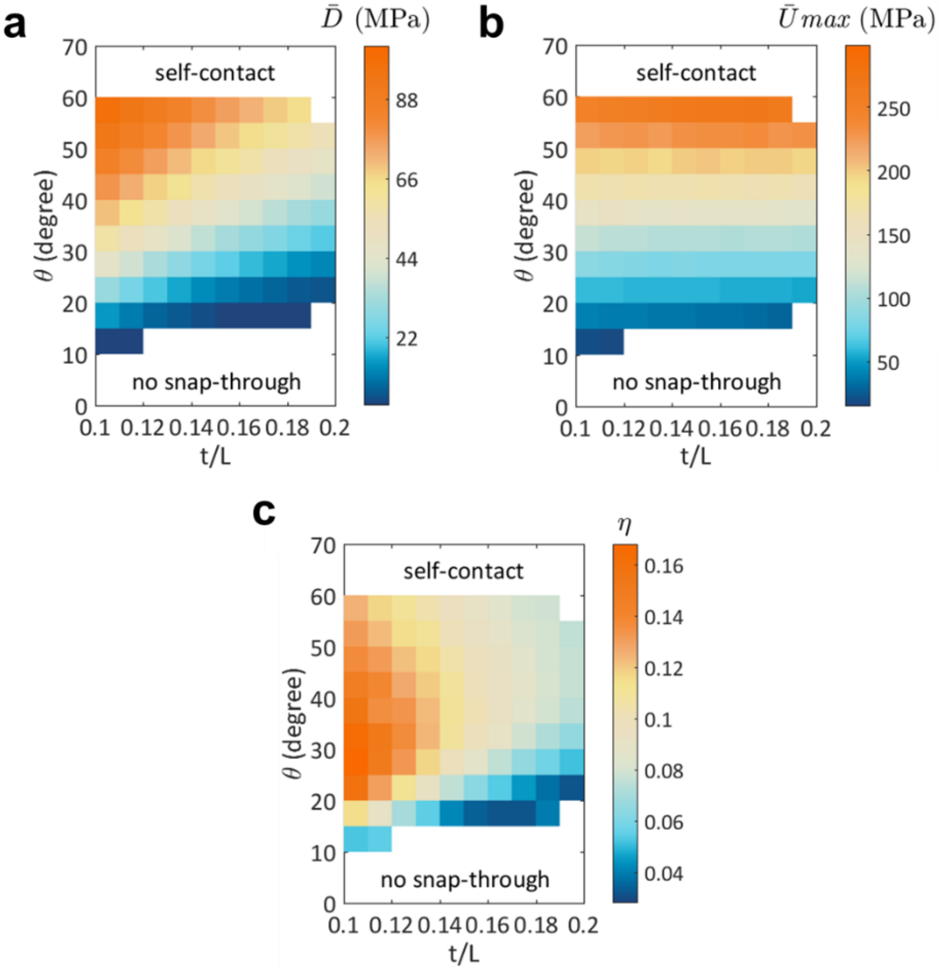

Figure 5-10: Response map of the energy properties in the proposed structures at their optimal performance (*n* = infinite) with different combination of $\theta$ and *t/L*. a). Normalized dissipated energy $\overline{D}$, b). Normalized maximum strain energy $\overline{U}_{max}$, and c). Loss factor $\eta$.

A response map, shown in Figure 5-10, that covers all the different combination of $\theta$ and *t/L* was created to evaluate the geometric effect of the unit element on the energy dissipation properties of the proposed structures at their optimal performance. The response map covers a wide range of unit geometries through combinations of $\theta$ and *t/L*, and the resulting properties are shown in terms of normalized dissipated energy $\overline{D}$, normalized maximum strain energy $\overline{U}_{max}$, and loss factor $\eta$.

The raw data used to generate this map can be found in Table 5-1, Table 5-2, and Table 5-3 below. A beam element experiences no snap-through instability when the value of $\theta$ is too low (i.e., the beam is close to perpendicular to the applied displacement direction), and self-contact due to large deformation occurs when the value of $\theta$ is too high (i.e., the beam is close to parallel to the applied displacement direction). These two conditions, indicated as white regions in Figure 5-9, define the feasible design domain of the material structures – colored area in the figure. Within the design domain, the system dissipates more energy as $\theta$ increases and $t/L$ decreases as a result of the increased absolute difference between the two critical snap-through stresses (see Figure 5-9). Also, the maximum strain energy due to the applied shear deformation increases as both $\theta$ and $t/L$ increase. This narrows the map that leads to high loss factor values in the left middle region of the domain, which gives the highest $\eta$ equal to 0.167 for a unit beam element with $\theta = 25°$ and $t/L = 0.1$.

Table 5-1: Normalized energy dissipation ($FL^3/mIh \times \sum\delta/\Delta max$) for half-cycle loading condition of structures at their optimal performance (n = inf) with a given unit geometry for different values of $\theta$ and $t/L$. The unit of normalized energy is MPa (or J/mm$^3$).

| θ° / t/L | 0.10 | 0.11 | 0.12 | 0.13 | 0.14 | 0.15 | 0.16 | 0.17 | 0.18 | 0.19 | 0.20 |
|---|---|---|---|---|---|---|---|---|---|---|---|
| 5 | NaN | NaN | NaN | NaN | NaN | NaN | NaN | NaN | NaN | NaN | NaN |
| 10 | 3.36 | 3.13 | 4.69 | NaN | NaN | NaN | NaN | NaN | NaN | NaN | NaN |
| 15 | 14.90 | 11.19 | 8.39 | 6.31 | 4.76 | 3.79 | 3.27 | 3.22 | 3.68 | 4.96 | NaN |
| 20 | 30.71 | 25.26 | 20.77 | 17.07 | 13.94 | 11.48 | 9.48 | 7.85 | 6.55 | 5.53 | 4.73 |
| 25 | 45.80 | 39.59 | 34.21 | 29.58 | 25.47 | 22.08 | 19.20 | 16.71 | 14.64 | 12.88 | 11.36 |
| 30 | 58.73 | 52.47 | 46.81 | 41.74 | 37.09 | 33.15 | 29.71 | 26.63 | 24.03 | 21.78 | 19.77 |
| 35 | 69.47 | 63.43 | 57.90 | 52.77 | 47.85 | 43.65 | 39.88 | 36.38 | 33.44 | 30.85 | 28.45 |
| 40 | 78.33 | 72.74 | 67.46 | 62.43 | 57.49 | 53.17 | 49.25 | 45.46 | 42.30 | 39.46 | 36.74 |
| 45 | 85.81 | 80.56 | 75.66 | 70.83 | 65.95 | 61.68 | 57.70 | 53.67 | 50.41 | 47.45 | 44.48 |
| 50 | 92.23 | 87.36 | 82.69 | 78.28 | 73.42 | 69.21 | 65.27 | 61.13 | 57.82 | 54.78 | 51.61 |
| 55 | 97.84 | 93.30 | 88.90 | 84.78 | 80.07 | 76.06 | 72.25 | 67.99 | 64.66 | 61.60 | 58.27 |
| 60 | 102.80 | 98.66 | 94.64 | 90.70 | 86.09 | 82.23 | 78.55 | 74.19 | 70.89 | 67.82 | NaN |
| 65 | NaN | NaN | NaN | NaN | NaN | NaN | NaN | NaN | NaN | NaN | NaN |
| 70 | NaN | NaN | NaN | NaN | NaN | NaN | NaN | NaN | NaN | NaN | NaN |

Table 5-2: Normalized maximum strain energy ($UL^3/mnIh$) for half-cycle loading condition of structures at their optimal performance ($n$ = inf) with a given unit geometry for different values of $\theta$ and $t/L$. The unit of normalized energy is MPa (or J/mm$^3$).

| θ° / t/L | 0.1 | 0.1 | 0.1 | 0.1 | 0.1 | 0.2 | 0.2 | 0.2 | 0.2 | 0.2 | 0.2 |
|---|---|---|---|---|---|---|---|---|---|---|---|
| 5 | NaN | NaN | NaN | NaN | NaN | NaN | NaN | NaN | NaN | NaN | NaN |
| 10 | 20.4 | 18.3 | 15.0 | NaN | NaN | NaN | NaN | NaN | NaN | NaN | NaN |
| 15 | 41.2 | 39.4 | 37.9 | 36.6 | 36.1 | 34.9 | 32.9 | 31.8 | 29.4 | 26.4 | NaN |
| 20 | 61.4 | 61.5 | 59.3 | 58.5 | 58.7 | 57.2 | 56.6 | 56.1 | 55.6 | 54.5 | 53.7 |
| 25 | 86.7 | 84.1 | 82.0 | 80.1 | 82.7 | 81.1 | 81.1 | 80.7 | 79.5 | 79.5 | 78.9 |
| 30 | 113.8 | 109.5 | 108.6 | 107.8 | 107.7 | 107.0 | 104.4 | 107.0 | 106.4 | 105.8 | 105.8 |
| 35 | 142.2 | 149.2 | 138.2 | 136.4 | 138.3 | 136.7 | 135.2 | 134.9 | 133.4 | 132.1 | 133.7 |
| 40 | 169.3 | 166.5 | 168.9 | 166.1 | 167.3 | 168.9 | 166.2 | 164.9 | 165.9 | 163.3 | 164.6 |
| 45 | 198.8 | 195.2 | 197.9 | 194.1 | 200.3 | 201.7 | 197.8 | 199.9 | 200.6 | 196.7 | 197.4 |
| 50 | 223.4 | 226.9 | 229.7 | 225.0 | 231.2 | 232.6 | 233.7 | 235.4 | 230.1 | 230.6 | 230.9 |
| 55 | 249.4 | 253.3 | 256.4 | 259.0 | 265.2 | 266.5 | 267.4 | 269.0 | 262.6 | 263.0 | 263.1 |
| 60 | 287.1 | 281.3 | 284.7 | 287.5 | 294.1 | 295.5 | 296.5 | 298.1 | 298.6 | 298.9 | NaN |
| 65 | NaN | NaN | NaN | NaN | NaN | NaN | NaN | NaN | NaN | NaN | NaN |
| 70 | NaN | NaN | NaN | NaN | NaN | NaN | NaN | NaN | NaN | NaN | NaN |

Table 5-3: Loss factor ($\eta = \bar{D}/\pi\bar{U}_{max}$) for structures at their optimal performance ($n$ = inf) with a given unit geometry for different values of $\theta$ and $t/L$.

| θ° / t/L | 0.10 | 0.11 | 0.12 | 0.13 | 0.14 | 0.15 | 0.16 | 0.17 | 0.18 | 0.19 | 0.20 |
|---|---|---|---|---|---|---|---|---|---|---|---|
| 5 | NaN | NaN | NaN | NaN | NaN | NaN | NaN | NaN | NaN | NaN | NaN |
| 10 | 0.05 | 0.05 | 0.10 | NaN | NaN | NaN | NaN | NaN | NaN | NaN | NaN |
| 15 | 0.12 | 0.09 | 0.07 | 0.05 | 0.04 | 0.03 | 0.03 | 0.03 | 0.04 | 0.06 | NaN |
| 20 | 0.16 | 0.13 | 0.11 | 0.09 | 0.08 | 0.06 | 0.05 | 0.04 | 0.04 | 0.03 | 0.03 |
| 25 | 0.17 | 0.15 | 0.13 | 0.12 | 0.10 | 0.09 | 0.08 | 0.07 | 0.06 | 0.05 | 0.05 |
| 30 | 0.16 | 0.15 | 0.14 | 0.12 | 0.11 | 0.10 | 0.09 | 0.08 | 0.07 | 0.07 | 0.06 |
| 35 | 0.16 | 0.14 | 0.13 | 0.12 | 0.11 | 0.10 | 0.09 | 0.09 | 0.08 | 0.07 | 0.07 |
| 40 | 0.15 | 0.14 | 0.13 | 0.12 | 0.11 | 0.10 | 0.09 | 0.09 | 0.08 | 0.08 | 0.07 |
| 45 | 0.14 | 0.13 | 0.12 | 0.12 | 0.10 | 0.10 | 0.09 | 0.09 | 0.08 | 0.08 | 0.07 |
| 50 | 0.13 | 0.12 | 0.11 | 0.11 | 0.10 | 0.09 | 0.09 | 0.08 | 0.08 | 0.08 | 0.07 |
| 55 | 0.12 | 0.12 | 0.11 | 0.10 | 0.10 | 0.09 | 0.09 | 0.08 | 0.08 | 0.07 | 0.07 |
| 60 | 0.11 | 0.11 | 0.11 | 0.10 | 0.09 | 0.09 | 0.08 | 0.08 | 0.08 | 0.07 | NaN |
| 65 | NaN | NaN | NaN | NaN | NaN | NaN | NaN | NaN | NaN | NaN | NaN |
| 70 | NaN | NaN | NaN | NaN | NaN | NaN | NaN | NaN | NaN | NaN | NaN |

## 5.5 Conclusions

This chapter presented a new class of 3D printed architected materials with the ability to tailor shear response with controllable energy dissipation. This was demonstrated by combining experiments, simulations, and analyses. The proposed materials offer recoverable and rate-independent response under cyclic shear deformations by utilizing the unique response of elastic instabilities in their microstructure. Design of the material's periodic architecture allows independent control of the critical stress limit and the energy dissipation properties; and permits the material structures to be functional under both half- and full-cycle in-plane shear deformations. The amount of dissipated energy in these materials depends solely on the microstructural geometry once the number of unit elements reach saturation, and their response is highly predictable. These mechanical metamaterial may find applications in mechanical engineering for protective equipment and packaging, or civil systems for infrastructure safety under a variety of shear loading conditions.

# Chapter 6

# CONCLUSIONS

## 6.1 General remarks

Energy transduction in mechanical systems by harnessing elastic instabilities was demonstrated in this dissertation by addressing two challenges: (1) harvesting electric energy from low frequency quasi-static mechanical deformations, and (2) dissipating energy in materials subject to cyclic shear deformations in a recoverable and rate-independent manner. Two novel concepts that leveraged the phenomena of multiple elastic instabilities in structural systems were presented to address each of the noted challenges. Each structural system was systematically investigated using 3D polymer-printing prototyping, theoretical analyses, numerical simulations, and experiments.

In the energy harvesting concept, the strain energy accumulated in axially compressed bilaterally constrained columns under quasi-static deformations was released through multiple buckling instabilities in their elastic postbuckling response. The strain energy accumulated in the structures was transformed into usable electric energy by coupling this response with the piezoelectric effect of mounted transducers. This concept overcomes the disadvantage of poor performance of piezoelectric materials under low frequency excitations and it was shown to be effective in harvesting energy directly from low frequency quasi-static deformation sources. It was demonstrated that the resulting energy generation can adequately provide power supply for low-power budget devices, such as self-powered structural health monitoring sensors or *in vivo* bio-MEMS.

The proposed energy harvesting devices were experimentally validated through 3D polymer-printed strip/ prototypes outfitted with commercial piezoelectric materials. The prototypes were tested under quasi-static loading and unloading. Results from numerical and analytical models were in good agreement with the experiments, and were the models were further used to predict the postbuckling behavior of the considered structures. The experimental results showed that the non-prismatic strip/column design permits controlling the buckling location at each buckling mode transition thus leading to enhanced energy generation compared to prismatic designs, which do now allow controlling the localized buckling locations. The proposed energy-harvesting devices incorporating non-prismatic cross-section were shown to generate a peak power of 1.33 $\mu$W/cm$^2$, which is considerably higher than other current quasi-static piezoelectric energy harvesting strategies.

The energy-dissipative material concept, which proposes the use of elastic inclined beams in the microstructure of the material architecture, was shown to manage the strain energy generated due to cyclic shear deformations and dissipate it through sequential snap-through instabilities. The periodic arrangement of the elastic inclined beams permits the generation of a 'twinkling' phenomenon under repeated in-plane deformations, which results in rate-independent energy dissipations and a fully recoverable response. This concept addresses the need of high energy-dissipative materials under shear loads, and overcomes the disadvantages of permanent deformations and rate dependency in traditional energy dissipating mechanisms and materials. The developed material design concept can be deployed in diverse applications such as personal protection, packaging, and civil structures.

Prototypes of the energy-dissipating material concept were experimentally tested at different loading rates showing controllable, repeatable, and rate-independent response under both half- and full-cycle in-plane shear deformations. The critical stress limit and the energy dissipation properties can be designed through the material's periodic architecture and can be predicted analytically. The system reaches optimal energy dissipation performance for a high number of unit elements, reaching a saturation point that was found to be one-hundred for the geometry and material evaluated in this study. The dissipated energy then depends solely on the microstructural geometry, predicted numerically in this work, with the highest loss factor $\eta$ for the studied system found to be equal to 0.167.

This dissertation leveraged the phenomena of internal energy exchange within a structure or solid due to the presence of multiple elastic instabilities, as well as multi-physics coupling effects, to convey strain energy accumulated in a system into predefined responses or to perform desirable functions. The presented investigation led to improved understanding on the methods to control elastic instabilities in slender structures for desirable purposes. The novel structural concepts developed in this research, along with the demonstrated analytical and numerical methods, enable and push forward the design of adaptive and smart structural systems.

## 6.2 Remaining questions

Several questions arose over the course of this study that are outside the scope of this dissertation but warrant further investigation. The most salient ones are presented here.

The behavior of the structural design concepts was demonstrated using 3D printed polymer prototypes without considering the operating environment for specific applications. Effects from the operating environment on the behavior of the proposed systems needs to be studied for appropriate base-material selection and manufacturing methods. Important effects to consider are temperature, moisture and surrounding media interaction/exposure; as well as long-term behavior due to material degradation and fatigue. Design optimization for optimal material/structural performance can also be implemented accordingly.

The architected material concept was demonstrated with table-top scale prototypes with only a few unit elements, rather than the high number of units required for their optimal performance. In addition, questions and challenges remain regarding scale-down and scale-up of the concept in order to deploy it for targeted applications. For example, for use in the inner layer of a helmet the architecture of the material needs to be fabricated at the microscale; or for use as connector between building shear walls, the materials need to be fabricated in large scales. Thus, effective fabrication methods need to be further considered for the large number of complex architecture design under different size scale requirements.

## 6.3 Potential future research

Potential future studies that follow directly from what was investigated and discovered in this research is discussed in the following.

Fatigue test on slender columns/beams made with different materials under repeated axial/transverse loading-unloading cycles to trigger buckling/snapping instabilities should be evaluated to assess the structures' long-term behavior. Materials with a range of stiffness variations and with high-flexibility to support large elastic rotations should be selected to fabricate the samples, since the response of elastic instabilities is associated the material's ability to store and release strain energy before and after the critical limit (i.e., pre- and post- critical stiffness).

The proposed energy-dissipating architected material designs are functional under half and full cycle unidirectional in-plane shear deformation. Designs for bi-directional shear deformations can be explored to expand the material design space from two-dimensional to three-dimensional. In the current investigation, the architected material prototypes were evaluated under quasi-static loading conditions with regular loading-unloading cycles. Their responses under dynamic loading conditions with consideration of inertia effects and under irregular loading-unloading cycles (e.g., seismic induced deformations) can also be further investigated.

Only two structural systems featuring a behavior with multiple elastic instabilities were investigated in this dissertation. However, the core knowledge and analytical and numerical methods developed and used in this research also enable the exploration other slender structures with highly nonlinear structural behavior. Further, while the multi-physics coupling of mechanical instabilities with piezoelectric effects was applied in the current work, other multi-physics phenomena, such as interactions with fluids, optoelectronics, or electromagnetism, can also provide fruitful and exciting research areas to be explored. Looking forward, the ample opportunities offered by elastic instabilities go well beyond the scope of this dissertation are a myriad of opportunities remain to be explored for leveraging this unique phenomena in solids for improved form and function of smart materials and adaptive structures.

# APPENDIX

# ABOUT THE AUTHOR

Suihan Liu was born in Zhengzhou, China on December 30, 1991. She attended schools in China, the U.K., and Singapore before coming to the U.S. for her college education. She joined Michigan State University in 2011 for her undergraduate studies and received her B.S. degree in Civil Engineering (specializing in structural engineering) in 2015. She continued her studies at Michigan State University to pursue a Ph.D. degree in Engineering Mechanics from the Department of Mechanical Engineering.

## RELEVANT PUBLICATIONS AND PRESENTATIONS

### Publications in refereed journal:

1. **Liu, S.** and Burgueño, R. "Controlled elastic postbuckling of bilaterally constrained non-prismatic columns: application to enhanced quasi-static energy harvesters," *Smart Materials and Structures* (2016). 25(12): p. 125010.
2. **Liu, S.**, Azad, A. I., & Burgueño, R. "Energy harvesting from quasi-static deformations via bilaterally constrained strips," *Journal of Intelligent Material Systems and Structures* (2018). 29(18): p. 3572-3581.
3. **Liu, S.**, Azad, A. I., and Burgueño, R. "Architected materials for tailorable shear behavior with energy dissipation," *Extreme Mechanics Letters* (2019). 28: p. 1-7.

### Publications in conference proceeding:

1. **Liu, S.**, Hu, N., and Burgueño, R. "Postbuckling Behavior of Axially-compressed Strips with Discrete Rigid Constraints," *ASME 2015 Conference on Smart Materials, Adaptive Structures and Intelligent Systems,* Colorado Springs, USA, SMASIS2015-9050, September 2015.
2. **Liu, S.**, and Burgueño, R. "Elastic Postbuckling Response of Bilaterally Constrained Non-Prismatic Columns," *SEMC 2016, the Sixth International Conference on Structural Engineering, Mechanics and Computation*, Cape Town, South Africa, SEMC2016-353, September 2016.
3. Hu, N., **Liu, S.**, and Burgueño, R. "Controlled Elastic Instabilities in Cylindrical Shells for Energy Harvesting Devices," *SEMC 2016, the Sixth International Conference on*

*Structural Engineering, Mechanics and Computation*, Cape Town, South Africa, SEMC2016-352, September 2016.

4. **Liu, S.**, and Burgueño, R. "Self-Sensing Solid Materials via Delamination Buckling," *ASME 2017 Conference on Smart Materials, Adaptive Structures and Intelligent Systems*, Snowbird, Utah, SMASIS2017-3984, September 2017.
5. Guo, J., **Liu, S.**, and Burgueño, R. "Tailoring the Elastic Postbuckling Response of Thin-Walled Cylindrical Shells for Applications in Mechanical Devices and Adaptive Structures," *ASME 2017 Conference on Smart Materials, Adaptive Structures and Intelligent Systems*, Snowbird, Utah, SMASIS2017-3967, September 2017.

**Public presentations:**

1. Contributed talk on "Postbuckling Behavior of Axially-compressed Strips with Discrete Rigid Constraints" at *ASME Conference on Smart Materials, Adaptive Structures and Intelligent Systems*, Colorado Springs, CO, USA (September 2015).
2. Poster presentation on "Elastic Postbuckling Response of Bilaterally Constrained Non-Prismatic Columns" at *Engineering Graduate Research Symposium*, Michigan State University, East Lansing, MI, USA (March 2016).
3. Contributed talk on "Controlled Elastic Instabilities in Cylindrical Shells for Energy Harvesting Devices" at the *Sixth International Conference on Structural Engineering, Mechanics and Computation*, Cape Town, South Africa (September 2016).
4. Contributed talk on "Elastic Postbuckling Response of Bilaterally Constrained Non-Prismatic Columns" at the *Sixth International Conference on Structural Engineering, Mechanics and Computation*, Cape Town, South Africa (September 2016).

5. Poster presentation on “Controlled Elastic Postbuckling Response of Bilaterally Constrained Non-Prismatic Columns: Application to Enhanced Quasi-static Energy Harvesters” at *Engineering Graduate Research Symposium*, Michigan State University, East Lansing, MI, USA (March 2017).
6. Contributed talk on “Self-Sensing Solid Materials via Delamination Buckling” at the *54th Society of Engineering Science Technical Meeting*, Boston, USA (August 2017).
7. Contributed talk on “Tailoring the Elastic Postbuckling Response of Thin-Walled Cylindrical Shells for Applications in Mechanical Devices and Adaptive Structures” at *ASME Conference on Smart Materials, Adaptive Structures and Intelligent Systems*, Snowbird, UT, USA (September 2017).
8. Invited talk on “Harnessing Elastic Instabilities for “Smart” Engineering Applications” at the *GE Research Innovate Event*, GE Global Research Center, Niskayuna, NY, USA (April 2019).

# REFERENCES

# REFERENCES

[1] Y. Forterre, J. M. Skotheim, J. Dumais, and L. Mahadevan, "How the Venus flytrap snaps," *Nature,* vol. 433, p. 421, 2005.

[2] K. Son, J. S. Guasto, and R. Stocker, "Bacteria can exploit a flagellar buckling instability to change direction," *Nature physics,* vol. 9, p. 494, 2013.

[3] J. Xiao and X. Chen, "Buckling morphology of an elastic beam between two parallel lateral constraints: implication for a snake crawling between walls," *Journal of The Royal Society Interface,* vol. 10, p. 20130399, 2013.

[4] L. Clark, W. Whalley, and P. Barraclough, "How do roots penetrate strong soil?," in *Roots: The Dynamic Interface Between Plants and the Earth,* ed: Springer, 2003, pp. 93-104.

[5] J. L. Silverberg, R. D. Noar, M. S. Packer, M. J. Harrison, C. L. Henley, I. Cohen, *et al.*, "3D imaging and mechanical modeling of helical buckling in Medicago truncatula plant roots," *Proceedings of the National Academy of Sciences,* vol. 109, pp. 16794-16799, 2012.

[6] E. Torricelli, "Opera geometrica," ed: Florentiae: typis Amatoris Masse & Laurentii de Landis, 1644.

[7] L. Euler, "Methodus inveniendi lineas curvas maximi minimive proprietate gaudentes, Lausanne," *Leonhardi Euleri Opera Omnia,* vol. 24, 1744.

[8] J. Lagrange, "Mécanique Analytique," ed: Paris, 1788.

[9] G. L. Dirichlet, "Über die Stabilität des Gleichgewichts," *Journal für die reine und angewandte Mathematik,* vol. 32, pp. 85-88, 1846.

[10] H. Poincaré, "Sur l'équilibre d'une masse fluide animée d'un mouvement de rotation," *Acta mathematica,* vol. 7, pp. 259-380, 1885.

[11] A. M. Lyapunov, "The general problem of motion stability," *Annals of Mathematics Studies,* vol. 17, 1892.

[12] J. M. T. Thompson and G. W. Hunt, *Elastic instability phenomena* vol. 2: Wiley Chichester etc., 1984.

[13] J. M. T. Thompson and G. W. Hunt, *A general theory of elastic stability*: J. Wiley London, 1973.

[14] P. B. C. Bažant, Luigi, *Stability of structures: elastic, inelastic, fracture and damage theories*: World Scientific, 2010.

[15] L. Euler, "Sur la force des colonnes," *Memoires de L'Academie des Sciences et Belles-Lettres,* vol. 13, pp. 252-282, 1759.

[16] L. Euler, "Determinatio onerum, quae columnae gestare valent," *Acta Academiae Scientiarum Imperialis Petropolitanae,* pp. 121-145, 1780.

[17] S. P. Timoshenko and J. M. Gere, "Theory of elastic stability," ed: McGraw-Hill, New York, 1961.

[18] F. Engesser, *Die Zusatzkräfte und Nebenspannungen eiserner Fachwerkbrücken: Eine systematische Darstellung der verschiedenen Arten, ihrer Grösse und ihres Einflusses auf die konstruktive Gestaltung der Brücken*: J. Springer, 1892.

[19] R. Narayanan, *Shell structures: stability and strength*: Elsevier London; New York, 1985.

[20] A. Kaplan, "Buckling of spherical shells(computer capabilities and experimental techniques)," *Thin-shell structures: Theory, experiment, and design,* pp. 247-288, 1974.

[21] D. Muggeridge and R. Tennyson, "Buckling of axisymmetric imperfect circular cylindrical shells underaxial compression," *AIAA Journal,* vol. 7, pp. 2127-2131, 1969.

[22] W. T. Koiter, "On the nonlinear theory of thin elastic shells," *Proc. Koninkl. Ned. Akad. van Wetenschappen, Series B,* vol. 69, pp. 1-54, 1966.

[23] D. O. Brush and B. O. Almroth, *Buckling of bars, plates, and shells* vol. 6: McGraw-Hill New York, 1975.

[24] A. d. S. Vol′mir, "Stability of deformable systems," FOREIGN TECHNOLOGY DIV WRIGHT-PATTERSON AFB OHIO1970.

[25] R. Mises and J. Ratzersdorfer, "Die Knicksicherheit von Fachwerken," *ZAMM ‐ Journal of Applied Mathematics and Mechanics/Zeitschrift für Angewandte Mathematik und Mechanik,* vol. 5, pp. 218-235, 1925.

[26] J. Zhao, J. Jia, X. He, and H. Wang, "Post-buckling and snap-through behavior of inclined slender beams," *Journal of Applied Mechanics,* vol. 75, p. 041020, 2008.

[27] S. Shan, S. H. Kang, J. R. Raney, P. Wang, L. Fang, F. Candido*, et al.,* "Multistable architected materials for trapping elastic strain energy," *Advanced Materials,* vol. 27, pp. 4296-4301, 2015.

[28] M. Vangbo, "An analytical analysis of a compressed bistable buckled beam," *Sensors and Actuators A: Physical,* vol. 69, pp. 212-216, 1998.

[29] B. Camescasse, "Actionnements statique et dynamique d'un mécanisme bistable: aspects modélisation, conception et expérimental," Paris 6, 2013.

[30] I. Z. Pane and T. Asano, "Investigation on bistability and fabrication of bistable prestressed curved beam," *Japanese Journal of Applied Physics,* vol. 47, p. 5291, 2008.

[31] B. Camescasse, A. Fernandes, and J. Pouget, "Bistable buckled beam and force actuation: Experimental validations," *International Journal of Solids and Structures,* vol. 51, pp. 1750-1757, 2014.

[32] B. Camescasse, A. Fernandes, and J. Pouget, "Bistable buckled beam: Elastica modeling and analysis of static actuation," *International Journal of Solids and Structures,* vol. 50, pp. 2881-2893, 2013.

[33] S. Park and D. Hah, "Pre-shaped buckled-beam actuators: theory and experiments," *Sensors and Actuators A: Physical,* vol. 148, pp. 186-192, 2008.

[34] J. Qiu, J. H. Lang, and A. H. Slocum, "A curved-beam bistable mechanism," *Journal of microelectromechanical systems,* vol. 13, pp. 137-146, 2004.

[35] M. D. Williams, F. van Keulen, and M. Sheplak, "Modeling of initially curved beam structures for design of multistable MEMS," *Journal of Applied Mechanics,* vol. 79, p. 011006, 2012.

[36] P. Z. C. Bažant, Luigi, *Stability of structures: elastic, inelastic, fracture and damage theories*: World Scientific, 2010.

[37] S. Timoshenko, "Buckling of curved bars with small curvature," *Journal of Applied Mechanics (ASME),* vol. 2, p. 17, 1935.

[38] K. Marguerre, "Die. Durchschlagskraft eines schwach gekrummten Balken," *Sitz. Berlin Math. Ges,* vol. 37, pp. 92-108, 1938.

[39] C. Biezeno, "Das Durchschlagen eines schwach gekrümmten Stabes," *ZAMM ‐ Journal of Applied Mathematics and Mechanics/Zeitschrift für Angewandte Mathematik und Mechanik,* vol. 18, pp. 21-30, 1938.

[40] Y.-C. Fung and A. Kaplan, "Buckling of low arches or curved beams of small curvature," 1952.

[41] R. H. Plaut, "Snap-through of arches and buckled beams under unilateral displacement control," *International Journal of Solids and Structures,* vol. 63, pp. 109-113, 2015.

[42] Y. Chandra, I. Stanciulescu, L. N. Virgin, T. G. Eason, and S. M. Spottswood, "A numerical investigation of snap-through in a shallow arch-like model," *Journal of Sound and Vibration,* vol. 332, pp. 2532-2548, 2013.

[43] J.-S. Chen and S.-Y. Hung, "Exact snapping loads of a buckled beam under a midpoint force," *Applied Mathematical Modelling,* vol. 36, pp. 1776-1782, 2012.

[44] S. Timoshenko, "Buckling of flat curved bars and slightly curved plates," *ASME J. Appl. Mech*, vol. 2, pp. A17-A20, 1935.

[45] Y. S. Oh and S. Kota, "Synthesis of multistable equilibrium compliant mechanisms using combinations of bistable mechanisms," *Journal of Mechanical Design*, vol. 131, p. 021002, 2009.

[46] J. Beharic, T. Lucas, and C. Harnett, "Analysis of a Compressed Bistable Buckled Beam on a Flexible Support," *Journal of Applied Mechanics*, vol. 81, p. 081011, 2014.

[47] P. Cazottes, A. Fernandes, J. Pouget, and M. Hafez, "Bistable buckled beam: modeling of actuating force and experimental validations," *Journal of Mechanical Design*, vol. 131, p. 101001, 2009.

[48] S. Palathingal and G. Ananthasuresh, "Design of bistable arches by determining critical points in the force-displacement characteristic," *Mechanism and Machine Theory*, vol. 117, pp. 175-188, 2017.

[49] K. Seffen and S. Pellegrino, "Deployment dynamics of tape springs," in *Proceedings of the Royal Society of London A: Mathematical, Physical and Engineering Sciences*, 1999, pp. 1003-1048.

[50] K. A. Seffen and S. D. Guest, "Prestressed morphing bistable and neutrally stable shells," *Journal of Applied Mechanics*, vol. 78, p. 011002, 2011.

[51] E. Kebadze, S. Guest, and S. Pellegrino, "Bistable prestressed shell structures," *International Journal of Solids and Structures*, vol. 41, pp. 2801-2820, 2004.

[52] S. Guest and S. Pellegrino, "Analytical models for bistable cylindrical shells," in *Proceedings of the Royal Society of London A: Mathematical, Physical and Engineering Sciences*, 2006, pp. 839-854.

[53] W. Wittrick, W. Wittrick, D. Myers, and W. Blunden, "Stability of a bimetallic disk," *The Quarterly Journal of Mechanics and Applied Mathematics*, vol. 6, pp. 15-31, 1953.

[54] M. W. Hyer, "The room-temperature shapes of four-layer unsymmetric cross-ply laminates," *Journal of Composite Materials*, vol. 16, pp. 318-340, 1982.

[55] M. W. Hyer, "Some observations on the cured shape of thin unsymmetric laminates," *Journal of Composite Materials*, vol. 15, pp. 175-194, 1981.

[56] S. R. White and H. Hahn, "Process modeling of composite materials: residual stress development during cure. Part II. Experimental validation," *Journal of composite materials*, vol. 26, pp. 2423-2453, 1992.

[57] H. Li, F. Dai, P. Weaver, and S. Du, "Bistable hybrid symmetric laminates," *Composite Structures*, vol. 116, pp. 782-792, 2014.

[58] S. Daynes, C. Diaconu, K. Potter, and P. Weaver, "Bistable prestressed symmetric laminates," *Journal of Composite Materials,* vol. 44, pp. 1119-1137, 2010.

[59] W. Hufenbach, M. Gude, and L. Kroll, "Design of multistable composites for application in adaptive structures," *Composites science and technology,* vol. 62, pp. 2201-2207, 2002.

[60] A. E. H. Love, *A treatise on the mathematical theory of elasticity*: Cambridge university press, 2013.

[61] C. R. Calladine, *Theory of shell structures*: Cambridge University Press, 1989.

[62] Z. Chen, Q. Guo, C. Majidi, W. Chen, D. J. Srolovitz, and M. P. Haataja, "Nonlinear geometric effects in mechanical bistable morphing structures," *Physical review letters,* vol. 109, p. 114302, 2012.

[63] B. H. Coburn, A. Pirrera, P. M. Weaver, and S. Vidoli, "Tristability of an orthotropic doubly curved shell," *Composite Structures,* vol. 96, pp. 446-454, 2013.

[64] F. Dai, H. Li, and S. Du, "Cured shape and snap-through of bistable twisting hybrid [0/90/metal] T laminates," *Composites Science and Technology,* vol. 86, pp. 76-81, 2013.

[65] J.-G. Lee, J. Ryu, H. Lee, and M. Cho, "Saddle-shaped, bistable morphing panel with shape memory alloy spring actuator," *Smart Materials and Structures,* vol. 23, p. 074013, 2014.

[66] K. Seffen, "'Morphing'bistable orthotropic elliptical shallow shells," in *Proceedings of the Royal Society of London A: Mathematical, Physical and Engineering Sciences,* 2007, pp. 67-83.

[67] E. H. Mansfield, "Bending, buckling and curling of a heated elliptical plate," in *Proceedings of the Royal Society of London A: Mathematical, Physical and Engineering Sciences,* 1965, pp. 396-417.

[68] W. Hamouche, C. Maurini, S. Vidoli, and A. Vincenti, "Multi-parameter actuation of a neutrally stable shell: a flexible gear-less motor," in *Proc. R. Soc. A,* 2017, p. 20170364.

[69] R. Burgueño, N. Hu, A. Heeringa, and N. Lajnef, "Tailoring the elastic postbuckling response of thin-walled cylindrical composite shells under axial compression," *Thin-Walled Structures,* vol. 84, pp. 14-25, 2014.

[70] W. Jun and C. Hong, "Cured shape of unsymmetric laminates with arbitrary lay-up angles," *Journal of reinforced plastics and composites,* vol. 11, pp. 1352-1366, 1992.

[71] S. Poppinga and M. Joyeux, "Different mechanics of snap-trapping in the two closely related carnivorous plants Dionaea muscipula and Aldrovanda vesiculosa," *Physical Review E,* vol. 84, p. 041928, 2011.

[72] Q. Guo, A. K. Mehta, M. A. Grover, W. Chen, D. G. Lynn, and Z. Chen, "Shape selection and multi-stability in helical ribbons," *Applied Physics Letters,* vol. 104, p. 211901, 2014.

[73] S. Armon, H. Aharoni, M. Moshe, and E. Sharon, "Shape selection in chiral ribbons: from seed pods to supramolecular assemblies," *Soft Matter,* vol. 10, pp. 2733-2740, 2014.

[74] G. Brodland and H. Cohen, "Deflection and snapping of spherical caps," *International journal of solids and structures,* vol. 23, pp. 1341-1356, 1987.

[75] D. Shilkrut, "About the ways of stability loss by snap-through of geometrically non-linear shells (systems) and some related problems," *International journal of non-linear mechanics,* vol. 29, pp. 671-686, 1994.

[76] A. Vaziri, "Mechanics of highly deformed elastic shells," *Thin-Walled Structures,* vol. 47, pp. 692-700, 2009.

[77] A. Madhukar, D. Perlitz, M. Grigola, D. Gai, and K. J. Hsia, "Bistable characteristics of thick-walled axisymmetric domes," *International Journal of Solids and Structures,* vol. 51, pp. 2590-2597, 2014.

[78] A. Gent, "Elastic instabilities of inflated rubber shells," *Rubber chemistry and technology,* vol. 72, pp. 263-268, 1999.

[79] A. Gent, "Elastic instabilities in rubber," *International Journal of Non-Linear Mechanics,* vol. 40, pp. 165-175, 2005.

[80] N. Yamaki, *Elastic stability of circular cylindrical shells* vol. 27: Elsevier, 1984.

[81] M. Stein, "Loads and deformations of buckled rectangular plates," *NASA,* 1959.

[82] G. W. Hunt, H. Bolt, and J. M. T. Thompson, "Structural localization phenomena and the dynamical phase-space analogy," *Proc. R. Soc. Lond. A,* vol. 425, pp. 245-267, 1989.

[83] P. Everall and G. W. Hunt, "Mode jumping in the buckling of struts and plates: a comparative study," *International Journal of Non-Linear Mechanics,* vol. 35, pp. 1067-1079, 2000.

[84] H. Chai, "The post-buckling response of a bi-laterally constrained column," *Journal of the Mechanics and Physics of Solids,* vol. 46, pp. 11551161-11591181, 1998.

[85] H. Chai, "On the post-buckling behavior of bilaterally constrained plates," *International Journal of Solids and Structures,* vol. 39, pp. 2911-2926, 2002.

[86] P. M. Reis, "A perspective on the revival of structural (in) stability with novel opportunities for function: From buckliphobia to buckliphilia," *Journal of Applied Mechanics,* vol. 82, p. 111001, 2015.

[87] N. Hu and R. Burgueño, "Buckling-induced smart applications: recent advances and trends," *Smart Materials and Structures,* vol. 24, p. 063001, 2015.

[88] K. Bertoldi, "Harnessing Instabilities to Design Tunable Architected Cellular Materials," *Annual Review of Materials Research,* 2017.

[89] D. Kochmann and K. Bertoldi, "Exploiting microstructural instabilities in solids and structures: from metamaterials to structural transitions," *Applied Mechanics Reviews,* 2017.

[90] A. Crivaro, R. Sheridan, M. Frecker, T. W. Simpson, and P. Von Lockette, "Bistable compliant mechanism using magneto active elastomer actuation," *Journal of Intelligent Material Systems and Structures,* vol. 27, pp. 2049-2061, 2016.

[91] M. Schaeffer and M. Ruzzene, "Homogenization of 1D and 2D magnetoelastic lattices," *EPJ Applied Metamaterials,* vol. 2, p. 13, 2015.

[92] E. Loukaides, S. Smoukov, and K. Seffen, "Magnetic actuation and transition shapes of a bistable spherical cap," *International Journal of Smart and Nano Materials,* vol. 5, pp. 270-282, 2014.

[93] B. Seung-Ki, Y. Yong-Kyu, J. Hye-Seon, S. Soonmin, and P. Jung-Hwan, "A wireless sequentially actuated microvalve system," *Journal of Micromechanics and Microengineering,* vol. 23, p. 045006, 2013.

[94] F. Mattioni, P. M. Weaver, K. D. Potter, and M. I. Friswell, "The application of thermally induced multistable composites to morphing aircraft structures," in *Proc. SPIE*, 2008, p. 693012.

[95] J. Qiu, J. H. Lang, A. H. Slocum, and A. C. Weber, "A bulk-micromachined bistable relay with U-shaped thermal actuators," *Journal of Microelectromechanical Systems,* vol. 14, pp. 1099-1109, 2005.

[96] P. F. Giddings, H. A. Kim, A. I. Salo, and C. R. Bowen, "Modelling of piezoelectrically actuated bistable composites," *Materials Letters,* vol. 65, pp. 1261-1263, 2011.

[97] H. A. Kim, D. N. Betts, A. I. Salo, and C. R. Bowen, "Shape Memory Alloy-Piezoelectric Active Structures for Reversible Actuation of Bistable Composites (TN)," *AIAA Journal,* vol. 48, p. 1265, 2010.

[98] C. Maurini, J. Pouget, and S. Vidoli, "Distributed piezoelectric actuation of a bistable buckled beam," *European Journal of Mechanics-A/Solids,* vol. 26, pp. 837-853, 2007.

[99] S. Krylov and N. Dick, "Dynamic stability of electrostatically actuated initially curved shallow micro beams," *Continuum Mechanics and Thermodynamics,* vol. 22, pp. 445-468, 2010.

[100] S. Krylov, B. R. Ilic, D. Schreiber, S. Seretensky, and H. Craighead, "The pull-in behavior of electrostatically actuated bistable microstructures," *Journal of Micromechanics and Microengineering,* vol. 18, p. 055026, 2008.

[101] L. Medina, R. Gilat, B. Ilic, and S. Krylov, "Experimental investigation of the snap-through buckling of electrostatically actuated initially curved pre-stressed micro beams," *Sensors and Actuators A: Physical,* vol. 220, pp. 323-332, 2014.

[102] L. Medina, R. Gilat, and S. Krylov, "Bistable behavior of electrostatically actuated initially curved micro plate," *Sensors and Actuators A: Physical,* vol. 248, pp. 193-198, 2016.

[103] S. Krylov, S. Seretensky, and D. Schreiber, "Pull-in behavior and multistability of a curved microbeam actuated by a distributed electrostatic force," in *Micro Electro Mechanical Systems, 2008. MEMS 2008. IEEE 21st International Conference on,* 2008, pp. 499-502.

[104] D. Wagg, I. Bond, P. Weaver, and M. Friswell, *Adaptive structures: engineering applications*: John Wiley & Sons, 2008.

[105] J. U. Schmied, H. Le Ferrand, P. Ermanni, A. R. Studart, and A. F. Arrieta, "Programmable snapping composites with bio-inspired architecture," *Bioinspiration & Biomimetics,* vol. 12, p. 026012, 2017.

[106] X. Lachenal, S. Daynes, and P. M. Weaver, "Review of morphing concepts and materials for wind turbine blade applications," *Wind Energy,* vol. 16, pp. 283-307, 2013.

[107] Y. Cui and M. Santer, "Highly multistable composite surfaces," *Composite Structures,* vol. 124, pp. 44-54, 2015.

[108] P. Portela, P. Camanho, P. Weaver, and I. Bond, "Analysis of morphing, multi stable structures actuated by piezoelectric patches," *Computers & Structures,* vol. 86, pp. 347-356, 2008.

[109] A. Pirrera, D. Avitabile, and P. Weaver, "Bistable plates for morphing structures: a refined analytical approach with high-order polynomials," *International Journal of Solids and Structures,* vol. 47, pp. 3412-3425, 2010.

[110] C. R. Bowen, P. F. Giddings, A. I. Salo, and H. A. Kim, "Modeling and characterization of piezoelectrically actuated bistable composites," *IEEE transactions on ultrasonics, ferroelectrics, and frequency control,* vol. 58, pp. 1737-1750, 2011.

[111] S. A. Tawfik, D. S. Dancila, and E. Armanios, "Unsymmetric composite laminates morphing via piezoelectric actuators," *Composites Part A: Applied Science and Manufacturing,* vol. 42, pp. 748-756, 2011.

[112] I. K. Kuder, A. F. Arrieta, M. Rist, and P. Ermanni, "Aeroelastic response of a selectively compliant morphing aerofoil featuring integrated variable stiffness bi-stable laminates," *Journal of Intelligent Material Systems and Structures,* vol. 27, pp. 1949-1966, 2016.

[113] M.-L. Dano, M. Jean-St-Laurent, and A. Fecteau, "Morphing of bistable composite laminates using distributed piezoelectric actuators," *Smart Materials Research,* vol. 2012, 2012.

[114] C. G. Diaconu, P. M. Weaver, and F. Mattioni, "Concepts for morphing airfoil sections using bi-stable laminated composite structures," *Thin-Walled Structures,* vol. 46, pp. 689-701, 2008.

[115] M. R. Schultz, "A concept for airfoil-like active bistable twisting structures," *Journal of Intelligent Material Systems and Structures,* vol. 19, pp. 157-169, 2008.

[116] L. Falcao, A. Gomes, and A. Suleman, "Morphing wingtip devices based on multistable composites," 2009.

[117] S. Daynes, S. Nall, P. Weaver, K. Potter, P. Margaris, and P. Mellor, "Bistable composite flap for an airfoil," *Journal of Aircraft,* vol. 47, p. 334, 2010.

[118] A. F. Arrieta, I. K. Kuder, T. Waeber, and P. Ermanni, "Variable stiffness characteristics of embeddable multi-stable composites," *Composites Science and Technology,* vol. 97, pp. 12-18, 2014.

[119] C. Sousa, P. Camanho, and A. Suleman, "Analysis of multistable variable stiffness composite plates," *Composite Structures,* vol. 98, pp. 34-46, 2013.

[120] S. A. Emam and D. J. Inman, "A review on bistable composite laminates for morphing and energy harvesting," *Applied Mechanics Reviews,* vol. 67, p. 060803, 2015.

[121] S. Barbarino, O. Bilgen, R. M. Ajaj, M. I. Friswell, and D. J. Inman, "A review of morphing aircraft," *Journal of intelligent material systems and structures,* vol. 22, pp. 823-877, 2011.

[122] A. Sofla, S. Meguid, K. Tan, and W. Yeo, "Shape morphing of aircraft wing: status and challenges," *Materials & Design,* vol. 31, pp. 1284-1292, 2010.

[123] J. C. Gomez and E. Garcia, "Morphing unmanned aerial vehicles," *Smart Materials and Structures,* vol. 20, p. 103001, 2011.

[124] S. Daynes and P. M. Weaver, "Review of shape-morphing automobile structures: concepts and outlook," *Proceedings of the Institution of Mechanical Engineers, Part D: Journal of Automobile Engineering,* vol. 227, pp. 1603-1622, 2013.

[125] I. K. Kuder, A. F. Arrieta, W. E. Raither, and P. Ermanni, "Variable stiffness material and structural concepts for morphing applications," *Progress in Aerospace Sciences,* vol. 63, pp. 33-55, 2013.

[126] S. Daynes and P. M. Weaver, "Stiffness tailoring using prestress in adaptive composite structures," *Composite Structures,* vol. 106, pp. 282-287, 2013.

[127] G. Tibert, "Deployable tensegrity structures for space applications," KTH, 2002.

[128] A. Hanaor, "Some structural-morphological aspects of deployable structures for space enclosures," *An Anthology of Structural Morphology,* p. 83, 2009.

[129] S.-P. Jung, G.-P. Jung, J.-S. Koh, D.-Y. Lee, and K.-J. Cho, "Fabrication of Composite and Sheet Metal Laminated Bistable Jumping Mechanism," *Journal of Mechanisms and Robotics,* vol. 7, p. 021010, 2015.

[130] R. F. Shepherd, F. Ilievski, W. Choi, S. A. Morin, A. A. Stokes, A. D. Mazzeo*, et al.*, "Multigait soft robot," *Proceedings of the National Academy of Sciences,* vol. 108, pp. 20400-20403, 2011.

[131] V. Böhm, I. Zeidis, and K. Zimmermann, "An approach to the dynamics and control of a planar tensegrity structure with application in locomotion systems," *International Journal of Dynamics and Control,* vol. 3, pp. 41-49, 2015.

[132] V. Böhm, T. Kaufhold, I. Zeidis, and K. Zimmermann, "Dynamic analysis of the rolling locomotion of mobile robots based on tensegrity structures with two curved compressed components," in *Proceedings of the 13th conference on dynamical systems-theory and applications, Łódź*, 2015, pp. 105-116.

[133] L.-H. Chen, B. Cera, E. L. Zhu, R. Edmunds, F. Rice, A. Bronars*, et al.*, "Inclined Surface Locomotion Strategies for Spherical Tensegrity Robots," *arXiv preprint arXiv:1708.08150,* 2017.

[134] V. Boehm, A. Jentzsch, T. Kaufhold, F. Schneider, F. Becker, and K. Zimmermann, "An approach to locomotion systems based on 3d tensegrity structures with a minimal number of struts," in *Robotics; Proceedings of ROBOTIK 2012; 7th German Conference on*, 2012, pp. 1-6.

[135] N. De Temmerman, L. A. Mira, A. Vergauwen, H. Hendrickx, and W. De Wilde, "Transformable structures in architectural engineering," *High Performance Structures and Materials VI,* vol. 124, p. 457, 2012.

[136] N. De Temmerman, K. Roovers, L. A. Mira, A. Vergauwen, A. Koumar, S. Brancart*, et al.*, "Lightweight transformable structures: materialising the synergy between architectural and structural engineering," *Mobile and rapidly assembled structures IV,* vol. 136, p. 1, 2014.

[137] R. E. Skelton and M. C. de Oliveira, *Tensegrity systems* vol. 1: Springer, 2009.

[138] K. Seffen, Z. You, and S. Pellegrino, "Folding and deployment of curved tape springs," *International Journal of Mechanical Sciences,* vol. 42, pp. 2055-2073, 2000.

[139] T. W. Murphey and S. Pellegrino, "A novel actuated composite tape-spring for deployable structures," in *Proceedings of the 45th AIAA/ASME/ASCE/AHS/ASC Structures, Structural Dynamics & Materials Conference, Reston, Virigina*, 2004.

[140] J. Costantine, Y. Tawk, C. G. Christodoulou, J. Banik, and S. Lane, "CubeSat deployable antenna using bistable composite tape-springs," *IEEE Antennas and Wireless Propagation Letters,* vol. 11, pp. 285-288, 2012.

[141] J. Hu, D. Pan, and F. Dai, "Microstrip Patch Array Antenna With Reconfigurable Omnidirectional and Directional Patterns Using Bistable Composite Laminates," *IEEE Antennas and Wireless Propagation Letters,* vol. 16, pp. 2485-2488, 2017.

[142] T. Chen, J. Mueller, and K. Shea, "Integrated Design and Simulation of Tunable, Multi-State Structures Fabricated Monolithically with Multi-Material 3D Printing," *Scientific Reports,* vol. 7, 2017.

[143] W. Wang, H. Rodrigue, and S.-H. Ahn, "Deployable soft composite structures," *Scientific reports,* vol. 6, p. 20869, 2016.

[144] H. Furuya, "Concept of deployable tensegrity structures in space application," *International Journal of Space Structures,* vol. 7, pp. 143-151, 1992.

[145] N. Wang, J. P. Butler, and D. E. Ingber, "Mechanotransduction across the cell surface and through the cytoskeleton," *Science,* pp. 1124-1127, 1993.

[146] D. E. Ingber, "Cellular tensegrity: defining new rules of biological design that govern the cytoskeleton," *Journal of cell science,* vol. 104, pp. 613-627, 1993.

[147] D. Stamenović, J. J. Fredberg, N. Wang, J. P. Butler, and D. E. Ingber, "A microstructural approach to cytoskeletal mechanics based on tensegrity," *Journal of Theoretical Biology,* vol. 181, pp. 125-136, 1996.

[148] S. Sumi, V. Böhm, F. Schale, R. Roeder, A. Karguth, and K. Zimmermann, "A Novel Gripper Based on a Compliant Multistable Tensegrity Mechanism," in *Microactuators and Micromechanisms,* ed: Springer, 2017, pp. 115-126.

[149] S. Sumi, V. Böhm, F. Schale, and K. Zimmermann, "Compliant gripper based on a multistable tensegrity structure," in *New Trends in Mechanism and Machine Science,* ed: Springer, 2017, pp. 143-151.

[150] S. Sumi, V. Böhm, and K. Zimmermann, "A multistable tensegrity structure with a gripper application," *Mechanism and Machine Theory,* vol. 114, pp. 204-217, 2017.

[151] C. Jianguo, D. Xiaowei, Z. Ya, F. Jian, and T. Yongming, "Bistable behavior of the cylindrical origami structure with Kresling pattern," *Journal of Mechanical Design,* vol. 137, p. 061406, 2015.

[152] J. Cai, X. Deng, J. Feng, and Y. Zhou, "Geometric design and mechanical behavior of a deployable cylinder with Miura origami," *Smart Materials and Structures,* vol. 24, p. 125031, 2015.

[153] A. Pagano, B. Leung, B. Chien, T. Yan, A. Wissa, and S. Tawfick, "Multi-Stable Origami Structure for Crawling Locomotion," in *ASME 2016 Conference on Smart Materials, Adaptive Structures and Intelligent Systems,* 2016, pp. V002T06A005-V002T06A005.

[154] A. Pagano, T. Yan, B. Chien, A. Wissa, and S. Tawfick, "A crawling robot driven by multi-stable origami," *Smart Material Structures,* vol. 26, 2017.

[155] B. J. Hansen, C. J. Carron, B. Jensen, A. Hawkins, and S. Schultz, "Plastic latching accelerometer based on bistable compliant mechanisms," *Smart Materials and Structures,* vol. 16, p. 1967, 2007.

[156] B. Todd, M. Phillips, S. M. Schultz, A. R. Hawkins, and B. D. Jensen, "Low-cost RFID threshold shock sensors," *IEEE Sensors Journal,* vol. 9, pp. 464-469, 2009.

[157] A. Frangi, B. De Masi, F. Confalonieri, and S. Zerbini, "Threshold Shock Sensor Based on a Bistable Mechanism: Design, Modeling, and Measurements," *Journal of Microelectromechanical Systems,* vol. 24, pp. 2019-2026, 2015.

[158] J. Zhao, Y. Yang, K. Fan, P. Hu, and H. Wang, "A bistable threshold accelerometer with fully compliant clamped-clamped mechanism," *IEEE Sensors Journal,* vol. 10, pp. 1019-1024, 2010.

[159] J. Zhao, Y. Yang, H. Wang, and J. Jia, "A novel magnetic actuated bistable acceleration switch with low contact resistance," *IEEE Sensors Journal,* vol. 10, pp. 869-876, 2010.

[160] J. Zhao, R. Gao, Y. Yang, Y. Huang, and P. Hu, "A bidirectional acceleration switch incorporating magnetic-fields-based tristable mechanism," *IEEE/ASME Transactions on Mechatronics,* vol. 18, pp. 113-120, 2013.

[161] J. Zhao, S. Wang, D. McCoul, Z. Xing, B. Huang, L. Liu, *et al.*, "Bistable dielectric elastomer minimum energy structures," *Smart Mater. Struct,* vol. 25, p. 075016, 2016.

[162] R. Vitushinsky, S. Schmitz, and A. Ludwig, "Bistable thin-film shape memory actuators for applications in tactile displays," *Journal of Microelectromechanical Systems,* vol. 18, pp. 186-194, 2009.

[163] Y. Gerson, S. Krylov, B. Ilic, and D. Schreiber, "Design considerations of a large-displacement multistable micro actuator with serially connected bistable elements," *Finite Elements in Analysis and Design,* vol. 49, pp. 58-69, 2012.

[164] L. Masia, L. Cappello, P. Morasso, X. Lachenal, A. Pirrera, P. Weaver, *et al.*, "A novel composite advanced robotic actuator powering assistive compliant exoskeleton preliminary design," in *Rehabilitation Robotics (ICORR), 2013 IEEE International Conference on*, 2013, pp. 1-8.

[165] R. Mutlu and G. Alıcı, "A multistable linear actuation mechanism based on artificial muscles," *Journal of Mechanical Design*, vol. 132, p. 111001, 2010.

[166] H. Matoba, T. Ishikawa, C.-J. Kim, and R. S. Muller, "A bistable snapping microactuator," in *Micro Electro Mechanical Systems, 1994, MEMS'94, Proceedings, IEEE Workshop on*, 1994, pp. 45-50.

[167] J. Oberhammer, M. Tang, A.-Q. Liu, and G. Stemme, "Mechanically tri-stable, true single-pole-double-throw (SPDT) switches," *Journal of Micromechanics and Microengineering,* vol. 16, p. 2251, 2006.

[168] S. Zaidi, F. Lamarque, C. Prelle, O. Carton, and A. Zeinert, "Contactless and selective energy transfer to a bistable micro-actuator using laser heated shape memory alloy," *Smart Materials and Structures,* vol. 21, p. 115027, 2012.

[169] B. Wagner, H. Quenzer, S. Hoerschelmann, T. Lisec, and M. Juerss, "Bistable microvalve with pneumatically coupled membranes," in *Micro Electro Mechanical Systems, 1996, MEMS'96, Proceedings. An Investigation of Micro Structures, Sensors, Actuators, Machines and Systems. IEEE, The Ninth Annual International Workshop on*, 1996, pp. 384-388.

[170] C. Goll, W. Bacher, B. Büstgens, D. Maas, W. Menz, and W. Schomburg, "Microvalves with bistable buckled polymer diaphragms," *Journal of Micromechanics and Microengineering,* vol. 6, p. 77, 1996.

[171] W. Schomburg and C. Goll, "Design optimization of bistable microdiaphragm valves," *Sensors and Actuators A: Physical,* vol. 64, pp. 259-264, 1998.

[172] V. Intaraprasonk and S. Fan, "Nonvolatile bistable all-optical switch from mechanical buckling," *Applied Physics Letters,* vol. 98, p. 241104, 2011.

[173] D. N. Guerra, M. Imboden, and P. Mohanty, "Electrostatically actuated silicon-based nanomechanical switch at room temperature," *Applied Physics Letters,* vol. 93, p. 033515, 2008.

[174] I.-H. Hwang, Y.-S. Shim, and J.-H. Lee, "Modeling and experimental characterization of the chevron-type bi-stable microactuator," *Journal of Micromechanics and Microengineering,* vol. 13, p. 948, 2003.

[175] R. A. Receveur, C. R. Marxer, R. Woering, V. C. Larik, and N.-F. de Rooij, "Laterally moving bistable MEMS DC switch for biomedical applications," *Journal of microelectromechanical systems,* vol. 14, pp. 1089-1098, 2005.

[176] K. Peterson, "Bistable micromechanical storage element in silicon," *IBM Technical Disclosure Bulletin,* vol. 20, 1978.

[177] B. Halg, "On a micro-electro-mechanical nonvolatile memory cell," *IEEE Transactions on Electron Devices,* vol. 37, pp. 2230-2236, 1990.

[178] B. Halg, "On a nonvolatile memory cell based on micro-electro-mechanics," in *Micro electro mechanical systems, 1990. proceedings, an investigation of micro structures, sensors, actuators, machines and robots. IEEE,* 1990, pp. 172-176.

[179] Y. Tsuchiya, K. Takai, N. Momo, T. Nagami, H. Mizuta, S. Oda, *et al.*, "Nanoelectromechanical nonvolatile memory device incorporating nanocrystalline Si dots," *Journal of applied physics,* vol. 100, p. 094306, 2006.

[180] R. L. Badzey and P. Mohanty, "Coherent signal amplification in bistable nanomechanical oscillators by stochastic resonance," *arXiv preprint cond-mat/0603108,* 2006.

[181] B. Charlot, W. Sun, K. Yamashita, H. Fujita, and H. Toshiyoshi, "Bistable nanowire for micromechanical memory," *Journal of Micromechanics and Microengineering,* vol. 18, p. 045005, 2008.

[182] B. Charlot, W. Sun, K. Yamashita, H. Fujita, and H. Toshiyoshi, "In-plane bistable nanowire for memory devices," in *Design, Test, Integration and Packaging of MEMS/MOEMS, 2008. MEMS/MOEMS 2008. Symposium on*, 2008, pp. 254-258.

[183] D. Roodenburg, J. Spronck, H. Van der Zant, and W. Venstra, "Buckling beam micromechanical memory with on-chip readout," *Applied Physics Letters,* vol. 94, p. 183501, 2009.

[184] S.-M. Jung and K.-S. Yun, "Energy-harvesting device with mechanical frequency-up conversion mechanism for increased power efficiency and wideband operation," *Applied Physics Letters,* vol. 96, p. 111906, 2010.

[185] A. Sneller, P. Cette, and B. Mann, "Experimental investigation of a post-buckled piezoelectric beam with an attached central mass used to harvest energy," *Proceedings of the Institution of Mechanical Engineers, Part I: Journal of Systems and Control Engineering,* vol. 225, pp. 497-509, 2011.

[186] F. Cottone, L. Gammaitoni, H. Vocca, M. Ferrari, and V. Ferrari, "Piezoelectric buckled beams for random vibration energy harvesting," *Smart materials and structures,* vol. 21, p. 035021, 2012.

[187] L. Van Blarigan, P. Danzl, and J. Moehlis, "A broadband vibrational energy harvester," *Applied Physics Letters,* vol. 100, p. 253904, 2012.

[188] L. Tang, Y. Yang, and C. K. Soh, "Toward broadband vibration-based energy harvesting," *Journal of Intelligent Material Systems and Structures,* vol. 21, pp. 1867-1897, 2010.

[189] D. Zhu, M. J. Tudor, and S. P. Beeby, "Strategies for increasing the operating frequency range of vibration energy harvesters: a review," *Meas. Sci. Technol,* vol. 21, p. 022001, 2010.

[190] A. Wickenheiser and E. Garcia, "Broadband vibration-based energy harvesting improvement through frequency up-conversion by magnetic excitation," *Smart materials and Structures,* vol. 19, p. 065020, 2010.

[191] S. Liu and R. Burgueño, "Controlled elastic postbuckling of bilaterally constrained non-prismatic columns: application to enhanced quasi-static energy harvesters," *Smart Materials and Structures*, vol. 25, p. 125010, 2016.

[192] N. Lajnef, R. Burgueño, W. Borchani, and Y. Sun, "A concept for energy harvesting from quasi-static structural deformations through axially loaded bilaterally constrained columns with multiple bifurcation points," *Smart Materials and Structures,* vol. 23, p. 055005, 2014.

[193] R. Burgueno and N. Lajnef, "Energy harvesting devices for low frequency applications," USA Patent 9438139, 2016/09/06, 2016.

[194] R. Harne and K. Wang, "A review of the recent research on vibration energy harvesting via bistable systems," *Smart materials and structures*, vol. 22, p. 023001, 2013.

[195] R. L. Harne and K.-W. Wang, *Harnessing Bistable Structural Dynamics: For Vibration Control, Energy Harvesting and Sensing*: John Wiley & Sons, 2017.

[196] R. S. Lakes, T. Lee, A. Bersie, and Y. Wang, "Extreme damping in composite materials with negative-stiffness inclusions," *Nature,* vol. 410, p. 565, 2001.

[197] R. Lakes, "Extreme damping in composite materials with a negative stiffness phase," *Physical review letters*, vol. 86, p. 2897, 2001.

[198] D. M. Kochmann, "Stable extreme damping in viscoelastic two-phase composites with non-positive-definite phases close to the loss of stability," *Mechanics Research Communications,* vol. 58, pp. 36-45, 2014.

[199] N. Kidambi, R. Harne, and K. Wang, "Adaptation of energy dissipation in a mechanical metastable module excited near resonance," *Journal of Vibration and Acoustics*, vol. 138, p. 011001, 2016.

[200] N. Kidambi, R. Harne, and K. Wang, "Strain Energy Trapping due to Energetic Asymmetry in Modular Structures Inspired by Muscle Cross-Bridges," in *ASME 2016 International Design Engineering Technical Conferences and Computers and Information in Engineering Conference*, 2016, pp. V008T10A052-V008T10A052.

[201] N. Kidambi, R. L. Harne, and K. Wang, "Energy capture and storage in asymmetrically multistable modular structures inspired by skeletal muscle," *Smart Materials and Structures,* vol. 26, 2017.

[202] N. Kidambi, R. L. Harne, and K.-W. Wang, "Corrigendum: Energy capture and storage in asymmetrically multistable modular structures inspired by skeletal muscle (2017 Smart Mater. Struct. 26 085011)," *Smart Materials and Structures*, 2017.

[203] L. Wu, X. Xi, B. Li, and J. Zhou, "Multi - Stable Mechanical Structural Materials," *Advanced Engineering Materials,* 2017.

[204] E. B. Duoss, T. H. Weisgraber, K. Hearon, C. Zhu, W. Small IV, T. R. Metz, *et al.*, "Three‐dimensional printing of elastomeric, cellular architectures with negative stiffness," *Advanced Functional Materials,* vol. 24, pp. 4905-4913, 2014.

[205] D. Restrepo, N. D. Mankame, and P. D. Zavattieri, "Phase transforming cellular materials," *Extreme Mechanics Letters,* vol. 4, pp. 52-60, 2015.

[206] T. Frenzel, C. Findeisen, M. Kadic, P. Gumbsch, and M. Wegener, "Tailored Buckling Microlattices as Reusable Light‐Weight Shock Absorbers," *Advanced Materials,* vol. 28, pp. 5865-5870, 2016.

[207] C. Findeisen, J. Hohe, M. Kadic, and P. Gumbsch, "Characteristics of mechanical metamaterials based on buckling elements," *Journal of the Mechanics and Physics of Solids,* vol. 102, pp. 151-164, 2017.

[208] D. M. Correa, T. Klatt, S. Cortes, M. Haberman, D. Kovar, and C. Seepersad, "Negative stiffness honeycombs for recoverable shock isolation," *Rapid Prototyping Journal,* vol. 21, pp. 193-200, 2015.

[209] D. M. Correa, C. C. Seepersad, and M. R. Haberman, "Mechanical design of negative stiffness honeycomb materials," *Integrating Materials and Manufacturing Innovation,* vol. 4, pp. 1-11, 2015.

[210] K. Che, C. Yuan, J. Wu, H. J. Qi, and J. Meaud, "Three-Dimensional-Printed Multistable Mechanical Metamaterials With a Deterministic Deformation Sequence," *Journal of Applied Mechanics,* vol. 84, p. 011004, 2017.

[211] B. Haghpanah, L. Salari‐Sharif, P. Pourrajab, J. Hopkins, and L. Valdevit, "Multistable Shape‐Reconfigurable Architected Materials," *Advanced Materials,* vol. 28, pp. 7915-7920, 2016.

[212] A. Rafsanjani, A. Akbarzadeh, and D. Pasini, "Snapping mechanical metamaterials under tension," *Advanced Materials,* vol. 27, pp. 5931-5935, 2015.

[213] V. R. Tuz and S. L. Prosvimin, "Multistable response of trapping light nonlinear structures," in *Laser and Fiber-Optical Networks Modeling (LFNM), 2011 11th International Conference on,* 2011, pp. 1-3.

[214] R. L. Harne, Y. Song, and Q. Dai, "Trapping and attenuating broadband vibroacoustic energy with hyperdamping metamaterials," *Extreme Mechanics Letters,* vol. 12, pp. 41-47, 2017.

[215] C. S. Ha, R. S. Lakes, and M. E. Plesha, "Design, Fabrication, and Analysis of Lattice Exhibiting Energy Absorption via Snap-through Behavior," *Materials & Design,* 2018.

[216] H. A. Sodano, D. J. Inman, and G. Park, "A review of power harvesting from vibration using piezoelectric materials," *Shock and Vibration Digest*, vol. 36, pp. 197-206, 2004.

[217] S. P. Beeby, M. J. Tudor, and N. White, "Energy harvesting vibration sources for microsystems applications," *Measurement science and technology*, vol. 17, p. R175, 2006.

[218] P. L. Green, E. Papatheou, and N. D. Sims, "Energy harvesting from human motion and bridge vibrations: An evaluation of current nonlinear energy harvesting solutions," *Journal of Intelligent Material Systems and Structures*, vol. 24, pp. 1494-1505, 2013.

[219] S. Roundy, E. S. Leland, J. Baker, E. Carleton, E. Reilly, E. Lai, *et al.*, "Improving power output for vibration-based energy scavengers," *IEEE Pervasive computing*, vol. 4, pp. 28-36, 2005.

[220] K. Najafi, T. Galchev, E. Aktakka, R. Peterson, and J. McCullagh, "Microsystems for energy harvesting," in *2011 16th International Solid-State Sensors, Actuators and Microsystems Conference*, 2011, pp. 1845-1850.

[221] T. L. Bergman, F. P. Incropera, D. P. DeWitt, and A. S. Lavine, *Fundamentals of heat and mass transfer*: John Wiley & Sons, 2011.

[222] S. Liu, A. I. Azad, and R. Burgueño, "Energy harvesting from quasi-static deformations via bilaterally constrained strips," *Journal of Intelligent Material Systems and Structures*, vol. 29, pp. 3572-3581, 2018.

[223] S. Liu and R. Burgueño, "Elastic Postbuckling Response of Bilaterally Constrained Non-Prismatic Columns," in *The Sixth International Conference on Structural Engineering, Mechanics and Computation*, Cape Town, South Africa, 2016.

[224] S. Liu, N. Hu, and R. Burgueño, "Postbuckling Behavior of Axially-Compressed Strips With Discrete Rigid Constraints: A Numerical Study," in *ASME 2015 Conference on Smart Materials, Adaptive Structures and Intelligent Systems*, 2015, pp. V001T03A024-V001T03A024.

[225] S. Liu, A. I. Azad, and R. Burgueño, "Architected materials for tailorable shear behavior with energy dissipation," *Extreme Mechanics Letters*, 2019.

[226] J. Sohn, S. B. Choi, and D. Lee, "An investigation on piezoelectric energy harvesting for MEMS power sources," *Proceedings of the Institution of Mechanical Engineers, Part C: Journal of Mechanical Engineering Science*, vol. 219, pp. 429-436, 2005.

[227] J. Cain, W. Clark, L. Schaefer, D. Ulinski, M. Mickle, and W. Mandecki, "Energy harvesting for DNA gene sifting and sorting," *International Journal of Parallel and Distributed Systems and Networks*, vol. 4, pp. 140-149, 2001.

[228] A. Nanda and M. A. Karami, "Energy harvesting from arterial blood pressure for powering embedded micro sensors in human brain," *Journal of Applied Physics*, vol. 121, p. 124506, 2017.

[229] S. Roundy, P. K. Wright, and J. M. Rabaey, *Energy scavenging for wireless sensor networks*: Springer, 2003.

[230] B. A. Warneke and K. S. Pister, "Exploring the limits of system integration with smart dust," in *ASME 2002 International Mechanical Engineering Congress and Exposition*, 2002, pp. 621-625.

[231] S. Chakrabartty, N. Lajnef, N. G. Elvin, and A. S. Gore, "Self-powered sensor," ed: Google Patents, 2011.

[232] D. McCreery, A. Lossinsky, V. Pikov, and X. Liu, "Microelectrode array for chronic deep-brain microstimulation and recording," *IEEE transactions on biomedical engineering,* vol. 53, pp. 726-737, 2006.

[233] Y. Qi, J. Kim, T. D. Nguyen, B. Lisko, P. K. Purohit, and M. C. McAlpine, "Enhanced piezoelectricity and stretchability in energy harvesting devices fabricated from buckled PZT ribbons," *Nano letters,* vol. 11, pp. 1331-1336, 2011.

[234] Y. Wang, T. Ma, H. Yu, and H. Jiang, "Random analysis on controlled buckling structure for energy harvesting," *Applied Physics Letters,* vol. 102, p. 041915, 2013.

[235] M. Ansari and M. A. Karami, "Energy harvesting from controlled buckling of piezoelectric beams," *Smart Materials and Structures,* vol. 24, p. 115005, 2015.

[236] L. Xiong, L. Tang, and B. R. Mace, "Internal resonance with commensurability induced by an auxiliary oscillator for broadband energy harvesting," *Applied Physics Letters,* vol. 108, p. 203901, 2016.

[237] A. Erturk and D. Inman, "Broadband piezoelectric power generation on high-energy orbits of the bistable Duffing oscillator with electromechanical coupling," *Journal of Sound and Vibration,* vol. 330, pp. 2339-2353, 2011.

[238] C. Peters, D. Maurath, W. Schock, and Y. Manoli, "Novel electrically tunable mechanical resonator for energy harvesting," *Proceedings PowerMEMS 2008,* pp. 253-256, 2008.

[239] M. Soliman, E. Abdel-Rahman, E. El-Saadany, and R. Mansour, "A wideband vibration-based energy harvester," *journal of micromechanics and microengineering,* vol. 18, p. 115021, 2008.

[240] H. S. Kim, J.-H. Kim, and J. Kim, "A review of piezoelectric energy harvesting based on vibration," *International Journal of precision engineering and manufacturing,* vol. 12, pp. 1129-1141, 2011.

[241] R. Burgueno and N. Lajnef, "Energy harvesting devices for low frequency applications," ed: Google Patents, 2016.

[242] W. Borchani, N. Lajnef, and R. Burgueño, "Energy method solution for the postbuckling response of an axially loaded bilaterally constrained beam," *Mechanics Research Communications,* vol. 70, pp. 114-119, 2015.

[243] H. Chai, "The post-buckling response of a bi-laterally constrained column," *Journal of the Mechanics and Physics of Solids,* vol. 46, pp. 1155-1181, 1998.

[244] E. Stein, W. Wagner, and P. Wriggers, "Nonlinear stability-analysis of shell and contact-problems including branch-switching," *Computational Mechanics,* vol. 5, pp. 428-446, 1990.

[245] S. P. Timoshenko and J. M. Gere, *Theory of elastic stability*: Courier Corporation, 2009.

[246] R. H. Plaut and Y.-W. Yang, "Behavior of three-span braced columns with equal or unequal spans," *Journal of Structural Engineering,* vol. 121, pp. 986-994, 1995.

[247] R. Javaheri and M. Eslami, "Buckling of Functionally Graded Plates under In‐plane Compressive Loading," *ZAMM‐Journal of Applied Mathematics and Mechanics/Zeitschrift für Angewandte Mathematik und Mechanik,* vol. 82, pp. 277-283, 2002.

[248] A. Dinnik, "Design of columns of varying cross section," *Trans ASME,* vol. 51, pp. 105-14, 1929.

[249] S. Timoshenko, "Buckling of bars of variable cross section," *Bulletin of the Polytechnic Institute, Kiev, USSR,* 1908.

[250] I. Elishakoff, "Both static deflection and vibration mode of uniform beam can serve as a buckling mode of a non-uniform column," *Journal of Sound and Vibration,* vol. 232, pp. 477-489, 4/27/ 2000.

[251] I. Elishakoff, *Eigenvalues of inhomogeneous structures: unusual closed-form solutions*: CRC Press, 2004.

[252] F. Arbabi and F. Li, "Buckling of variable cross-section columns: integral-equation approach," *Journal of Structural Engineering,* vol. 117, pp. 2426-2441, 1991.

[253] C. Wang and C. Y. Wang, *Exact solutions for buckling of structural members* vol. 6: CRC press, 2004.

[254] D. Pasini, "Shape transformers for material and shape selection of lightweight beams," *Materials & Design,* vol. 28, pp. 2071-2079, 2007.

[255] D. Pasini, "Shape and material selection for optimizing flexural vibrations in multilayered resonators," *Microelectromechanical Systems, Journal of,* vol. 15, pp. 1745-1758, 2006.

[256] P. Jiao, W. Borchani, H. Hasni, A. H. Alavi, and N. Lajnef, "An energy harvesting solution based on the post-buckling response of non-prismatic slender beams," in *Smart Materials and Nondestructive Evaluation for Energy Systems 2017*, 2017, p. 101710A.

[257] P. Jiao, W. Borchani, H. Hasni, and N. Lajnef, "Enhancement of quasi-static strain energy harvesters using non-uniform cross-section post-buckled beams," *Smart Materials and Structures*, vol. 26, p. 085045, 2017.

[258] N. Hu and R. Burgueño, "Tailoring the elastic postbuckling response of cylindrical shells: A route for exploiting instabilities in materials and mechanical systems," *Extreme Mechanics Letters*, vol. 4, pp. 103-110, 2015.

[259] J. Guo, S. Liu, and R. Burgueño, "Tailoring the Elastic Postbuckling Response of Thin-Walled Cylindrical Shells for Applications in Mechanical Devices and Adaptive Structures," p. V002T03A037, 2017.

[260] B. F. Feeny and A. R. Diaz, "Twinkling phenomena in snap-through oscillators," *Journal of Vibration and Acoustics*, vol. 132, p. 061013, 2010.

[261] J. Prasad and A. Diaz, "Synthesis of bistable periodic structures using topology optimization and a genetic algorithm," *Journal of mechanical design*, vol. 128, pp. 1298-1306, 2006.

[262] N. Nadkarni, C. Daraio, and D. M. Kochmann, "Dynamics of periodic mechanical structures containing bistable elastic elements: From elastic to solitary wave propagation," *Physical Review E*, vol. 90, p. 023204, 2014.

[263] Y. Cui and M. Santer, "Adaptive multistable flexible composite surfaces," in *Spacecraft Structures Conference*, 2014, p. 0671.

[264] J. G. A. Croll and A. C. Walker, *Elements of structural stability*: John Wiley & Sons, 1972.

[265] V. Slesarenko and S. Rudykh, "Towards mechanical characterization of soft digital materials for multimaterial 3D-printing," *International Journal of Engineering Science,* vol. 123, pp. 62-72, 2018.

[266] N. G. Elvin and A. A. Elvin, "A general equivalent circuit model for piezoelectric generators," *Journal of Intelligent Material Systems and Structures*, vol. 20, pp. 3-9, 2009.

[267] I. Müller and P. Villaggio, "A model for an elastic-plastic body," *Archive for Rational Mechanics and Analysis*, vol. 65, pp. 25-46, 1977.

[268] G. Puglisi and L. Truskinovsky, "Mechanics of a discrete chain with bi-stable elements," *Journal of the Mechanics and Physics of Solids*, vol. 48, pp. 1-27, 2000.